Modifying the Hohlraum Environment For Improved Drive in Inertial Confinement Fusion

Joseph Michael Owen

Doctor of Philosophy

University of York

Physics

September 2021

Acknowledgements

Firstly, I would like to extend my deepest thanks to my supervisors Chris Ridgers and John Pasley, who have both been an invaluable source of expertise and encouragement during my PhD.

I would also like to thank everyone at the York Plasma Institute for creating a welcoming and supportive environment that I am proud to have been a part of.

In addition, I would like to thank Raoul Trines and Robbie Scott and the Rutherford Appleton Laboratory for providing access to and maintaining the computing systems on which HYADES and h2d was used.

Finally, I thank my family and friends for their the patience and support, without which none of this would be possible.

This work was funded by the Engineering and Physical Sciences Research Council [EP/L01663X/1].

This work was funded by the UK Atomic Weapons Establishment (AWE).

Abstract

This thesis contains simulation work carried out in order to understand the effect of modifying the hohlraum environment and the consequences of these modifications on the performance of an inertial confinement fusion capsule.

Simulations were carried out using the radiation hydrodynamic codes HYADES and h2d. In addition, a view-factor code was developed in order to calculate the radiation symmetry for different hohlraum designs.

Firstly, h2d was used to study the effect of lining the inside of a hohlraum with a mid-Z element, in this case copper, on the X-ray drive produced. A reduction in the hard X-ray component of the drive was found and attributed to the inclusion of the liner. The mechanism by which this reduction occurs was investigated and is outlined within this work. Secondly, the consequences of including a mid-Z liner were investigated by using HYADES to perform 1D implosions of capsules. A hohlraum with a reduced high energy X-ray content will be able to drive a capsule that contains lower levels of dopant. Implosions of capsules containing several different dopant concentrations were compared with regards to the ignition threshold energy in order to assess the benefit of using a lined hohlraum. Finally, a method for tailoring the X-ray drive symmetry in hohlraums via albedo-profiling of the hohlraum wall was investigated using a view-factor method. Symmetry control in geometries relevant to laser-driven and z-pinch driven hohlraums was obtained by using this method with the extent presented in the final results section of this thesis.

Contents

List of Figures

Declaration

This thesis has not previously been accepted in substance for any degree and is not being concurrently submitted in candidature for any degree other than Doctor of Philosophy of the University of York. This thesis is the result of my own investigations, except where otherwise stated. Other sources are acknowledged by explicit references. Work contained within Chapter 4 has been published in the following article

- J. Owen, J. Pasley, C. P. Ridgers, ”Investigation of the performance of mid-Z Hohlraum wall liners for producing x-ray drive”, Physics of Plasmas 28, 012703 (2021)

Data is available upon reasonable request from the authors. The simulation codes HYADES and h2d are commercial products of Cascade Applied Sciences. This work has been supervised by Dr John Pasley and Dr Christopher Ridgers.

My personal invovlement in this work included the design and running of the radiation hydrodynamic simulations, analysis and interpretation of the results of those simulations, and the determination of the research direction. In addition, I was soley responsible for the creation of the view-factor code, its running, and analysis and interpretation of the results. Dr John Pasley initially brought to the fore the work by Olson *et al* on mid-Z lined hohlraums on which forms the base of the initial results chapter of this work.

I hereby give consent for my thesis, if accepted, to be made available for photocopying and for inter-library loan, and for the title and summary to be made available to outside organisations.

Chapter 1

Introduction

The need for a sustainable source of safe, clean, reliable energy is greater now than it has ever been [1]. Human impact on the climate due to the burning of fossil fuels and the release of green-house gases could mean mass extinctions of plant and animal species [2]. In addition, rising sea levels and changing weather could mean disaster for coastal inhabitants [3].

A worldwide response to the dangers of climate change is needed and sustainable solutions for the energy sector are required if we are to continue to enjoy the benefits that technology and electricity bring. The decarbonisation of some of the worlds biggest polluters is not without challenge, as countries with the largest reserves of fossil fuels are seeing a higher increase in demand for fossil fuels than for other renewable energy sources [4]. In fact, in order to keep carbon levels on target to help reduce climate change it is estimated that of the known reserves, 80% of the coal, 50% of the gas and 30% of the oil need to be left untouched [5]. This presents a major hurdle for countries whose economies and the daily lives of their citizens are dependent on the burning of fossil fuels.

Mass decarbonisation of our industries is required in order to meet global emission targets [6] necessitating the development of alternative forms of energy production such as wind and solar. These renewable energy sources rely on using wind to turn turbines to generate electrical energy and the conversion of sunlight into electricity inside of photovoltaic cells respectively. Both are subject to the availability of these natural phenomena, hence why a lot of wind turbines are located offshore and solar panels are located in regions with reliable levels of sunlight and adequate space. However, seasonal and daily variations in the electrical power generated by these renewables necessitates the use of batteries for storing energy for use when the power production dips [7]. Though work is ongoing into designing optimal configurations of wind turbines, solar arrays and batteries [8, 9] the need for a constant baseline source of electrical power still exists. High electrical energy losses are incurred from the cables used to transport the electricity long distances as is required to counter the variability in power generation between locations [10]. This coupled with the issue of creating stable and efficient battery storage means that a grid such as this which supports large amounts of renewable energy sources presents a complex problem.

Having renewables work alongside a constant power generator such as biofuel [11], nuclear fission, or the subject of this thesis - nuclear fusion, would allow a responsive electricity supply of clean energy that could meet the demand of the grid.

In fusion reactors the radioactive waste, assuming a fuel is used for which neutrons are a primary product of the fusion reactions, would be generated predominantly in the surrounding structural materials of the reactor. Neutrons from the fusion reactions are high energy and therefore very penetrating and will activate materials that are in the vicinity of the burning plasma. Work is ongoing to develop materials such as steels [12] which can withstand the neutron bombardment and also retain low levels of activation. The absence of great quantities of long-lived radioactive isotopes in fusion reactor designs means that they provide an attractive alternative to traditional fission reactors. Nuclear fission, which produces harmful long-lived radioactive waste, requires complex and expensive storage solutions which need to be maintained for potentially hundreds to thousands of years into the future [13]. In addition, the possible impacts of environmental releases of reactor material from fusion facilities is much lower than those presented by fission [14, 15].

Harnessing nuclear fusion could provide the world with an alternative means of generating great amounts of electrical power from fuel that is in abundance here on earth, seawater. Take the nuclear fusion reaction between isotopes of hydrogen, deuterium $\mathrm{D}(^2\mathrm{H})$ and tritium $\mathrm{T}(^3\mathrm{H})$, for an example

$$\mathrm{D} + \mathrm{T} \;\rightarrow\; \alpha \;(3.5\mathrm{MeV}) + \mathrm{n} \;(14.1\mathrm{MeV}) \tag{1.1}$$

The products of equation 1.1 are an alpha particle (^{4}He nucleus) and a neutron. The neutron carries away most of the energy of the reaction and stopping of these neutrons and conversion of their energy into electricity is required to operate a fusion reactor based on this reaction. The alpha particles, though being of lower energy, still play an important role in the fusion power generation process through re-depositing their energy into the fuel which heats it and sustains the nuclear reactions. The deuterium that exisits on earth was created in the big band and is found in seawater on Earth with a relative abundance by number of 0.016% [16]. While the short-lived (12 years) isotope tritium, has a relative abundance by number of only 0.00005% [16] with its presence being due to human activity such as nuclear reactors and nuclear bombs. Tritium therefore needs to be obtained from other sources such as tritium breeding blankets integrated within fusion reactors [17], creating a self-sustaining system, or from fission reactors such as CANDU-type reactors [18].

1.1 The Physics of Nuclear Fusion

In addition to equation (1.1) there are several reactions between light nuclei to consider, for example

$$\begin{aligned} \mathrm{D} + \mathrm{D} &\rightarrow {}^{3}\mathrm{He} + \mathrm{n} && (1.2) \\ &\rightarrow {}^{3}\mathrm{H} + {}^{1}\mathrm{H} && (1.3) \\ \mathrm{D} + {}^{3}\mathrm{He} &\rightarrow {}^{4}\mathrm{He} + {}^{1}\mathrm{H} && (1.4) \\ \mathrm{p} + {}^{11}\mathrm{B} &\rightarrow 3({}^{4}\mathrm{He}) && (1.5) \end{aligned}$$

Nuclear fusion between deuterium and tritium is the main reaction pathway being considered due to the high average reaction cross-section at relatively low temperatures [19], see figure (1.1). The reaction cross-section is a measure of the likelihood of a reaction taking place and is a function of the center-of-mass energy of the collision or, for thermonuclear fusion, the plasma temperature. It can be used to define the reaction rate of a plasma and therefore the total fusion power output from a volume of plasma.

Consider a high energy beam of deuterium ions fired into a solid tritium target. The nuclear reaction rate per unit volume between the beam with density n_D and a solid slab of tritium atoms of density n_T can be expressed simply as

$$\mathrm{R}_{\mathrm{DT}} = n_D n_T \sigma_{\mathrm{DT}} v \tag{1.6}$$

where σ_{DT} is the cross-section for the deuterium-tritium reaction and v is the relative velocity between the beam and the target. In this situation the fact that the cross section

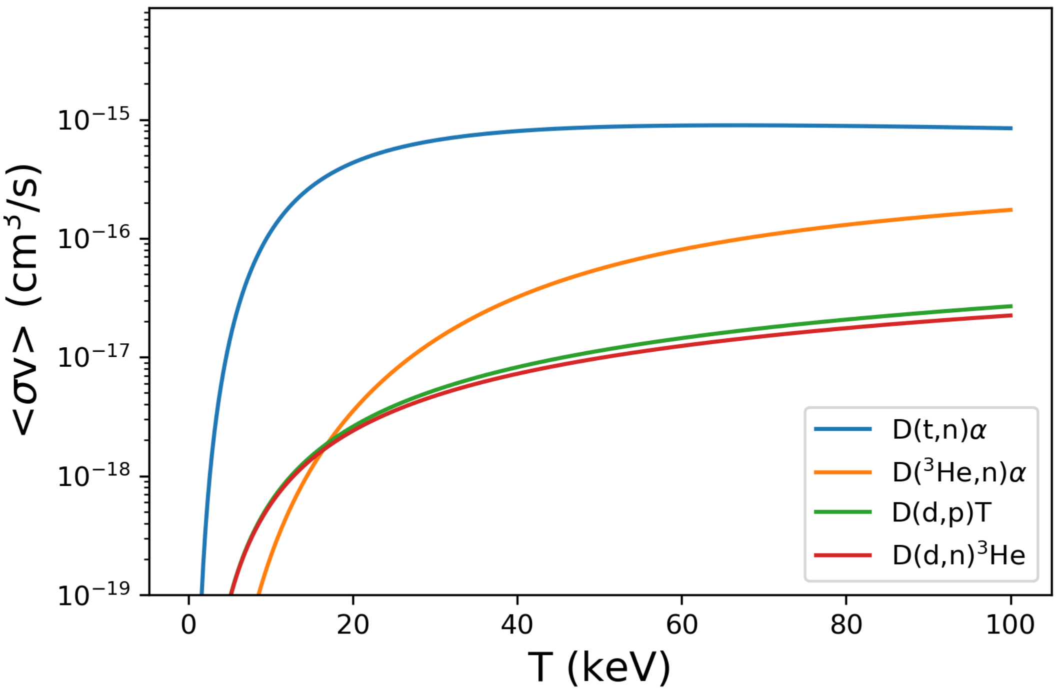

Figure 1.1: Reactivity plotted against temperature for four common light-element nuclear fusion reactions. Reactions are given in the legend where for example the reaction D(d, p)T denotes the reaction of deuterium with deuterium producing a proton and a tritium atom.)

for nuclear reactions is much lower than the sum of the cross sections for other processes such as scattering [20] ([21] p176) means that the particles in the beam are far more likely to lose energy due to scattering rather than undergo nuclear reactions. Ions in the beam will undergoe collisions with the electrons in the target resulting in the ions losing energy based on the ratio of ion to electron mass. The large difference between ion and electron masses means that the electron-ion collisions will dominate as the primary source of energy loss for the ions in the beam. In this situation the potential yield due to these reactions, even supposing a beam of high density and kinetic energy, is very low and the process is highly inefficient as most of the energy goes into heating the target just for the particles in the beam to leave the target where they are no longer able to undergo fusion reactions. Thus the potential for obtaining net energy gain in a single-pass beam-target setup is low.

The beam target approach is the simplest but for this reason of energy efficiency it is not pursued seriously in the context of an industrial scale reactor design. Rather, a thermonuclear approach is considered whereby a high temperature (several keV) plasma is created and confined for a sufficient amount of time in order to obtain energy from the fusion reactions occurring within the volume. Within this thermonuclear plasma most of the interactions will again be scattering events which relax the particle distribution function $f(v)$ to an equilibrium distribution with temperature T. However, for a given equilibrium distribution there will be particles that occupy the high energy tail of the distribution and have velocity high enough for fusion reactions to occur. This overcomes the problem of the higher scattering cross-section dominating the reactions found in a beam-target fusion setup as there will be multiple opportunities for particles to fuse within a thermonuclear plasma.

Though DT is the fuel of choice, owing to its high fusion cross-section, other potential reactions could be utilized in the future. Of particular interest is the aneutronic proton-boron reaction shown in equation (1.5). Though requiring a higher temperature to obtain a similar cross section to DT it removes the issue of neutron bombardment of the surrounding reactor materials which can cause transmutation, displace atoms in the material lattice and alter material properties such as brittleness [22]. It still remains that a high flux of high energy neutrons will be present when utilizing many of the most easily achievable light nuclei fusion reactions, such as DT. Therefore, materials are being developed that can handle these high neutron loads while retaining the mechanical properties needed for the safe and stable operation of a fusion reactor [23, 24].

1.1.1 Plasma Description

Due to the high energies required for fusion to occur the matter involved will be in the plasma state, an ionized gas that exhibits long range electro-magnetic interactions. A plasma in its simplest form is a collection of positive ions and negative electrons (and negative ions in some applications) that forms via ionization mechanisms such as electron-ion collisions or by photo-ionization. Plasmas are the most common state of matter in the universe and understanding them not only improves our ability to harness fusion energy but also our understanding of astrophysical objects [25, 26]. However, it is not sufficient just to have a gas that contains ions and free electrons in order to classify something as a plasma. In fact due to the presence of a high energy tail in the equilibrium distribution function there may well be a small number of free electrons in even a gas at room-temperature that have sufficient energy to ionize atoms.

For an ionized gas to be called a plasma it's dynamics should be dominated by the electromagnetic interactions between it's charged particle constituents rather than the collisions between the neutral particles. The presence of long-range electro-magnetic interactions between the constituent particles of a plasma mean that many different types of wave behaviour are supported. In addition, the dynamics of the plasma can be complicated through the introduction of external electric and magnetic fields. The motion of charged particles in a plasma is governed by their interaction with internally generated fields which arise due to the motion and separation of charges within the plasma and with externally imposed fields. This interaction is governed by the Lorentz force equation

$$\mathbf{F} = q\left(\mathbf{E} + \mathbf{v} \times \mathbf{B}\right) \tag{1.7}$$

where q is the charge of the particle, v is the velocity of the charged particle, E and B are the total electric field and magnetic field respectively due to both other charged particles in the plasma and any externally imposed fields.

Of the phenomena supported by a plasma one of the most important is that of quasi-neutrality. The condition of quasi-neutrality allows a sphere of a certain radius around an ion to be considered as having no net charge due to shielding from surrounding electrons. This removes much of the consideration of long-range interactions between the shielded ion and other charged particles within the plasma. Quasi-neutrality occurs in plasmas due to the local attraction of the negatively charged electrons to the positively charged ions. This movement of electrons takes place over the characteristic timescale for electron plasma waves defined as one over the plasma frequency ($\tau_p = 1/\omega_p$) where the plasma frequency, ω_p, is defined as

$$\omega_p = \sqrt{\frac{ne^2}{\epsilon_0 m_e}} \tag{1.8}$$

where n is the plasma density, e is the electron charge and m_e is the electron mass. Due to the much lower mass of the electron relative to the ions ($m_i/m_e \approx 4600$ for a DT plasma) the electrons can be considered as the only particles that will partake in the Debye shielding process due to their higher relative mobility.

This concentration of negative charge around the ions screens the charge over a characteristic distance known as the Debye length, given by

$$\lambda_D = \sqrt{\frac{\epsilon_0 k_B T_e}{n_e e^2}} \tag{1.9}$$

Equation (1.9) gives the Debye length in a plasma with static ions where T_e is the electron temperature and n_e the electron density. This length is important when it comes to a variety of models used to simulate plasmas such as the fluid theory, allowing individual fluid volumes within the fluid to be considered as having no net charge.

In general, for quasi-neutrality to hold in a plasma both the timescale, τ, and length scale, L, being considered should adhere to the following conditions.

$$\tau >> 1/\omega_p \tag{1.10}$$

$$L >> L_D \tag{1.11}$$

The methods used within this work rely on the assumption that both of the above conditions remain true for the processes being investigated, particularly that the Debye length is smaller than the size of the cells used to discretize the simulation space and also smaller than the scale lengths of gradients within the plasma.

1.1.2 Fusion Power from a Plasma

Now that what is meant by a plasma is more clearly defined it is important to determine the rate of fusion power production from a given plasma. The fusion reaction rate, as in equation (1.6), for a thermonuclear plasma of deuterium and tritium can be expressed as

$$\mathrm{R}_{\mathrm{D}\rightarrow\mathrm{T}} = \int\int f_{\mathrm{D}}(\mathbf{v}_{\mathrm{D}}) f_{\mathrm{T}}(\mathbf{v}_{\mathrm{T}}) \sigma(\mathbf{v}_{\mathrm{D}}, \mathbf{v}_{\mathrm{T}})(|\mathbf{v}_{\mathrm{D}} - \mathbf{v}_{\mathrm{T}}|) d\mathbf{v}_{\mathrm{D}} d\mathbf{v}_{\mathrm{T}} \tag{1.12}$$

where f_D and f_T are the distribution functions for deuterium and tritium respectively, $\sigma(\mathbf{v}_{\mathrm{D}}, \mathbf{v}_{\mathrm{T}})$ is the cross-section for the D-T reaction which is a function of the velocity of the deuterium particles ($\mathbf{v}_{\mathrm{D}}$) and of the tritium particles ($\mathbf{v}_{\mathrm{T}}$).

The complexity in the integral of equation (1.12) lies in the calculation of the velocity averaged cross-section σ. Many forms of the averaged cross-section exist and they depend on the distribution functions of the deuterium and tritium ions (which are not necessarily the same for non-equilibrium plasmas). However, much of the complexity can be ignored by writing the result of the integral in the following commonly used form

$$R_{\mathrm{DT}} = n_{\mathrm{D}} n_{\mathrm{T}} \langle \sigma v \rangle \tag{1.13}$$

where $\langle \sigma v \rangle$ represents the averaged product of the cross-section and the velocity and is referred to as the reactivity and is a function of the temperature of the plasma. Data and parametrizations exist for the cross-section and the reactivity of a Maxwell distribution plasma [19] which describe the behaviour of the reactivity as a function of temperature.

By taking the reaction rate and the energy released per reaction an expression for the fusion power can be obtained

$$P_{\mathrm{fus}} = \epsilon n_D n_T \langle \sigma v \rangle \tag{1.14}$$

where $\epsilon = 17.2$ MeV for the DT reaction. From this expression we can conclude already that there exists multiple ways to generate fusion energy via trade-offs between the fundamental levers of plasma density and the temperature of the plasma. Also of importance is the confinement time, which is the time before the plasma dissassembles into a low density state. This dissassembly is characterised by a several orders of magnitude drop in the rate of fusion reactions and therefore also in fusion power output. The exact relationship between these fundamentals can be expressed via the Lawson criterion [27] which gives the product of the plasma density n, temperature T, and confinement time τ, required for the energy losses inherent in the plasma to be outweighed by the energy gain due to the fusion reactions.

$$nT\tau \geq 3 \times 10^{21} \quad \mathrm{keV\ s\ /m^3} \tag{1.15}$$

The main energy loss mechanisms are particles transporting energy out of the volume due to loss of confinement, energy lost from the plasma due to electron heat conduction and energy lost by radiation escaping. The Lawson criterion is plotted in figure (1.2) for several different reaction cross-sections against the plasma temperature. As shall be seen in subsequent sections the Lawson criterion does not give a full picture of the ignition mechanism of an ICF fuel capsule as the ignition and propagation of the burn wave generated in an ICF capsule is governed more by the product of the fuel density and the radial extent of the capsule after compression, ρR.

There are currently two approaches to achieving the Lawson criterion, magnetic confine-

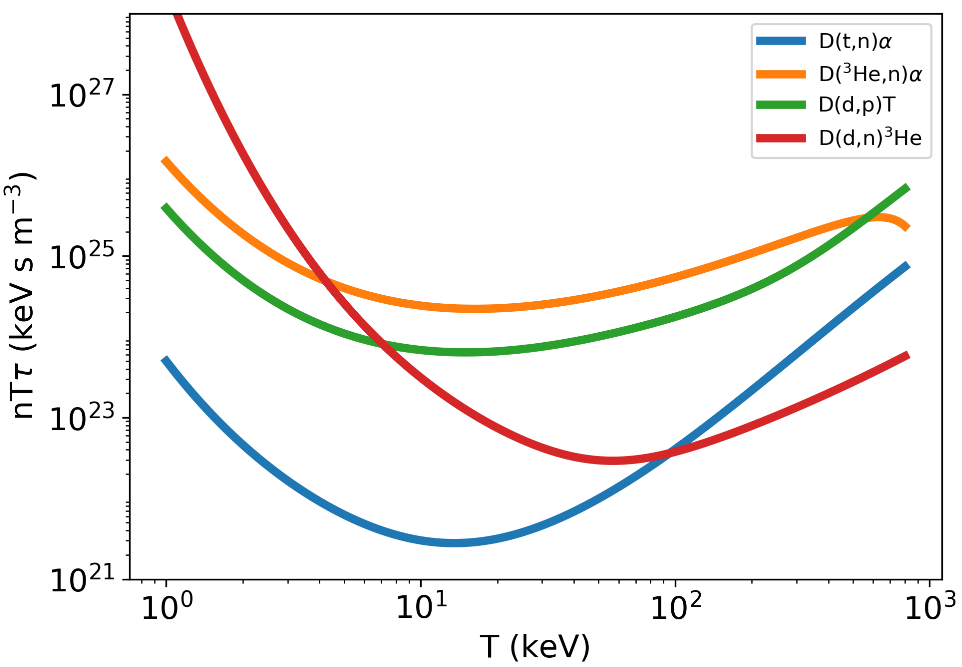

Figure 1.2: The fusion triple-product plotted against plasma temperature for several light-nuclei reactions. The lines represent the value of the triple product necessary to sustain a burning plasma where fusion power is equal to the sum of energy losses from the plasma. One can see that DT fuel provides the most easily accessible burning plasma at the lowest temperatures.

ment fusion (MCF) and inertial confinement fusion (ICF). Though this work concentrates on ICF it is relevant to briefly compare and contrast the two approaches in order to understand the pros and cons of each.

MCF aims to sustain a relatively low-density plasma above the Lawson criterion through heating and confinement for a time ranging from microseconds up to minutes or even hours [28]. This is achieved through an arrangement of magnetic coils which generate the field which confines the plasma. Charged particles interact with a magnetic field according to equation (1.7) which forces charged particles to follow the magnetic field lines thus allowing for a magnetic geometry to be set up that can perpetually confine the particles.

An early device called the magnetic mirror consisted of a tube with a magnetic field that increased in strength towards the ends of the tube. When particles moved towards the ends of the tube they would be reflected by the magnetic field gradient and thus the arrangement could be used to confine particles below a given energy. This concept suffered from particles with high energy escaping the magnetic mirror and thereby lowering the temperature of the plasma. Arrangements that are still finding application in research today are based on a magnetic geometry that is toroidal, so as to remove the possibility for the end-losses present in the magnetic mirror arrangement. In this toroidal geometry the field lines run in circles confining the particles to move in continuous curved trajectories around the torus. The spherical tokamak and the stellarator [29] are two such designs that implement this toroidal geometry. In these devices the primary loss of particle confinement occurs due to perpendicular motion of the particles across field lines and the stability and overall effectiveness of the confinement is heavily influenced by the presence of magnetic instabilities [30] [31]. The tokamak increases the stability of its magnetic field arrangement by introducing a poloidal field component, twisting the magnetic field lines to reduce a type of instability that causes the magnetic field to become deformed. A similar effect is implemented in the stellarator arrangement but rather than generating a new component to the magnetic field the geometry of the magnetic coils in a stellarator is what causes the stabilisation. The shape of the coils are designed to generate fields which twist the plasma without having to rely on the generation of a poloidal magnetic field component.

ICF takes a very different approach to that of MCF by assembling and burning a high density plasma but only for a very short time, on the order of tens of picoseconds [32, 33]. This avoids the need to confine the plasma with magnetic fields as the reactions release enough energy before the disassembly of the capsule is sufficient to significantly lower the number of collisions occuring within the plasma. ICF requires mass densities several hundreds to several thousands times greater than solid density which means that compression of the initial mass is required [34]. To achieve the compression necessary a driver that can produce high pressures is needed. Both lasers, X-rays and particle beams have been explored as drivers for ICF implosions through the generation of ablation pressure with X-rays being the primary source of drive in indirect-drive inertial fusion [35].

1.2 Summary of Work Contained Within

This work includes studies into various aspects of hohlraum and capsule physics applicable to indirect-drive inertial fusion energy. The theory relating to inertial confinement fusion and the description of the simulation methods used within are outlined in Chapter 2 and

Chapter 3. Contained in Chapter 4 is a simulation study into the X-ray conversion efficiency of copper lined hohlraums compared to unlined gold hohlraums with a focus on the ability of a liner to reduce the proportion of high energy X-rays contained within the drive relative to an unlined hohlraum. Chapter 5 is an extension of the work contained in Chapter 4 where 1D capsules are simulated comparing different levels of capsule dopant and X-ray drive combinations in order to understand the potential benefits of a reduced M-band drive on capsule implosion performance. Chapter 6 examines albedo-profiling of the hohlraum wall as a method of increasing X-ray drive symmetry in both laser-driven and Z-pinch driven hohlraums using a view-factor method to calculate radiation symmetry.

Chapter 2

Theory

2.1 Inertial Confinement Fusion

Inertial confinement fusion schemes can be broadly described as being methods of achieving fusion energy gain in which some volume of fuel is burned, where from now burning will refer to thermonuclear burning (i.e. fusion reactions), where a sufficient amount of the fuel is burned (around 33% of the original mass of DT) before the disassembly of the capsule extinguishes the burn [34]. The fact that no external effort is made to confine the fuel and that high pressure gradients exist in such a burning plasma means that the fusion power production from ICF is inherently pulsed with the compression taking place over tens of

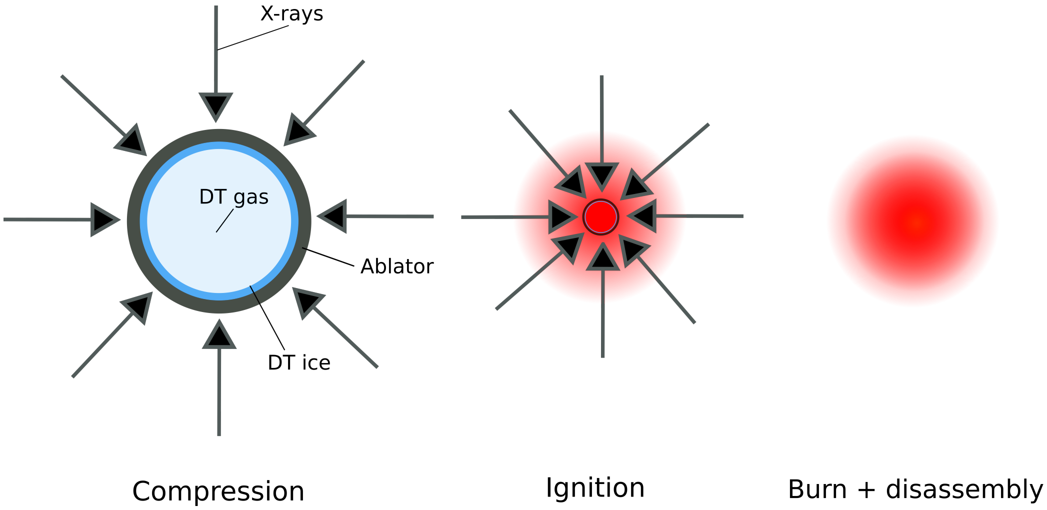

Figure 2.1: Diagram outlining the three main stages of an ICF implosion: compression of the capsule by X-ray or laser radiation, hotspot formation and ignition during the shell deceleration, thermonuclear burn wave propagation into the DT fuel.

nanoseconds and the burn taking place over tens of picoseconds.

In this situation the burning of the fuel needs to occur on a time scale shorter than the time it would take for the plasma to disassemble which can be estimated by considering the size of the fuel mass R and the sound speed $\approx \sqrt{kT/\rho}$. This finite confinement time is an inherent feature of ICF unlike in the case of MCF where the confinement time is another parameter requiring maximization. Most of the fusion power is generated over a few tens of picoseconds whereas a typical fuel mass remains assembled for the time it takes the rarefaction wave to reach some fraction of the way into the fuel.

When considering a volume of DT plasma in isolation we would say that in order to achieve ignition the Lawson criterion must be exceeded, which is most readily achieved by obtaining an ion temperature of approximately 15 keV (see figure 1.2).

The most straightforward way of envisioning this is to heat an entire volume of plasma to 15 keV such that the Lawson criteria is met throughout. If we consider the energy, E_{T}, required to raise N monotonic particles from 0 keV to a given temperature T , assuming an ideal gas, we have

$$E_T = \frac{3}{2} N k_B T \tag{2.1}$$

The fusion energy output of the plasma is can be expressed as

$$E_f = \Phi \frac{N}{2} \epsilon_n \tag{2.2}$$

where the number of DT pairs is $(N/2)$, Φ is the fraction of the DT pairs that undergoe fusion, and ϵ_n is the energy of the neutron released per DT fusion reaction (14.1 MeV). Taking the ratio of equation 2.1 to equation 2.2 for an equimolar mix of deuterium and tritium, including the N electrons gives

$$G = \frac{\Phi \frac{N}{2} \epsilon_D T}{\frac{3}{2} N k_B T_i + \frac{3}{2} N k_B T_e} \tag{2.3}$$

Equation 2.3 gives the energy gain, G, for a volume of plasma. Using a burn-fraction Φ of 0.33 [36], a temperature of 15 keV, and assuming $T_i = T_e$ gives $G \approx 50$.

Compare this gain of $G \approx 50$ for this type of volume ignition with that required to realise break-even energy production in a fusion power plant. This can be estimated by considering the power balance in a plant with the following efficiencies: η_{el}, the efficiency of converting the fusion power into electricity; η_{L}, the efficiency of converting electrical power into laser power; η_C, the coupling efficiency of laser power into heating the plasma.

In order for a fusion power plant to break-even the power input into the system must be equal to the power output. In this case the power output, P_{out}, is the fusion power produced by the plasma, P_f, multiplied by η_{el}. This can be expressed in terms of the gain as

$$P_{\mathrm{out}} = \eta_{\mathrm{el}} G \eta_C P_L \tag{2.4}$$

where P_L is the laser power. As the power input into the system can be expressed as the product of the laser power P_L and the electricity to laser conversion efficiency η_L the break-even condition can be expressed as

$$\eta_{\mathrm{el}} G \eta_C P_L \geq \frac{P_L}{\eta_L} \tag{2.5}$$

Rearranging equation 2.5 to give the required gain gives the following equation.

$$G = \frac{1}{\eta_L \eta_C \eta_{\mathrm{el}}} \tag{2.6}$$

Due to the second law of thermodynamics the value of η_{el} will be limited to around 40% owing to the use of steam turbines to convert the fusion energy into electricity. The current efficiencies for large scale lasers that could be used to heat and compress the plasma are on the order of 1%. Finally, optimistically assuming that all of the laser energy is coupled into the plasma, this results in a required gain for break-even of $G \approx 250$. It can be seen that in this optimistic scenario the gains from heating the entire plasma volume are not sufficient. Though these calculation are only approximate the requirement for high efficiencies to compensate for the low gain makes this type of fusion difficult to apply to a power plant design.

If it were possible to lower the energy required to heat the plasma while keeping the fusion power produced the same the gain could be increased and these requirements of high efficiencies lowered. An approach that implements this line of thinking is known as the 'hotspot-ignition' scheme [37]. In this scheme a small mass of fuel is ignited in the centre of the fuel mass which then through the deposition of the charged α-particle products from the DT reactions raises the temperature of the surrounding dense cold fuel.

A volume of fuel burned via hotspot ignition has two distinct regions, the low density hotspot and the surrounding denser fuel. As safety concerns regarding the surrounding reactor components limit the yield obtainable from a capsule implosion, this puts a limit on the initial mass of the DT fuel. The initial fuel mass is also limited by the driver energy available as driver energy scales with the volume of the fuel. For initial fuel masses of a few hundred micrograms compression of the fuel is required in order to achieve sufficiently high ρR values given these restrictions. In order to generate the required levels of compression requires a powerful driver which is most readily achieved through utilizing a laser or ion beam to drive an ablative rocket. Heating the outer surface of a low-Z material to high temperatures ablates the outer surface and causes a reaction force to drive the remaining mass inwards, hence the term ablative rocket.

Once the outer shell begins to slow as the implosion stagnates the kinetic energy of the imploding shell is transferred to the hotspot and the compression of the cold fuel. If the ρR of the fuel is sufficient to confine the hotspot and if, ignoring all forms of energy loss from the hotspot, the ρR of the hotspot is greater than the stopping length for the 3.6 MeV alpha particles in DT ($\rho R = 0.3$ g/cm^2) then the alpha particles will 'bootstrap' the heating of the hotspot and rapidly increase the temperature of the hotspot. Once this occurs and the hotspot reaches approximately 50-80 keV alpha particles are no longer stopped primarily in the hotspot but travel and deposit their energy into the surounding dense fuel. The hotspot alphas propagate a distance R_α into the surrounding cold dense DT such that $\rho_{DT} R_\alpha = 0.3$ g/cm^2. The energy contained within the hotspot alpha particles, $E_{\alpha,\mathrm{hs}}$, required to raise the temperature of the cold layer of surrounding DT fuel can be approximated as

$$E_{\alpha,\mathrm{hs}} \geq 4\pi R_{\mathrm{hs}}^2 R_\alpha \rho_{DT} c_{\mathrm{DT}} \Delta T \tag{2.7}$$

where R_{hs} is the radius of the hotspot, c_{DT} is the specific heat capacity of DT, ΔT is the change in temperature required in order for the DT to become transparent to the alpha particles and ρ_{DT} is the density of the DT fuel surrounding the hotspot. This layer of cold DT is then heated by the hotspot alphas and this process repeats creating a thermonuclear burn wave propagating from the initial central hotspot. In reality the condition that the ρR of the hotspot is greater than the mean-free-path of the alphas in order for ignition to be achieved does not hold exactly as one should also consider the power balance of the hotspot. Deformation of the hotspot durng the implosion can increase the surface area and therefore increase electron heat conduction losses. In addition, turbulence in the hotspot can mix fuel from the surronding layers that may contain higher Z impurities thus increasing bremsstrahlung radiation losses. These two effects will cause the hotspot to cool and therefore reduce the effect of alpha particle bootstrapping on raising the hotspot temperature.

Assuming the stated ρR conditions on the hotspot and an implosion kinetic energy sufficient to raise the hotspot temperature to > 10 keV [36] the hotspot will ignite and burn the surrounding fuel. The yield however, that is the amount of energy that is obtained from fusion reactions, is determined by the actual fraction of the initial DT fuel that is burned. We can imagine this as a competition between the thermonuclear burn wave travelling outwards from the hotspot and the rarefaction wave that travels inwards, lowering the ρR of the fuel.

The burn fraction can be determined by integrating the fusion reaction rate, which can be obtained from equation 1.14 assuming an equimolar mix of deuterium and tritium,

$$\int_0^{t_b} \frac{dn}{dt}dt = \int_0^{t_b} \frac{n^2}{2}\langle\sigma v\rangle dt \tag{2.8}$$

Defining the time after ignition until capsule breakup as the time when the rarefaction wave moves a third of the radius, R, toward the centre, so $t_b \approx R/3c_s$, equation (2.8) can be integrated, assuming values for the reactivity, to give the burn fraction $\Phi = 2n(t = tb)/n(t = 0)$ as

$$\Phi = \frac{\rho R}{\rho R + 6} \tag{2.9}$$

where ρR is in g/cm^2. The choice of setting a radius of $R/3$ as the cut-off for fuel disassembly is based on the fact that in the hotspot ignition scheme most of the dense fuel region surrounds the hotspot, closer to the outside of the assembled fuel at a radius of approximately $2R/3$. From equation (2.9) we arrive at ρR of 3 g/cm^2 for a target of 33% burn fraction [36].

2.1.1 Indirect-drive

ICF experiments that use direct illumination of the target with lasers or other directed energy sources are classed as direct-drive whereas experiments that first use lasers or ion beams to generate X-rays through an intermediate target, such as a hohlraum, are classed as indirect-drive. The X-rays then go on to compress the capsule through a similar ablative rocket effect as in the case of direct illumination with lasers with some subtle differences in terms of absorption of the X-rays within the capsule ablator plasma. The target capsule in this case is comprised of a spherical shell usually made from low-Z compounds, such as Be or CH, filled with deuterium-tritium gas and cooled to low temperatures in order to form a solid DT ice layer on the inside surface of the low-Z shell [38, 39].

There are several reasons for using an indirect X-ray drive over directly illuminating the capsule with lasers. Firstly, the spatial smoothness and the symmetry of the drive has a large effect on the efficiency of the implosion. A directly-driven capsule requires that the lasers are precisely arranged in order to achieve a uniform illumination over the entire capsule surface. Laser-plasma instabilities that occur between the lasers and low-density coronal plasma surrounding the capsule can scatter energy away from the intended location resulting in an non-uniform compression and reduced energy yields [40]. In an indirect-drive experiment the lasers interact with the hohlraum wall and generate X-rays which then are confined within the hohlraum through multiple emission and absorption events occurring within the high-Z wall of the hohlraum. These multiple emission and absorption events act to thermalize the X-ray spectrum and also increase the spatial uniformity of the X-ray radiation by smoothing any high order non-uniformity that originates from the non-uniform heating by the lasers.

Furthermore, in direct-drive, laser-plasma instabilities such as stimulated Raman scattering and two-plasmon decay can create a population of high energy electrons which in addition to scattering energy from the laser deposition site can, due to their high energy, penetrate into the capsule and preheat the DT fuel [41, 42]. This increases the internal pressure of the fuel making it harder to compress and leads to reduced yield. Hot-electron generation remains an issue in indirect-drive through interaction of the laser with the low-Z coronal plasma, the high-Z hohlraum wall and the gas that fills the hohlraum [43].

Finally, the laser beams used to illuminate the capsule have an inherent spatial non-uniformity to the cross-section of the beam intensity which originates from the lasing process and the optical assembly. These non-uniformities can imprint onto the capsule ablator seeding hydrodynamic instabilities which then grow and effect the stability of the capsule [44]. They may then cause mixing of fuel-ablator material, break-up of the capsule [45] and introduce variations in shock velocity [46]. Methods exist for smoothing the intensity cross-section of laser beams used in direct and indirect drive [47]. Despite this the imprint of intensity non-uniformity onto the capsule surface is still a negative by-product of direct illumination of the capsule with lasers. It is for this reason, the lack of seeding of hydrodynamic instabilities, that indirect-drive is preferable to direct-drive despite the inefficiencies introduced by using a hohlraum as an intermediary source to generate the X-rays.

For these reasons primarily, and due to the large amount of experimental data available for indirect-drive, it was chosen as the scheme to pursue on the National Ignition Facility and is the main focus of this work.

2.1.2 The Hohlraum

A commonality between these various inertial fusion schemes is that they all require a well characterised energy source driving the capsule with high coupling between the drive and the capsule in order to maximise the compression available at a minimal energy cost. With this in mind, in the case of indirect-drive it is important to understand the processes by which the laser energy is converted into X-rays by the hohlraum and how the spectral energy distribution of these X-rays affects the overall implosion of the capsule. It is also of interest to consider how the hohlraum as a whole can be modified to provide a better environment for X-ray generation.

Hohlraums consist of a high-Z cavity surrounding the capsule, see Figure 2.2 the shape of which is decided based on a number of factors, one being the required geometrical smoothing of the radiation drive as determined by the need to generate a spherical implosion. Geometrical smoothing refers to the process by which radiation that is emitted by the hohlraum wall maps onto the capsule surface. For example, a capsule driven by a large hohlraum that contains small non-uniformities in the radiation field at the surface of the hohlraum wall will experience a reduction in the non-uniformity of the radiation field at the outer ablator surface. In general, the greater the distance from the source containing the non-uniformities the greater the smoothing of said non-uniformity. The case-to-capsule ratio is the ratio between the diameter of the hohlraum and the diameter of the capsule and is a determiner of the amount of geometrical smoothing.

The hohlraum is also designed with the path and deposition location of the lasers in mind. For cylindrical hohlraums there exist two laser entrance holes (LEHs) covered in a plastic window. This window keeps the gas within the hohlraum until the target is illuminated by the lasers. The lasers enter through the laser entrance holes and deposit their energy on the inside of the hohlraum wall heating it and generating X-rays. An important reason for

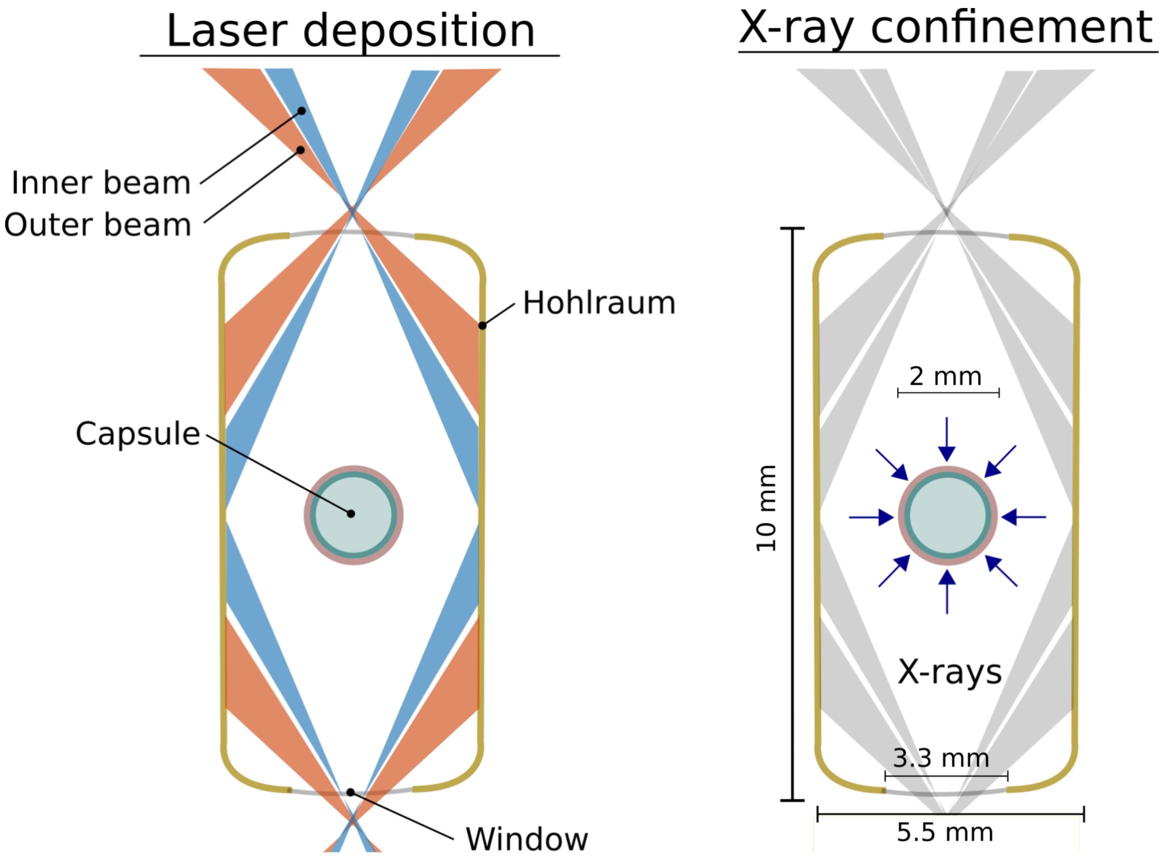

Figure 2.2: Diagram of an indirect-drive hohlraum showing inner beams, outer beams, capsule and window (left) for a cylindrical hohlraum. X-rays are produced by laser absorption and are confined in the high-Z hohlraum due to the high opacity of the hohlraum wall material (right). An example of the dimensions of the hohlraum and capsule for a cylindrical hohlraum are included in the figure.

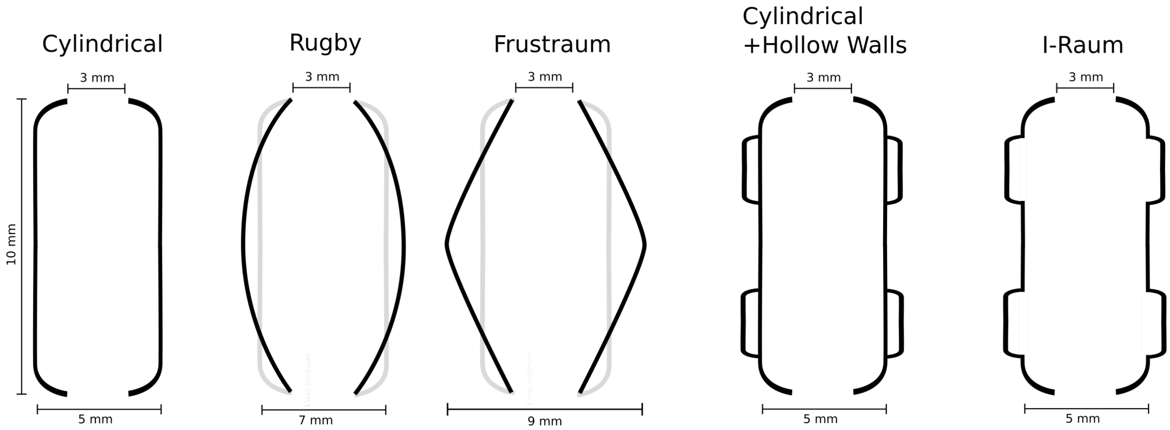

Figure 2.3: Diagram showing Cylindrical, Rugby, Frustraum, Cylindrical with hollow walls, and I-Raum hohlraum geometries with approximate dimensions included

choosing a cylindrical hohlraum over a spherical hohlraum is the fewer laser entrance holes and simpler beam arrangement required to achieve a uniform illumination of the capsule. Laser hotspots created at the spot on the hohlraum wall where the laser is incident need to be distributed such that the capsule is irradiated uniformly by the X-rays. To do this easily in a spherical hohlraum more than the two laser entrance holes (LEH) required by a cylinderical hohlraum are needed. This increases the amount of X-ray energy lost to the LEH in a spherical hohlraum versus a cylindrical hohlraum. In addition, the required number and arrangement of beams increases ablation of the hohlraum wall near the LEH resulting in faster closure of the LEH.

Several novel hohlraum designs are being investigated in addition to the cylindrical hohlraum which aim to increase drive symmetry and improve laser propagation and deposition, see Figure 2.3. One such design is the rugby hohlraum which is an intermediary between a cylindrical and spherical hohlraum [48]. Rather than the straight walls of a cylindrical hohlraum, the rugby hohlraum has curved walls that result in a smaller surface area for the same hohlraum diameter compared to a cylinder. With the cylindrical hohlraum and the rugby hohlraum having the same laser entrance hole diameters this results in a lower laser power required to achieve the same radiation temperature for the rugby hohlraum. The curved walls also aid in the propagation of the inner beams due to the hotspot plasma from the outer beams being set further back compared to the cylindrical hohlraum. As well as the rugby hohlraum the spherical hohlraum is also being pursued with laser entrance hole closure being mitigated by the development of novel laser entrance hole designs [49] [50].

More recently, efforts have been focussed on increasing the propagation of the laser beams by altering the hohlraum geometry. For example, designs with hollow walls located at the laser hotspots have been investigated in order to reduce the expansion of the hotspot plasma by allowing it to expand into the hollow area [51]. The I-Raum has a similar design with recessed regions at the laser hotposts, giving its cross-section the shape of a capital "I" [52]. These recesses mean that the plasma starts expanding at a greater distance from the axis of the hohlraum than in previous designs. This results in more time for the beams to propagate in the hohlraum before the expanding plasma begins to impede.

Finally, the "Frustraum" [53] has been proposed, a hohlraum composed of two truncated cones with their largest ends joined at the waist. This geometry allows for larger capsules and therefore allows a greater amount of energy to be absorbed by the capsule. Additionally, the Frustraum geometry means that beams can impact the surface of the Frustraum at a glancing angle thus increasing the amount of specular reflection. These reflections can then be leveraged to increase the irradiation symmetry as they redeposit their energy into the hohlraum wall.

In addition to pursuing energy production, hohlraums have applications in a number of interesting fields of research including the study of astrophysical plasmas [54], neutron sources for diagnostics and security applications [55], nuclear stockpile stewardship [56], the study of warm-dense matter [57], and opacity, equation of state and phase transitions under extreme conditions [18].

2.2 Hydrodynamics

2.2.1 Fluid Equations

The equations of fluid dynamics provide a basis for modelling the flows of plasma inside a hohlraum by considering the plasma as comprised of many small volumes. Each volume should contain enough particles such that random fluctuations in the quantities is low. The standard error of a sample size, N, scales with $1/\sqrt{N}$ so the standard error scales with the characteristic length of the volume, L, as $L^{-3/2}$. To ensure equillibrium within the volume the fluid volume should also be larger than the mean-free-path of the particles, λ. Using these volumes and their averaged values as an approximation is useful as it allows large systems of particles to be modelled without needing to track each particle individually. A distribution function describes how a number of particles are distributed in a specific space. A commonly used assumption for the velocity distribution function of particles is the Maxwell-Boltzmann distribution, which assumes that the particles are in thermal equillibrium

$$f(v) = \left(\frac{m}{2\pi k_B T}\right)^{3/2} \exp\left(-\frac{mv^2}{2k_B T}\right) \tag{2.10}$$

where v is the speed of the particle, m is the mass of the particle in kg and T is the temperature in Kelvin of the distribution. Equation (2.10) when multiplied by the phase space volume dx^3dv^3 gives the number of particles with speed, v, given a temperature, T. It is this temperature T, which defines the shape of the distribution function, that is referred to as the temperature of the plasma. All particle distributions given enough time tend towards the Maxwell-Boltzmann distribution due to collisions within the collection of particles if the rate of collisions between particles in the distribution is high enough to smooth out any effect of collective heating processes.

Several quantities can be obtained from the distribution function such as the average speed $v_{av} = \sqrt{8k_BT/\pi m}$. The average value of a quantity q can be acquired by performing the following integration over the 3-dimensional velocity space d^3v

$$\langle q \rangle = \int_0^\infty q f(v) d^3v \tag{2.11}$$

With these assumptions of volume averaged quantities and well defined particle distribution functions the equations of fluid dynamics can be formed based on conservation laws. However, this approach does have limitations since it relies on the particles in the volume following a velocity distribution that has a well defined temperature. A complication that can arise that breaks this assumption is non-local transport. Heat diffusion occurs in the plasma where temperature gradients exist and takes place on the scale of the particle's mean-free-path, assuming this mean free path is smaller than the scale length of the temperature gradient. Mechanisms in the plasma that selectively heat a population of particles to a higher temperature can result in a significant number of particles having a much higher mean-free-path than those in thermal equillibrium. This higher mean-free-path can exceed temperature gradient scale lengths resulting in non-local heat transport, breaking the assusmption of diffusion.

The equations for conservation of mass, momentum and energy can be obtained by considering the force and energy balance on a infinitesimal volume containing particles that can be described by a distribution function having a single temperature.

$$\frac{D\rho}{Dt} = -\rho\frac{\partial v_i}{\partial x_i} \tag{2.12}$$

$$\rho\frac{Dv_i}{Dt} = -\frac{\partial p}{\partial x_i} + \frac{\partial \tau_{ij}}{\partial x_j} \tag{2.13}$$

$$\rho\frac{D}{Dt}\left(e + \frac{1}{2}v_i v_i\right) = S - \nabla\cdot\mathbf{q} - \frac{\partial}{\partial x_i}pv_i + \frac{\partial}{\partial x_j}\tau_{ij}v_i \tag{2.14}$$

where ρ is the mass density, v is the fluid velocity, p is the hydrostatic pressure, e is the specific internal energy, S is the heat added from volume sources, $\mathbf{q}$ is the heat flux vector, τ is the viscous stress tensor, and the material derivative is defined as

$$\frac{D}{Dt} = \left(\frac{\partial}{\partial t} + \mathbf{v}\cdot\nabla\right) \tag{2.15}$$

The first term in equation (2.15) represents the local variations of a quantity inside a specific volume of the fluid. The second term is the advection term and represents the variation of a quantity at a certain location in space due motion of fluid into and out of that location. These two terms make up the material derivative which is a convenient shorthand describing how a given quantity changes along the flow trajectory of a fluid volume.

The fluid equations (2.12, 2.13, 2.14) assume that the conditions on the volume of fluid elements and the distribution function hold. It is also assumed that mass, momentum and energy is conserved. The viscous stress tensor τ_{ij} is represents the forces on the fluid volume due to partiucles diffusing across the boundaries encountering regions of plasma that have a different velocity. Collisions occur and momentum is transfered accross the boundary resulting in heating of the plasma. The viscous stress tensor contains nine terms to account for the three spatial dimensions on which particles can leave the fluid volume and the three velocity dimensions for each particle. τ_{ij} differs from the hydrostatic pressure, p, as it required the fluid to have relative motion between fluid elements in order for the viscous stress to be present.

In the momentum equation (2.13) the two terms on the RHS describe the change of momentum due to local gradients in the hydrostatic pressure and the viscous-stress tensor respectively. The locality of the theory is an important issue to keep in mind as it will necessitate modifications in order to correctly incorporate non-local transport, particularly non-local heat transport which is very present in high energy laser-plasma experiments.

The form of the energy conservation equation in (2.14) makes the purpose of the terms on the RHS clear. The first, S is a general term representing sources of energy into the volume, for example laser deposition. The second term is the energy escaping the volume due to heat transport from electrons or any other particle species within the plasma fluid. The final two terms on the RHS describe processes which involve the deformation of the volume; the first is the energy lost due to expansive work driven by the hydrostatic pressure, the second is the viscous heating due to velocity gradients between neighbouring fluid volumes.

In order to solve this set of equations another is required that describes the relationship between the pressure in the fluid and the density and temperature. An example of such a relationship can be taken from the ideal gas equation of state given by

$$P = nk_BT \tag{2.16}$$

where P is the pressure, n is the number density of particles, k_B is the Boltzmann constant and T is the temperature. The equation of state can also be taken from tabulated values that may contain either or both experimental data and results from computational modelling.

This formulation of the fluid equations is known as the Eulerian form and serves to describe the evolution of the fluid from a frame of reference separate from that of the fluid motion (lab frame). Sometimes, a more useful form of the fluid equations is the Lagrangian form, which shifts the frame of reference to one co-moving with the fluid. In 1-D this frame transforms the equations into the form

$$\frac{dV}{dt} = \frac{dv}{dm} g(x) \tag{2.17}$$

$$\frac{dv}{dt} = -\frac{dp}{dm} g(x) \tag{2.18}$$

$$\frac{d\left(e + \frac{1}{2}v^2\right)}{dt} = \frac{S}{\rho} + \left(\frac{d(pv)}{dm} - \frac{dq}{dm}\right) g(x) \tag{2.19}$$

where the specific volume is $V = 1/\rho$ and m is the mass defined here for a simple 1-D slab geometry as

$$dm = \rho g(x) dx \tag{2.20}$$

where $g(x)$ has units of area and depends on the geometry of the problem, $g(x) = 1$ for slab geometry, $g(x) = x$ for cylindrical and $g(x) = x^2$ for spherical. In the Lagrangian formulation the mass in a fluid volume dV is conserved and the fluid elements are tracked through a *mass coordinate* denoted here as ϵ such that

$$dm = \rho(x,t) g(x) dx = \rho(\epsilon, 0) g(\epsilon) d\epsilon \tag{2.21}$$

This approach is very useful for situations where there is a need to maintain and track material boundaries and when there are shocks present in the fluid. Due to the presence of shocks in the capsule during implosion and the multiple material boundaries solving the fluid equations in their Lagrangian form is a popular approach and the one utilised by the codes used in this work, **HYADES** and **h2d** [58].

2.2.2 Hydrodynamic Instabilities

Important to understanding many of the decisions taken in the design of the capsule and pulse is an understanding of the hydrodynamic instabilities that the capsule is susceptible to during the implosion. The most important of these instabilities is the Rayleigh-Taylor instability which occurs when a fluid is supported by a less dense fluid [59]. Any perturbation to the boundary between the two fluids will grow until turbulent mixing occurs [60]. The interface between these two fluids can be described by the Atwood number, A

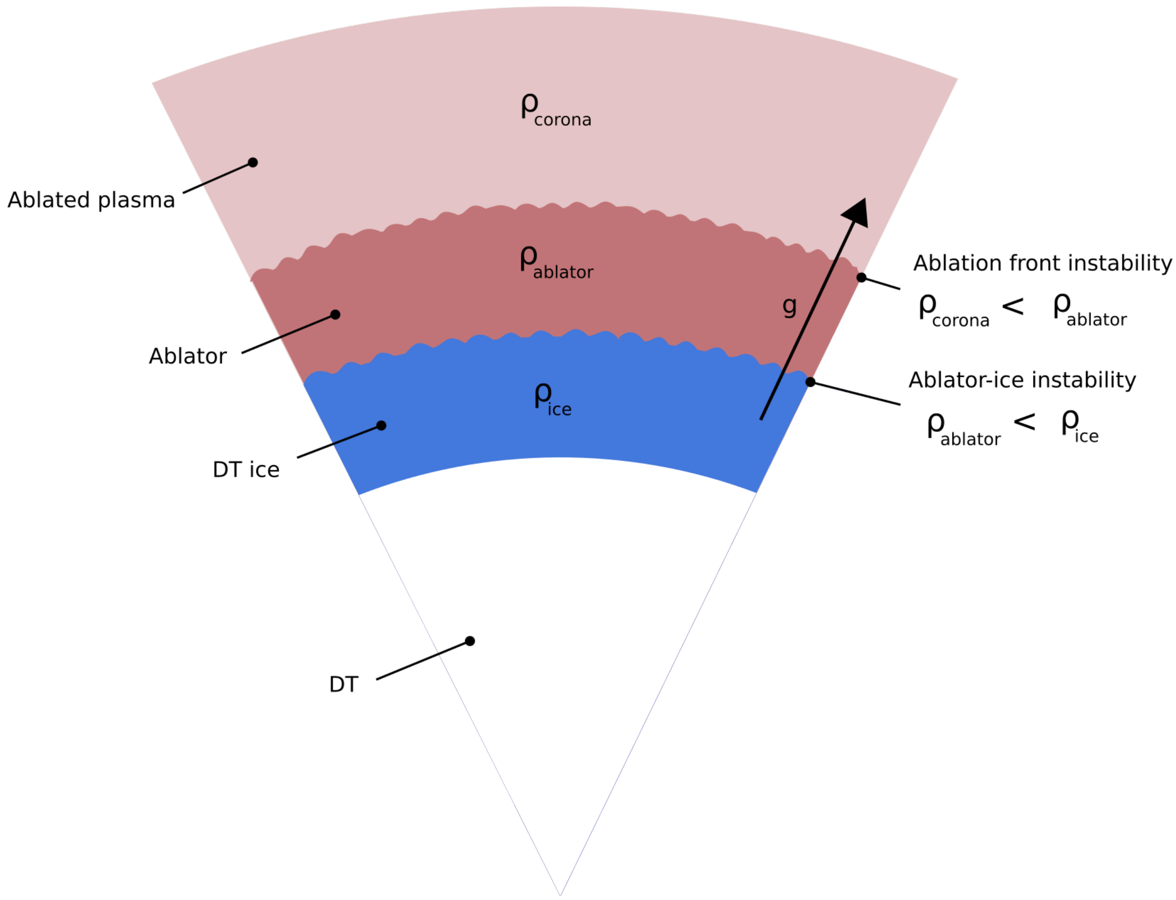

Figure 2.4: Figure showing a cross section segment of an ICF capsule with layers corresponding to the ablated plasma, ablator, DT ice and DT included. Two interfaces that may become unstable to Rayleigh-Taylor instabilities during the implosion are indicated, the ablation front and the boundary between the ablator and the DT ice. The direction of the acceleration in the frame of reference of the imploding capsule g, is also indicated.

$$A = \frac{\rho_1 - \rho_2}{\rho_1 + \rho_2} \tag{2.22}$$

where ρ_2 is the density of the supporting fluid and ρ_1 is the density of the fluid being supported. We can see that in the case of a more dense fluid supporting we have a stable Atwood number less than zero. Whereas in the case of a lighter fluid supporting, the Atwood number is greater than zero and describes a situation where the instability can occur.

There exist several such boundaries in the capsule during the implosion process (see Figure 2.4 , for example the ablation front. Here the outer material of the ablator is heated by the X-rays, creating a hot, low-density plasma corona which drives the rest of the capsule inwards. If we transform our frame of reference to be stationary with respect to the boundary between the cold capsule material and the ablated plasma we see that due to the acceleration of the boundary in the lab frame the situation is analogous to the cold capsule material being supported by the low-density coronal plasma. This means that the boundary is unstable and any initial perturbation in the boundary will grow in time. These initial perturbation arise from multiple sources; the target fabrication process produces capsules with a certain surface roughness, the tent and fill tube cause large perturbations to the capsule surface, non-uniformities in the X-ray drive can imprint non-uniformities onto the capsule surface [61]. Other such boundaries within the capsule are the ice-ablator boundary where the solid DT ice layer meets the inner layer of the ablator. Due to heating via high energy X-rays or by hot electrons the ice-ablator interface can become unstable to the Rayleigh-Taylor instability causing deformation of the fuel hotspot and mixing of ablator material and DT [62, 63].

There is a benefit to using an ablative rocket as the means to drive the capsule. Perturbation modes that grow through the Rayleigh-Taylor instability can be suppressed due to them being transported away from the unstable region through the ablation of the capsule. Also, the interface between the two fluids in reality will have a finite density gradient scale length which also tends to reduce the instability growth rate as given by the equation [64].

$$\gamma_{abl} = \alpha\sqrt{\frac{kg}{1+kL}} - \beta k v_a \tag{2.23}$$

where k is the wave number, g is the acceleration of the ablator, L is the minimum density scale-length and v_a is the ablation velocity. The constants α and β depend on the heat conduction and the Froude number $Fr = v_a/\sqrt{gl}$, which is the ratio of the inertia of the fluid to the acceleration over some characteristic length l for thermal diffusion. α and β can be obtained from hydrodynamic simulations of the capsule ablation.

Looking at the equation (2.23) for the growth rate of perturbations of wave number k via the Rayleigh-Taylor instability we can see that there is a competition between the growth of the perturbation, represented by the first term in equation (2.23) , and the transport of the perturbed plasma away from the boundary, represented by the second term in equation (2.23) . This process is known as ablative stabilisation and decreases the growth rate significantly for high wave number (short wavelength) modes of the instability. In addition, the first term in equation (2.23) includes a reduction in the growth rate due to the density scale length for short wavelength modes (kL $\gg$ 1).

2.3 Radiation Transport

The high power lasers used in inertial confinement fusion often generate plasmas that are opaque to the X-rays within the hohlraum, this is an essential property of the plasma within the hohlraum if radiation confinement and therefore high radiation temperatures are to be obtained. It is important then to know how this radiation is transported within not only the hohlraum wall but the capsule ablator also, where it is absorbed to drive the implosion. The field of radiation transport within plasmas has been investigated [65], [66] but remains a complex and computationally expensive process depending on the plasma state.

If we model the radiation as a ray where the position along the ray has the coordinate s we can write an expression for the specific intensity of the radiation I_ν at given frequency as [66]

$$\frac{\partial I_\nu}{\partial s} = \epsilon_\nu - \kappa_\nu I_\nu + \frac{1}{c}\frac{\partial I_\nu}{\partial t} \tag{2.24}$$

where ϵ_ν is the specific emission of the plasma at a given frequency (in units of J m^{-2} sr^{-1} s^{-1} Hz^{-1}) , κ_ν is the absorption coefficient with units of m^{-1}. The first term represents the radiation source from the plasma along the ray at each point while the second term accounts for absorption of radiation by the plasma. The final term in equation (2.24) is the contribution of the changing plasma during the journey of the ray. Only in very rapidly changing plasmas does this term have any effect and can be neglected for the radiation conditions found in a hohlraum where the laser pulse power changes over hundreds of picoseconds which is much greater than the time taken for radiation to travel its mean-free-path (on the order of picoseconds).

These calculations are complicated by the fact that the atomic energy level populations are influenced and in turn influence the radiation field. Assuming a plasma in local thermodynamic equilibrium (LTE) [67] means that the energy level populations can be described by the Fermi distribution

$$P_i = \frac{1}{\exp\{E_i - \mu\}/k_B T} + 1 \tag{2.25}$$

where P_i is the probability of an electron occupying state i, E_i is the energy of the state i, μ is the amount of energy released/required to add an electron to the system known as the chemical potential, and T is the temperature of the plasma.

This approximation assumes that the plasma can be adequately described as having a defined temperature within a specific volume which if the collision frequency of the electrons is high enough will be met and then the free electrons in the plasma can be described by a Maxwellian distribution. Also required is the assumption that the electronic excitation and de-excitation rates are dominated by collisions. We can then say that the bound electrons arrange themselves according to equation (2.25). One final requirement is that the plasma is optically thick, meaning that the mean-free-path of the radiation is much shorter than the typical density scale length in the plasma. With these conditions met the radiation field can be described as being in equilibrium with the plasma at a temperature T and thus follows the Planckian distribution

$$B(\nu, T) = \frac{2h\nu^3}{c^2} \frac{1}{\exp(h\nu/k_B T) - 1} \tag{2.26}$$

where $B(\nu, T)$ gives the spectral radiance in units of J s^{-1} m^{-2} sr^{-1} Hz^{-1} with ν being the radiation frequency. Often these assumptions are not valid, for example when the plasma is not optically thick or when collective heating processes skew the electron energy distribution. In these situations in order to find the energy level populations P_i the rate equations describing the excitation and de-excitation processes should be solved for.

In the case of optically thick plasmas, like the plasma found in the high-Z hohlraum wall, the radiation can be assumed to be isotropic and the diffusion approximation can be used. This results in a Fick's law relating the radiation flux, $\mathbf{F}$, to the radiation energy density, u

$$\mathbf{F} = -\frac{1}{3\sigma_t} \nabla u \tag{2.27}$$

here σ_t is the total opacity for scattering and absorption in units of m^{-1}, $\mathbf{F}$ the flux integrated over the solid angle Ω, $\mathbf{F} = \int \mathbf{\Omega} I_\nu d\mathbf{\Omega}$, and $u = \int I_\nu d\Omega$.

2.3.1 Bremsstrahlung and Inverse-bremsstrahlung

As the primary function of the hohlraum in inertial confinement fusion is to generate and confine X-rays the radiative processes that occur determine several aspects of the X-ray drive and overall performance of the target. At several locations within the hohlraum the types of processes and their magnitude vary greatly and evolve in time as the hohlraum fills with plasma and the intensity of the laser changes. Of primary importance are the radiative processes which occur at the hohlraum wall and in the laser hotspot region as this is where the conversion of laser energy into X-rays takes place.

Most of the laser energy at incident laser intensities of $10^{14} - 10^{15}$ W cm^{-2} is absorbed via inverse-bremsstrahlung in the laser hotspots. Inverse-bremsstrahlung is the transfer of laser energy to the electrons via electron-ion collisions and so is directly tied to the electron-ion collision frequency. This occurs in the under-dense high-Z plasma of the hohlraum wall where the coefficient of absorption due to inverse-bremsstrahlung has the following form [68]

$$\kappa_{\text{brem}} = 3.10 \times 10^{-7} Z n_e^2 \ln\left(\frac{v_{th}}{\Omega\Lambda}\right) T^{-3/2} \omega^{-2} \left(1 - \frac{\omega_p^2}{\omega^2}\right)^{-1/2} \tag{2.28}$$

$$\Omega = \max \begin{cases} \omega \\ \omega_p \end{cases} \tag{2.29}$$

$$\Lambda = \max \begin{cases} Ze^2/k_B T \\ \hbar/\sqrt{m_i k_B T} \end{cases} \tag{2.30}$$

where Z is the ionization state, n_e is the electron density, v_{th} is the electron thermal velocity, m_i is the ion mass and T is the plasma temperature. The inverse bremsstrahlung absorption increases with increasing laser frequency, ω, with an upper cut-off of the plasma frequency ω_p. The term $\hbar/\sqrt{m_i k_B T}$ in equation 2.30 represents a relativistic correction for high plasma temperatures.

At high laser intensities ($> 10^{14}$ W cm^{-1}) inverse-bremsstrahlung can alter the electron distribution function and thereby lower the amount of energy transferred from the laser into the electrons [69]. This occurs when the electrons cannot relax via collisions fast enough to create a Maxwellian distribution. This creates a distribution skewed towards higher energies thus reducing the overall number of electron-ion collisions and therefore the amount of inverse-bremsstrahlung heating. This exemplifies the often coupled nature of laser-plasma interactions within the hohlraum and how in a number of situations a kinetic theory analysis, for example with a Fokker-Planck code [70], is required.

As inverse-bremsstrahlung is the transfer of energy from radiation into free electrons, bremsstrahlung is the radiation by free particles of that energy into X-rays. Bremsstrahlung is a process whereby a photon is emitted by a free electron while in the electric field of an ion. The spectrum of X-rays produced is a continuum with a cut-off at the plasma frequency and a peak that depends on the temperature of the plasma.

Bremsstrahlung radiation is produced throughout the target and is a strong function of temperature but is mainly of interest at the time of hotspot formation within the capsule as this is when it becomes a dominant source of energy loss from the fuel. In other regions of the hohlraum the power radiated via bremsstrahlung is much lower than that of other mechanisms.

2.3.2 Recombination

Recombination radiation is the radiation emitted by a free electron that combines with an ion to fill a vacant energy level thus becoming a bound electron. The difference between the energy of the bound state the electron now occupies and the energy it had as a free particle becomes the energy of the emitted photon. There is therefore a cut-off energy in the spectrum for recombination radiation for a given atomic energy level, the value being the energy of the level. The power radiated by recombination radiation [71, 72] can be expressed as

$$W_r = 1.69 \times 10^{-32} n_e T_e^{1/2} \sum_i \left(Z_i^2 n_i \left(\frac{E_{Z-1}}{T_e} \right) \right) \quad \text{W cm}^{-3} \tag{2.31}$$

Where Z_i is the ionization state of the ion, n_i is the number density of the ion with ionization state Z_i, n_e is the number density of the electrons and T_e is the electron temperature. The power radiated due to recombination, W_{re}, can be compared to the power radiated due to bremsstrahlung, W_b, in a hohlraum

$$\frac{W_{\mathrm{re}}}{W_b} \approx 32.64 \frac{Z^2}{T_e} \tag{2.32}$$

where T_e is in units of eV. For high atomic numbers, like those used in the hohlraum, the power radiated by recombination is several orders of magnitude greater than that radiated by bremsstrahlung.

2.3.3 Line Emission

The final main contributor to radiative processes in the hohlraum emission from bound-bound transitions within ions. Calculation of this radiation is complex as the rates are dependant not only on the energy of the transition but of the occupancy of the electronic states, which are time dependent. The energy of the photon released as a consequence of an electron falling from a higher energy level to a lower one is equal to the difference in energy between the two levels. The energy for the level corresponding to the principle quantum number, n, in a hydrogen-like atom can be expressed as

$$E_n = -\frac{13.6 Q_n^2}{n^2} \quad \text{eV} \tag{2.33}$$

where Q_n is the screened nuclear charge as seen by the electron in the nth energy level. For atoms with $Z > 1$ the charge of the nucleus is screened by electrons in energy levels above and below n. Electrons are excited to higher energy levels in the hohlraum plasma by electron collisional excitation and by photon absorption excitation mechanisms.

2.4 Atomic Physics

2.4.1 Hydrogenic Average Atom Model

Several approximations can be used to simplify the calculation of the atomic physics occurring in the plasma, one common one being the average-atom approach [73]. This approach is integrated into radiation-hydrodynamics simulations due to it's relatively low computational cost and its ability to reproduce experimental results for opacities of low Z elements.

The approximation uses an 'average atom' as a representation of all the atoms in a given cell of the simulation domain rather than the alternative of modelling a distribution of atoms with various ionization states and electron level populations [74]. This greatly simplifies calculations and fits well with the fluid representation of the plasma already utilized in rad-hydro simulations. From here the energy levels can be calculated with a hydrogenic model that takes into account electron screening effects. This simple model works well for low Z elements but runs into issues when Z becomes large as electron screening becomes an important factor as well as many body transitions [75].

The average atom model involves either solving for the equilibrium energy level populations (LTE) or obtaining the energy level populations by solving the rate equations (non-LTE). These rate equations represent the balance between physical processes occurring within the plasma that excite, de-excite and ionize electrons from various energy levels within the fictional 'average-atom'. The atomic energy level populations can be time dependent and are solved for using an equation of the form

$$\frac{dN_i}{dt} = \sum_j W_{ji} N_j - \sum_j W_{ij} N_i \tag{2.34}$$

where N_i is the population of energy level i and W_{ji} and W_{ij} is the de-excitation rate from energy level j to i for an electron and the excitation rate from level i to j respectively. The calculation of the W rates in equation (2.34) is quite involved and can include contributions from electron-impact excitations [76][77], atom-atom collisional ionization [78], radiative transitions [79] and dielectric transitions [80].

Two examples of average atom models used to perform calculations of atomic states in ICF relevant plasmas are the XSN [81] and DCA [75] models. The XSN model assumes that each electron has an energy corresponding to the principal quantum number, n, of the energy level they occupy and that this energy is independent of the number of electrons that occupy that level. The XSN model calculates the rates for radiative transitions between bound and free electrons and also the elastic and recombination collisional transitions. The DCA model is an extension of the XSN model that includes a greater number of processes such as electronic transitions within principal energy levels ($\Delta n = 0$) and dielectronic processes. The DCA model has been shown to more accurately reproduce conditions in the hohlraum due to the importance of the dielectronic and $\Delta n = 0$ transitions.

2.4.2 M-band

The laser hotspots in high-Z hohlraums are heated to several keV during the pulse compared to the hundreds of eV that the remaining wall area is heated to by the thermal X-rays. In addition to the thermal X-rays, which at peak laser power can reach temperatures of 300 eV, the hotspots in high-Z hohlraums produce higher energy X-rays which can degrade capsule performance. In a common hohlraum wall material such as gold these high energy X-rays originate from the M-band (n=4→3) electronic transitions [82]. Photons emitted due to M-band transitions in gold sit in the 2-3 keV range and due to their higher energy can penetrate much deeper into the capsule than the thermal X-rays.

In order to model such a radiation field a multi-group radiation transport method is required as the assumption of a Plankian radiation field of temperature T_R does not hold. The rate equations governing the populations of electrons within the various atomic energy levels also need to be solved in a time-dependent manner in order to model the M-band transitions occuring in the laser hotspots.

2.5 Radiation Hydrodyamics

As the walls of the hohlraum are heated by the incoming lasers both the motion of the hohlraum wall and the capsule can be calculated by considering a fluid model of the plasma. Energy is firstly delivered into the hohlraum by the laser beams but the majority of the energy transport within the hohlraum is due to radiation emission and re-emission of the X-rays produced in the laser hotspots. Radiation transport is also the means by which the X-ray energy is transported to the capsule where the shell is then ablated. Also of importance is the calculation of the propagation of the radiation into the high-Z hohlraum wall as this determines the effectiveness of the radiation confinement. Therefore, as the heat transport within both the hohlraum and the capsule is dominated by radiation transport it is necessary to model both the hydrodynamic motion and the radiation transport in a self-consistent way via radiation-hydrodynamic models.

As previously discussed the fluid motion can be solved by using the Lagrangian fluid equations (2.17), (2.18) and (2.19). Radiation transport with the plasma can be solved by using the equation of radiative transfer, equation (2.24). However, in order to solve both consistently then coupling terms are required which will account for energy transferred between the matter and the radiation field. Equation (2.24) accounts for this in the first two terms on the right-hand side, $\epsilon_\nu - \kappa_\nu I_\nu$, which represents the net energy gain of the radiation field (and therefore the net energy lost from the matter) per solid angle Ω, per unit frequency ν, per unit volume.

The coupling term that takes the place of S in the fluid energy conservation equation, equation (2.19), is therefore

$$S_R = -\int (\epsilon_\nu - \kappa_\nu I_\nu) d\nu d\Omega \tag{2.35}$$

Likewise, using the fact that radiation pressure can be obtained by dividing the radiation energy density by the speed of light, the following term can be added to the right-hand side of the fluid momentum conservation equation, equation (2.18),

$$P_R = -\frac{1}{c}\int(\epsilon_\nu - \kappa_\nu I_\nu)d\nu\hat{x}d\Omega \tag{2.36}$$

where $\hat{x}$ is the unit vector in the x direction for the one dimensional example used in equation (2.18). Though in radiation hydrodynamics the radiation pressure source term is included it is not the radiation pressure in the hohlraum that is the main driver of the capsule implosion. The pressure generated by the radiation heating the ablator shell is several orders of magnitude larger.

2.6 Shocks

Shocks occur in a medium when a sharp discontinuity in pressure forms. This discontinuity emerges from a pressure wave due to the dependence of its sound speed on the pressure. This is a non-linear effect that is only relevant for strongly driven waves that will have high enough pressures for this non-linearity to develop. Take, for example, a 1-D rod that has a pressure wave driven through it by a source at one end. After the initial pressure disturbance has been set up it will move through the rod — mediated by interaction forces between the atoms, radiation transport and other energy transferring mechanisms such as plasma waves. For a pressure wave of high amplitude the phase velocity at the peak of the wave is higher than at the trough and this will cause it to catch-up to the lower pressure region of the wave that precedes it. This process causes a pressure discontinuity to form at the front of the wave resulting in two clearly defined regions: un-shocked material ahead of the shock front, shocked material behind the shock front. This discontinuity in reality is smoothed out via energy transport away from the shock front due to heat conduction and radiation transport. The thickness of the shock front is governed by the mean-free-path of the particles transporting energy accross the shock front, be they electrons or photons.

Shocks are an essential component of inertial fusion as they are how high levels of compression are achieved and how the shell is accelerated. In an ICF experiment the pulse shape and capsule are designed such that the timing and strength of shocks is such that a minimal amount of entropy is introduced into the capsule. In order to fully understand the implosion process a simple single shock in 1-D planar geometry can be examined. Obtaining expressions for the mass, momentum and energy across the shock boundary allows us to arrive at the well known Hugoniot conditions [83, 84]

$$\rho_0 v_{x,0} = \rho_1 v_{x,1} \tag{2.37}$$

$$\rho_0 v_{x,0}^2 + p_0 = \rho_1 v_{x,1}^2 + p_1 \tag{2.38}$$

$$v_{y,0} = v_{y,1} \tag{2.39}$$

$$\frac{1}{2}(v_{x,0}^2 + v_{y,0}^2) + h_0 = \frac{1}{2}(v_{x,1}^2 + v_{y,1}^2) + h_1 \tag{2.40}$$

where h is the specific enthalpy, $h = e + pV$ with e being the internal energy and $V = 1/\rho$ the specific volume. Subscripts 0 and 1 refer to the upstream and downstream material conditions respectively. Pressure and enthalpy can be calculated from the equation of state which can be in the form of an expression, such as the ideal gas equation ($P = nk_bT$), or a table derived from experimental data and computational models.

Equation (2.37) is the mass conservation condition across the shock front. The momentum conservation across the shock is represented by equations (2.38) and (2.39) which account for the momentum parallel and normal to the direction of the shock respectively (for our planar geometry). Equation (2.40) is the energy conservation which contains a kinetic energy term and an enthalpy term, h, where enthalpy is defined as the sum of internal energy and pdV work.

Re-arranging the Hugoniot conditions gives several useful equations describing the conditions up and downstream of the shock. Of particular interest in inertial confinement fusion is the change in entropy, Δs, in the shocked material.

$$\Delta s = 9.6 \times 10^7 \ln\left(\frac{T_0/T_1}{(p_0/p_1)^{(\gamma-1)/\gamma}}\right) \quad \mathrm{J\,keV^{-1}\,g^{-1}} \tag{2.41}$$

where T_i and p_i are the upstream and downstream temperatures and pressures respectively. The ratio of specific heats, γ, for an ideal monotonic gas is 5/3. In a plasma the value of γ may be much lower due to processes that effect the internal energy of the plasma such as ionization [85]. From equation (2.41) it is clear that a powerful shock driven into cold matter will introduce a lot of entropy into the fuel thereby raising it's pressure and reducing the effectiveness of the compression. If we wish to achieve high levels of compression the pressure of the fuel must remain as low as possible and so the entropy added to the fuel by the shocks must be minimised.

The minimum pressure of a gas containing Fermions is given by the Fermi pressure which results from the filling up of energy states due to the Pauli exclusion principal. Due to the finite number of phase states available for fermions to occupy at low temperatures a fermion gas will have an internal energy of $E_T = \frac{3}{5}E_F N$ where N is the number of fermions, m is the mass of the individual fermions, V is the volume they occupy, and E_F is the Fermi Energy

$$E_F = \frac{\hbar^2}{2m}\left(\frac{3\pi^2 N}{V}\right)^{2/3} \tag{2.42}$$

The pressure generated by this internal energy can be expressed as the Fermi pressure

$$P = -\frac{\partial E_T}{\partial V} = \frac{(3\pi^2)^{2/3}\hbar}{5m}\left(\frac{N}{V}\right)^{5/3} \tag{2.43}$$

As the Fermi pressure is inversly proportional to the mass of the fermion the majority of the degeneracy pressure is generated by the electrons in the plasma. The Fermi pressure can be expressed in terms of the plasma density ρ and can be used to express the pressure of the fuel

$$P = S(\Delta s)\rho^{5/3} \tag{2.44}$$

where S is some function of the entropy introduced into the fuel by the shocks. At $\Delta s = 0$ equation (2.44) equals the Fermi pressure thus giving a ratio of the fuel pressure to the ideal Fermi pressure equal to 1. This ratio is referred to as the adiabat [38], α, of the capsule and gives a way of quantifying how far away the fuel is from an ideal compression.

The entropy introduced by a single powerful shock can be large, a shock driven by a sharp rise in radiation temperature to 300 eV generates a relative change in entropy more than twice that of a pulse consisting of several incrementally increasingly powerful shocks. This combined with the limit on the levels of compression achievable with a single shock leads to the requirement of a shaped drive pulse consisting of several steps in drive pressure that produce multiple shocks which maintain a low fuel adiabat. Even in the case of a smooth ramp up to a high peak drive pressure after a certain time shocks can form due to pressure steepening [86]. Shocks are a necessary feature of inertial confinement fusion due to the need for ablation of the capsule outer shell in order to generate the pressure that drives the compression. Direct drive requires laser intensities $> 10^{14}$ W cm^{-2} in order to efficiently convert laser energy via inverse-bremsstrahlung and electron heat conduction. Indirect-drive also requires similarly high laser intensities for efficient conversion of laser energy into X-rays in the hohlraum.

Each shock travels through the capsule with a shock velocity, v_s, that is dependent on the upstream sound speed as well as the ratio of the downstream pressure to the upstream pressure.

$$v_{\mathrm{s}} = v_{x,0} + c_0\sqrt{1 + \frac{\gamma+1}{2\gamma}\left(\frac{p_1}{p_0} - 1\right)} \tag{2.45}$$

where $c_0 = \sqrt{\gamma p_0/\rho_0}$ is the upstream sound speed. This results in the more powerful shocks catching up to and overtaking the preceding shocks. If the spacing of the pressure steps in the drive pulse are not spaced correctly then any number of shocks may merge inside the ablator. Shock merger results in the material ahead of the newly merged shock seeing a larger pressure difference and as a result more entropy is introduced. Studies have been undertaken into shock timing [87, 88, 89], and the effect of pulse shape on determining the adiabat of the fuel [90]. Variations on the shock timing due to experimental uncertainty on the timing and height of the peaks in the drive can cause shocks to become mistimed. The equation of state at the high pressures found in inertial fusion capsules is less well understood than at lower pressures due to the difficulty in obtaining high pressure conditions in experiments [91]. The requirement of detailed knowledge of the equation of state of the capsule materials coupled with this experimental uncertainty means that an iterative experimental approach is required in order to get the shock timings to within an acceptable tolerance.

In the first capsule implosion experiments on the NIF initial pulse shapes consisted of a 4-shock structure with a relatively low initial rise to 70 eV known as the ‘foot’ of the pulse, see Figure 2.5 . The foot creates the greatest jump in entropy as it is represents the largest difference in pressure versus the pressure of the cryogenic capsule. This jump in pressure is necessary for initially ionizing the capsule ablator and creating the initial conditions for the subsequent shocks, for example causing material state changes in the ablator. Thus the foot is important for setting the overall adiabat of the fuel. It also sets the first shock travelling through the capsule and therefore determines the shock timing. The optimal timing sees all four shocks merging just inside the DT ice layer as this prevents the issue previously stated

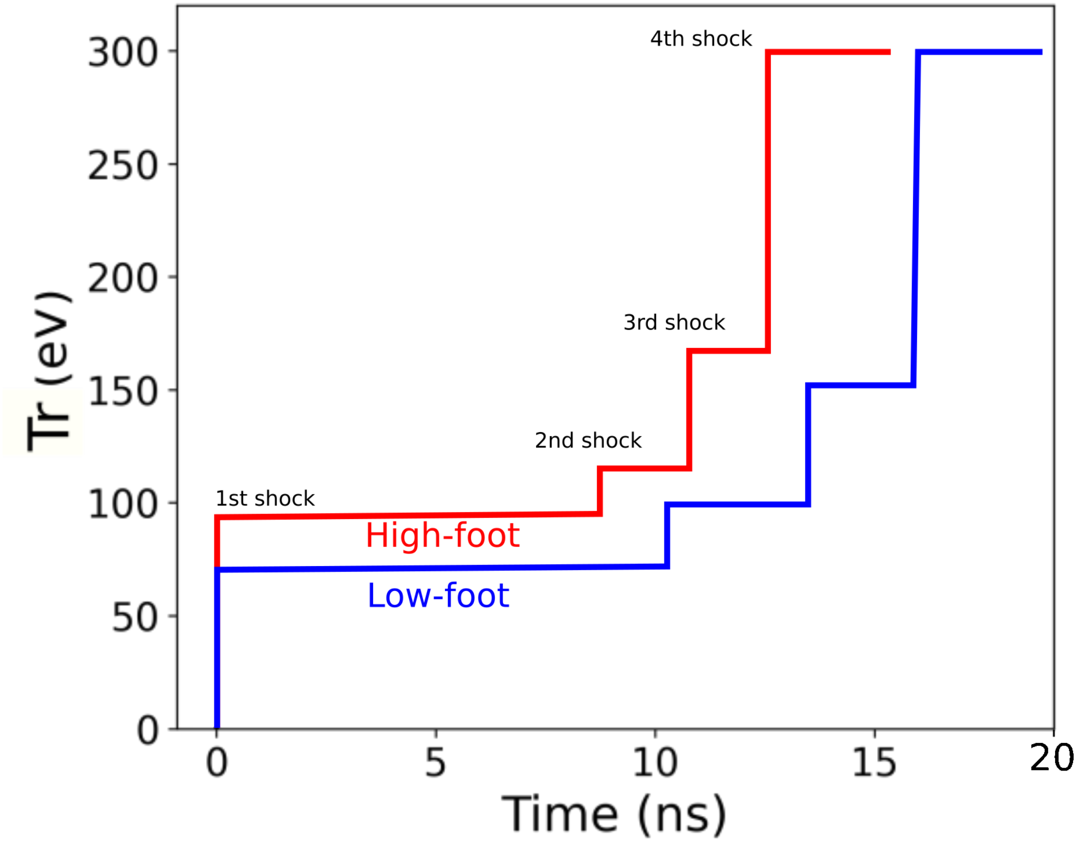

Figure 2.5: Figure showing the characteristics shapes of the high (red) and low (blue) foot pulse shapes used in inertial confinement fusion with shocks labelled.

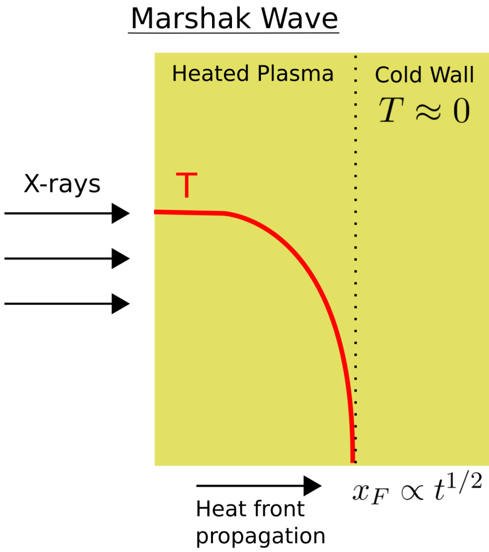

Figure 2.6: Diagram showing a Marshak wave propagating into the cold wall of a hohlraum with the heat front position, x_F, wall temperature T, and heat front position scaling $x_F \propto t^{1/2}$ included.

of an enhanced pressure ratio and also ensures that limited expansion of the DT ice inner surface occurs, which could also cause an unwanted increase in the fuel adiabat [88].

The first experimental campaign on the NIF saw these 'low foot' 4-shock pulse shapes being used [92, 38] while recent experiments, alongside changes to the capsule material and dimensions [93], have seen pulses with higher foot radiation temperatures upwards of 100 eV [94, 95, 96, 97] resulting in implosions with a higher fuel adiabat. Adiabats for the low-foot pulses are around $\alpha = 1.5$ while high-foot pulses can have adiabats $\alpha > 2$.

2.7 Marshak Waves

X-rays generated in the laser hotspots fill the hohlraum and penetrate into the cold high-Z walls. This penetration of X-rays in to the walls represents a heat flux q that, for materials where the mean-free-path of the X-rays is small compared to the scale of temperature gradients within the wall, can be expressed as

$$q = -K\nabla T \tag{2.46}$$

where K is the conduction coefficient and T is the temperature. The mean-free-path assumption used here holds in the high-Z gold walls of a hohlraum due to its high opacity to the thermal X-rays produced in the laser hotspots. Equation (2.46) is complicated by the fact that the conduction coefficient for the radiation depends strongly on the temperature of the material. The conduction coefficient for radiation has the following form

$$K \propto \frac{T^3}{\chi_R} \tag{2.47}$$

where χ_R is the Rosseland mean opacity, which is assumed to follow a power law and has the scaling $\chi_R = \chi_0 \rho^\alpha T^{-n}$. The result of this dependency of the radiation conductivity coefficient on temperature is that a sharp temperature front develops in the wall as the heat front deposits its energy. For a heat front moving from left to right, if we assume that the hohlraum wall has a temperature of zero, then the position of the heat front can be defined as the rightmost position where the wall temperature is non-zero. The deposition of energy raises the temperature of the material at the heat front thus increasing its radiation conduction coefficient. This feed-back results in a sharp temperature gradient at the heat front.

Assuming that the speed of the heat front propagating into the wall is much larger than the speed of the wall expansion near the heat front then the wall can be assumed to have a constant density. Marshak developed solutions to this type of heat conduction problem, replicating the sharp rise in the temperature at the heat front by imposing an exponentially increasing temperature boundary condition there [98]. Radiation heat waves of this type are known as Marshak waves and have a characteristic scaling of the heat front position, x_F, of $x_F \propto t^{1/2}$, see Figure 2.6.

2.8 Margin for Ignition

Establishing the relative performance between particular target designs, both capsule and hohlraum, in inertial confinement fusion is of great importance. However, numerous factors influence the performance of a capsule implosion and between designs there can exist a large parameter space where gaps in simulation modelling and experimental uncertainties conspire to obfuscate the exact conditions of experiments. This is where complex simulations that can integrate the dynamics of the hohlraum with the laser absorption and the hydrodynamics of the capsule implosion find use as post-experiment analysis tools of difficult to observe experimental variables.

These simulation tools by themselves often fail to predict implosion performance and often require post hoc adjustments. In order to evaluate the distance a particular design is from ignition and to plot the course of target design towards that goal several implosion metrics have been proposed. The advantage of this approach is that simple scalings taken from analytical solutions can inform basic trends one expects in the target performance. Then more detailed experimental studies can generate scaling laws composed from multiple variables. This 'experiment first' method where an area of design space is explored then designs are modified, guided by scaling laws, gives a way of moving in the direction of ignition in spite of some physics being missing in the models.

There will exist an amount of energy that is required to create conditions sufficient for igniting the fuel capsule. For a capsule to achieve ignition the ρR of the hotspot must be at least the stopping length of the fusion alpha particles in order for the bootstrapping effect to occur. The hotspot must also be at a high enough temperature such that the sum of energy lost via mechanisms such as Bremsstrahlung is lower than that deposited by the alpha particles. These impose upon the ignition energy a dependence on the hotspot ρR and the hotspot temperature T respectively. In addition, there will be a dependency on the adiabat of the capsule, α, as a higher adiabat implies a higher pressure which will require more energy to achieve the required compression. Finally, to achieve the ρR condition the capsule needs to be compressed and so a dependence on the radius of the hotspot is introduced. The radius of the capsule can be linked to the in flight aspect ratio (IFAR) $R/\Delta R$ which is the radius of the capsule divided by the thickness of the shell. This in turn depends on the velocity of the implosion [99]

$$v = \alpha^{0.6} T_r^{0.9} \frac{R}{\Delta R} \tag{2.48}$$

where T_r is the radiation temperature of the drive. Scalings such as this are useful but due to the complex conditions in the hotspot at stagnation simulations are required in order to create scalings that better capture the physics. An example of such a scaling law is given by the following equation, which expresses the margin for ignition, M, as a function of the kinetic energy of the capsule, E_{kin}, the energy required to ignite the hotspot, E_{ign}[100], the adiabat of the DT fuel, α, the outer radius of the capsule before compression, R, and the peak implosion velocity, v.

$$M = \frac{E_{\text{kin}}}{E_{\text{ign}}} \propto \alpha^{-1.9} R^3 v^{7.9} \tag{2.49}$$

Equation (2.49) can be used to assess how changing the adiabat, capsule outer radius and peak implosion velocity alters the kinetic energy required for ignition. A margin of $M = 1$ implies that the kinetic energy of the fuel, which is converted into the internal energy of the hotspot, is equal to the energy required to ignite the hotspot. It can be seen from equation (2.49) that the strongest lever for achieving the margin for ignition is increasing the velocity of the implosion. This scaling also shows that larger capsules - greater fuel mass capsules - have a lower margin for ignition due to the lower levels of compression required to achieve the required ρR. This may be the case but capsule size is ultimately determined by the available laser energy and any increase in capsule size independent of the hohlraum leads to a loss in drive symmetry. Recent results, however, have shown that increasing the size of the capsule can increase the amount of energy absorbed by the capsule thus increasing the hohlraum-capsule coupling efficiency [101].

2.9 Inertial Fusion Progress and Challenges

The National Ignition Facility (NIF), located in California, is the largest facility of it's type dedicated to achieving ignition of an inertial fusion target via compression with lasers. The 192 beams of the NIF converge on a target chamber to deliver upwards of 2 MJ of laser energy onto the target. The footprint of the entire NIF facility covers around three football pitches with most of the space taken up by the laser amplification beam-lines and spatial filters. Beam-lines have a square cross-section and after amplification are frequency-tripled to 0.35 μm. The beams then enter the spherical chamber in two hemispheres and are focused onto the hohlraum target, which is around 1 cm in size.

NIF began with planar target experiments utilizing four of the NIF beamlines in order to measure laser performance and examine aspects of laser-matter interaction. Radiation-hydrodynamics codes were benchmarked against X-ray radiography data from laser-solid interactions and initial findings were positive in the sense that they did not predict any majorly detrimental effects due to hydrodynamic instabilities [102].

First experiments on the NIF focussed on achieving high compression via pulses designed to keep the fuel on a low-adiabat and drive four shocks into the fuel, timed such that they converge at the DT fuel-ice interface. These experiments suffered from a number of deficiencies; the major ones being 3-D hydrodynamic instabilities caused by capsule surface imperfections and features due to the supporting FOAMVAR tent and fill tube [103]. Other issues included hot electron generation [104] by the lasers causing preheating in the capsule, lowering the efficiency of the implosion and introducing asymmetries. Cross-beam energy transfer, a laser plasma instability that occurs inside the hohlraum, also resulted in asymmetry of the laser deposition onto the hohlram walls [105].

In order to mitigate the problems of the first set of high-convergence low-adiabat implosions a ‘high-foot’ design, see Figure 2.5, was developed [95, 94, 97]. These experiments used pulses designed to drive three shocks into the capsule and to introduce more entropy into the ablator via a higher first pulse peak (picket). This pulse design also puts the DT fuel on a higher adiabat where the adiabat, α, is defined as the ratio of the pressure of the DT to the ideal Fermi pressure of the DT at a 1000 g/cc reference density $\alpha = P/P_{\text{Fermi}}$. A high adiabat means that more entropy has been introduced into the fuel and therefore lower convergence ratios can be achieved due to the higher fuel pressure. This has the effect of reducing the achievable convergence ratio and thus reduces the impact of hydrodynamic instabilities seeded by capsule surface and material interface defects. Driving the capsule harder also results in a higher ablation velocity and therefore more stabilization of Rayleigh-Taylor instabilities, as can be seen in equation (2.23).

In an effort to reduce laser-plasma instabilities and to improve laser deposition and drive symmetry near-vacuum hohlraums have been fielded on the NIF [106, 107, 93]. These low gas-fill hohlraums typically have He densities of 0.1 mg/cc and employ short laser pulses out of necessity due to the laser becoming impeded by hohlraum wall plasma earlier. High density carbon ablators have been used as their high density (3.5 g/cc) relative to the conventional plastic ablators (1.0 g/cc) means that thinner ablator shells can be used and driven by shorter pulses due to the shorter distance the shocks need to traverse.

Near-vacuum hohlraum experiments have demonstrated symmetry tuning of the implosions by directly altering the balance of power between NIF’s inner and outer cone beams rather than by relying on CBET for time-dependant symmetry control [106]. As CBET is difficult to calculate in the complex, evolving environment of the hohlraum, direct tuning of power is a preferred way of imposing symmetry control onto the capsule and is most effective in this low gas fill environment where CBET is minimal.

While near-vacuum hohlraums have been successful in improving the laser-hohlraum coupling by reducing LPIs there are still modelling discrepancies in capsule performance relative to 1D and 2D implosion metrics and also in late time laser-hohlraum coupling where inner cone propagation is overly impeded in radiation-hydrodynamic simulations [107]. Kinetic physics also plays an important role in the dynamics governing several aspects of indirect-drive, from LPIs in the hohlraum to mass and energy transport within the capsule [108].

Some of the modelling discrepancies brought to light and exacerbated by the near-vacuum hohlraum experiments have led to so-called intermediate fill experiments which use a hohlraum gas fill density lying somewhere between the original fills fielded in the first campaign and the near-vacuum experiments [109]. In these experiments the value was chosen in order to retain some of the low CBET symmetry control and low levels of LPIs afforded by the near-vacuum hohlraums while decreasing the rate of high-Z hohlraum wall plasma fill and bringing experimental results more in line with simulations.

Recently, experiments on the NIF have obtained neutron energy yeilds exceeding 50kJ and have entered the regime where alpha heating begins to dominate the energy deposition in the hotspot [110].

In order to increase the yield there are various avenues of physics being considered such as increasing the target energy coupling efficiency to drive up the efficiency of the target [53, 101, 111] and increasing the hydrodynamic stability of the capsule and reducing the impact of perturbations caused by the fill tube and tent [112, 113]. ”Hybrid B” and Hybrid E” campaigns have been conducted using designs that bring together elements from previous campaigns in order to further increase capsule performance [114][115]. A major element of the Hybrid-E being an increased capsule size relative to the hohlraum in order to increase coupling. There is also indication that these efforts have lead to ignition potentially being achieved on the NIF with the recent, at the time of writing unpublished, 1.3 MJ yield result recorded in August 2021. This experiment produced an internal hotspot energy more than three times that of previous similar experiments, enough to achieve the alpha heating of the hotspot required for ignition. If this result is repeatable then a major milestone in inertial confinement fusion will have been achieved as it will have been shown that the central hotspot ignition scheme can create a viable thermonuclear burn in spite of Rayleigh-Taylor instabilities and other deleterious effects. This result would not be the end however, as gains can still be made on yield and the overall energy efficiency of the target necessitating further work in the areas previously outlined.

Chapter 3

Methods

3.1 HYADES and h2d

3.1.1 Physics Description

H2d is a code developed by John Larsen [58] that can be used for many applications in high energy density physics. The code solves the fluid equations on a Lagrangian mesh while calculating ionization levels, atomic physics, laser deposition and radiation transport. In addition the code provides multiple options for sources such as radiation and velocity sources. Tabulated equation of state and opacity data from SESAME tables or other external tables can also be used.

HYADES can operate in slab, cylindrical and spherical geometry while h2d operates in R-Z geometry. R-Z geometry assumes that the problem is symmetric about the Z axis (along the length of the cylinder) which is applicable to the cylindrical hohlraum being simulated in this work. For the HYADES 1D capsule simulations a spherical geometry is used, the first (R=0) boundary is fixed and the outer boundary is free to expand as the ablation progresses. The 2D hohlraum simulated using h2d uses the R-Z cylindrical geometry. The hohlraum is defined in the upper half of the R-Z plane, h2d then treats this as if it were rotated around the Z axis. In order to simplify the mesh at the laser entrance holes the mesh curves outwards, see Figure 3.3. This reduces the degree of mesh entanglement at the laser entrance holes as the hohlraum wall plasma is ablated. Radiation that leaves the outer cells is lost from the system, similarly laser rays that leave the compuational mesh and do not re-intersect it are considered lost from the system. All outer mesh boundaries in the hohlraum are allowed to freely expand.

HYADES and h2d solve the fluid equations in the Lagrangian form, see Section 2.2.1 which results in a moving computational mesh that conserves mass in each of the respective cells. The electrons and ions are each treated as separate fluids and are coupled together via collisions. The electron-ions collisions are modelled via a Spitzer collision model [116] that contains corrections due to electron degeneracy effects. In order to deal with shocks that may emerge in simulations, an additional viscosity term is added to the fluid equations. As the physical mechanisms that transport energy across the shock front occur on spatial scales often much smaller than the size of the computational cells a discontinuity forms. This artificial viscosity is applied in order to increase the thickness of shock fronts in the simulation as the presence of discontinuities will result in un-physical growth of acoustic oscillations in the simulation. The artificial viscosity term in HYADES and h2d is proportional to the square of the velocity gradient and therefore only grows large at shock fronts.

In order to close the system of fluid equations information on the pressure and specific energy of the plasma is required. HYADES and h2d utilise equation of state data tables created by external simulation tools that incorporate experimental data and complex models that would be impractical to include in a radiation hydrodynamics code. The SESAME library [152] contains equation of state data on several relevant materials to indirect drive and is utilised throughout this work.

Radiation transport within h2d is handled using a diffusion approximation, see Section 2.3. This approximation is accurate for optically thick plasmas such as are found in the high density re-emission region. This assumption breaks down in the lower density laser hotspot plasma but as the bulk of the radiation transport within the hohlraum will take place within the re-emission region it is deemed a reasonable approximation for this investigation. Diffusive transport does however tend to smooth out spatial variations in the radiation flux leading to a prediction of higher X-ray drive symmetry. As comparisons are being made between two hohlraum designs (even with the smoothing effect of a diffusive radiation transport model) there should still be meaningful conclusions that can be reached. The key outputs being measured by this investigation is the energy content of the drive and of the spectral distribution and so a diffusive model is sufficient. An alternative approach is to use a Monte Carlo method for simulating the radiation such as is used to simulate experiments on the NIF [117]. This involves discretizing the radiation into packets of photons that

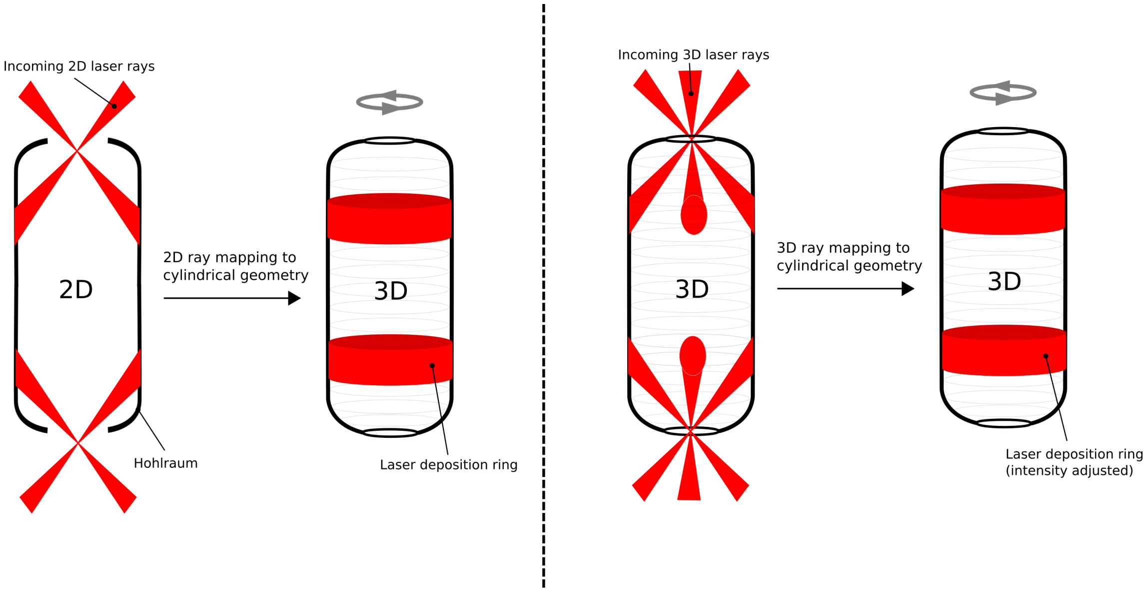

Figure 3.1: Diagram showing how rays are mapped in the HYADES simulation. (Left) rays are described with 2D coordinates and then mapped onto the cylindrical geometry in rings. (Right) rays are specified in 3D and then the deposition is smeared onto the cylindrical geometry in rings in order to obtain the correct intensity.

travel through the plasma and at each each point on their traversal have a probability of being scattered or absorbed. This method is computationally expensive as it requires many photon packets to be tracked within the simulation but has the advantage of more accurately representing the radiation field. This is particularly true in situations where the radiation is not in local thermodynamic equilibrium with the plasma and when the field cannot be assumed to be isotropic.

The radiation field is binned into groups with each group covering an energy range specifed by the user. Absorption coefficients are then calculated by sampling the material opacity at the frequency of each group. This method makes no assumption about the photon energy distribution and allows each group its own mean free path. This is important to model in non-LTE plasmas particularly when we are aware than a high energy population of M-band generated X-rays exist.

Laser deposition can be calculated in the 2D cylindrical R-Z geometry by specifying ray coordinates and directions in either 2D or 3D. The 2D raytracing of the laser beams entering the hohlraum through both laser entrance holes results in two rings of deposition on the inside of the hohlraum. In order to obtain the correct intensities the rays can be specified in 3D coordinates. H2d then can take the 3D rays and calculate deposition onto the 2D cylindrical geometry. This method of specifying 3D rays to be used in a 2D simulation allows the energy and intensity of the laser beams to model the actual deposition that would occur in several individual laser hotspots, see Figure 3.1.

The coefficient of laser absorption, η_{las}, in the laser hotspots is calculated via inverse bremsstrahlung, see Section 2.3.1. Rays propagate through the plasma until they reach the critical density and are reflected, depositing an amount of energy due to resonance absorption, depending on the angle of incidence. Laser reflections causing deposition on other areas of the hohlraum wall are confined to early times where the laser absorption efficiency of the wall is low. As the wall material is ionized the inverse bremsstrahlung co-efficient rises and reflected laser energy drops. For this investigation the energy reflection is negligible due to the rise time of the laser pulse.

Radiation transport within the hohlraum is dependent on the ionization states of the material in which the radiation is travelling. Calculating these states requires an atomic physics model that can account for the plasma in the high-Z optically thick region of the hohlraum re-emission region and the optically thin mid-to-high-Z laser conversion region. Rather than assume local-thermodynamic equillibrium (LTE) h2d can solve the time-dependent rate equations and therefore model the optically thin plasma in the conversion region. HYADES and h2d both utilise a hydrogenic average atom atomic physics model, see Section 2.4.1.

The optical mean-free-path in the gold re-emission region where the Marshak wave travels is short. For the case of a gold wall an LTE model can be used for the re-emission region. However, for the laser conversion region in the gold a non-LTE model is required which solves the time-dependent rate equations due to the higher optical mean-free-path.

Solving the rate equations is also required in the mid-Z liner featured in Chapter 4, see Figure 3.2. At early times in the simulation the mid-Z liner will contain the laser conversion region and the X-ray re-emission region. Due to the lower opacity of the liner the re-emission region will not be as optically thick meaning that the assumption of LTE and of a pure Marshak wave will be less valid. At later times the re-emission region will consist primarily of the gold wall and therefore the LTE approximation is sufficient.

Non-local transport effects that arise due to steep gradients in the laser plasma and the presence of high energy electrons complicate modelling laser heated plasmas [118] as they are not easily accounted for in radiation hydrodynamics codes [119]. As the mean-free-path of the electrons grows relative to the gradient scale length of the plasma non-local transport

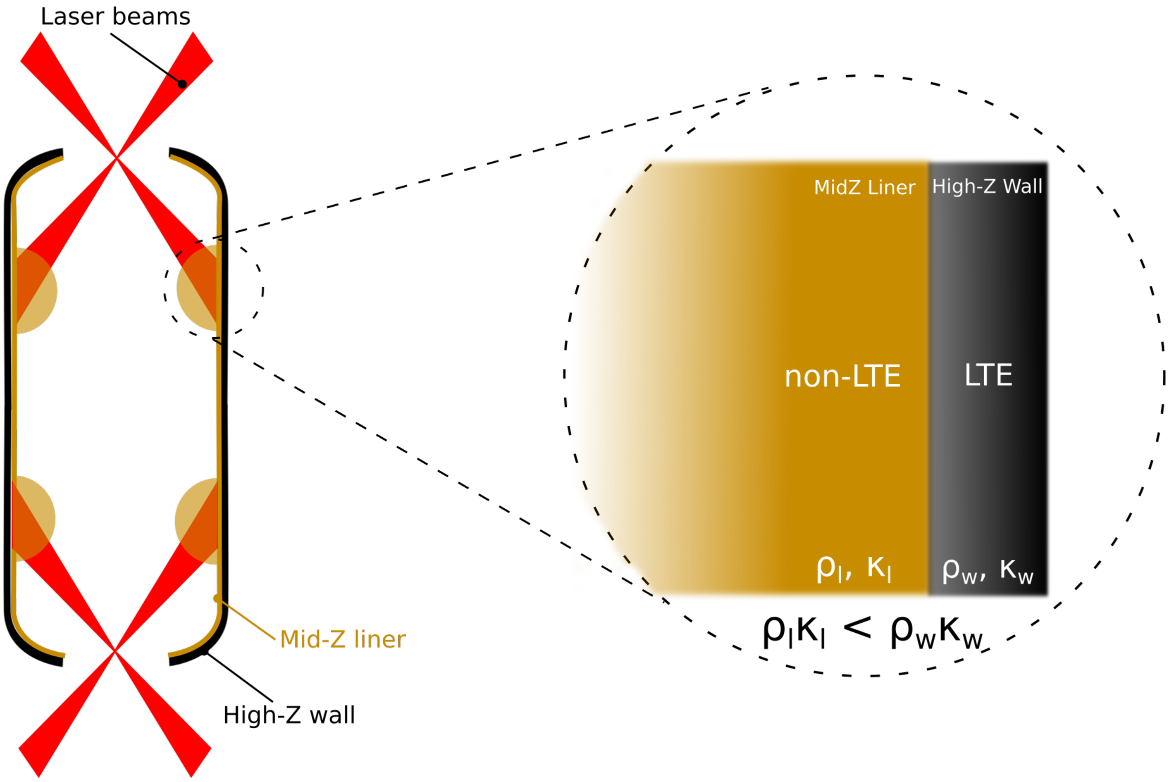

Figure 3.2: Diagram showing a high-Z hohlraum lined with a mid-Z material irradiated by lasers. The zoomed section (right) shows a cross section of the hohlraum wall where the laser is incident. ρ and κ are the mass density and radiation absorption cooefficient of the plasma respectively. Due to the lower Z number and density of the mid-Z liner the assumption of LTE is not as appropriate as it is in the case of the high-Z, high density wall.

becomes more prominent. Laser plasma instabilities can create a population of electrons with energy much greater than that of the thermal electrons. This high energy ‘bump’ on the distribution can change the electron heat transport in the laser hotspot due to their high mean-free-path. The assumption then of a diffusive conduction model is invalidated as these high energy electrons will deliver their energy further from the thermal heat front resulting in a reduction in the total heat flux due to the electrons locally. In radiation hydrodynamic modelling a flux limiter [120, 121] is used in order stop the heat flux from having an unphysically large value due to the large temperature gradients present in laser plasmas. The electron flux limiter used in h2d has been set to 10% of the free-streaming flux limit q_f, where the free-streaming flux is the maximum flux that can be transported by the thermal electrons

$$q_f = \frac{3}{2} n_e K_B T_e v_e \tag{3.1}$$

where v_e is the velocity of the thermal electrons, n_e is the electron density and T_e is the thermal electron temperature.

This electron flux limiter value has been chosen so that it is inline with experimental measurements of 3%-15% [122] and has been set the same for both gold and Cu-lined gold hohlraums in order to be consistent. Higher values of the flux limiter results in more cooling of the laser hotspots due to electron heat conduction and therefore lower temperature hotspots. This in turns leads to ions with higher populations of electrons in bound states capable of radiating energy from the hotspot, causing additional cooling. In order to set the value of the flux limiter more accurately experiments or simulations measuring the non-local heat transport are required which is beyond the scope of this work.

Simulations conducted using HYADES have been validation through convergence testing of the X-ray deposition profile and net amount of X-ray energy deposited in the capsule ablator. Feathering of the mesh towards the outer radius is increased while maintaining mass matching in other regions of the capsule until both the X-ray deposition profile and the net amount of laser energy deposited individually converge. A similar procedure is undertaken in the case of the two-dimensional h2d simulations where the laser energy deposition profile converges and net amount of laser energy deposited converges. In addition, the X-ray deposition into the hohlraum wall is also monitored separately for convergence.

3.1.2 Lagrangian Re-zoning

Studying the use of a liner at these laser intensities for longer than a few nanoseconds is challenging using a Lagrangian fluid code due to deformations that occur in the computational mesh. As the laser ablates material from the hohlraum wall, a bubble of plasma expands in the negative radial direction localized where the laser impacts the hohlraum. In addition, the X-rays generated from the laser hot-spot ablate the interior of the hohlraum per unit frequencycausing it to expand also. This results in a number of regions in the hohlraum where flows converge or undergo shear motion in such a way as to render the computational mesh invalid. An invalid computational mesh means that it can no longer be used to approximate the fluid or reasonably model transport between cells. This can occur in several ways most common being what we shall call negative volume cells or distorted cells. Negative volume occurs when a cell, in h2d a quadrilateral, has the nodes which define its corners deformed in such that it's internal volume cannot be calculated. While a distorted cell can be seen as

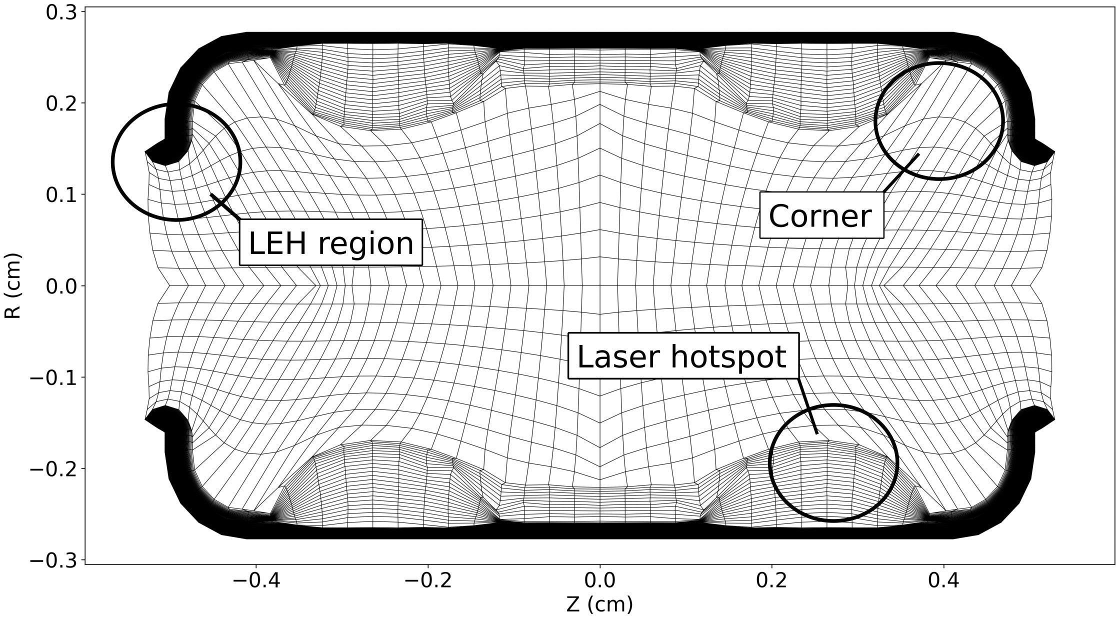

Figure 3.3: The computational mesh in the hohlraum during the 2D Lagrangian simulation with several important regions with regards to mesh rezoning procedures labelled.

occurring when the centre of mass of a cell falls outside the bounds of the quadrilateral that the cell defines. Both of the these cases occur frequently when utilising Lagrangian fluid codes to model complex hydrodynamic systems such as hohlraums and require a process of 're-zoning' the computational mesh in order for the simulation to proceed.

The process of rezoning can be undertaken in either or both of two ways; actively rezoning, prescribing a procedure that acts concurrently with the simulation; or retroactively re-zoning, waiting for a mesh failure and fixing the mesh in post-processing. Active re-zoning has the advantage of allowing, if done correctly, a simulation to continue to completion without the need for human intervention. This can be beneficial in situations where a large number of simulations is desired in order to perform a parameter sweep - for example when considering variations on hohlraum or capsule designs. It does however require some amount of prior knowledge of the simulation, specifically how the mesh tends to behave and in what areas issues are likely to occur. Actively prescribing a re-zoning operation usually will require a repeating operation to be performed on the mesh at designated time-steps and if this is done without care given to how these operations affect the physicality of the simulation it can lead to erroneous results. It is trivial to re-zone a simulation such that the mesh remains viable, it is much more difficult to re-zone while ensuring your simulation still models what was originally intended.

Retroactive re-zoning has the benefit of allowing the simulation to run unmodified until a fault occurs, one may fix this fault then by applying whatever operation is appropriate to the mesh. However, this can be time consuming and also, contrary to the fact that this is a less 'intrusive' method, may not lead to a more physical simulation compared to actively re-zoning. This is often the case since the mesh surrounding the fault is usually very deformed for a significant time before the fault occurs. This deformed mesh is many times a poor approximation to the fluid and so even a retro-actively re-zoned simulation can deviate from a physical solution over several re-zoning operations.

Rezoning operations broadly are geometric transformations performed on the mesh independent of the underlying fluid it approximates. Once the transformation is complete the old mesh is mapped onto the new mesh and the various physical quantities of the cells such as mass are re-calculated. Caution is required when performing re-zoning as many operations can result in quantities like mass not being conserved from the old to the new mesh. The extent of this loss of conservation is very dependent on both the initial mesh and the transformation being applied to it and is something that should be monitored and minimized wherever possible.

An example of a re-zoning transformation is the redistribution of mesh points via the Laplace equation

$$\nabla^2 q(x,y) = 0 \tag{3.2}$$

where $q(x,y)$ represents the position of mesh points. Given a set of boundary conditions, which in this case is a set of mesh points that define the boundary of the space being re-zoned, equation (3.2) can be solved for the new positions of points within space. This operation has the effect of smoothing areas of the mesh that may have been exposed to shear motion or extreme deformation.

The smoothing operation applied actively at various time intervals to a simulation creates a computational mesh that effectively moves independently from the fluid in certain regions of the simulation domain. This approach can only generate physical results when confined to a very small area of the mesh where physical quantities vary slowly with respect to the time interval between re-zone operations. For example in the case of the simulations of hohlraums performed here the corners of the hohlraum (see figure 3.3) are an area that is exposed to converging flows and required the careful application of this form of smoothing re-zoning.

In order to ensure re-zoning does not cause results to diverge several quantities are monitored at each stage of the rezoning process. For example, before and after each rezoning step the mass distribution between the newly rezoned cells is compared to the mass distribution before re-zoning. If the re-zoning step has caused the mass to redistribute itself such that material boundaries and density gradients have shifted significantly then that is an indicator that the problem has begun to diverge. Additionally, the total energy contained in the ions, electrons and radiation is monitored at each rezoning step. Total energy losses on the order of a few percent is observed due the rezoning operations conducted on the hohlraum. As the rezoning operations in the case of the hohlraum are confined mainly to the corners of the hohlraum in the low-density blow-off plasma they have not been found to have a large effect on the simulation even with more severe rezoning operations being applied.

3.1.3 1D vs. 2D Simulations

This work contains simulations results from both one-dimensional and two-dimensional radiation hydrodynamics codes (HYADES and h2d respectively [58]). The code h2d is an extension of HYADES into two-dimensions and with this extension comes both advantages and disadvantages.

One-dimensional simulations can be run in a far shorter time and have lower requirements on computational hardware such as RAM, number of cores and CPU speed. This is due to there being fewer variables to store and fewer equations to solve for owing to the lower dimensionality. This allows for larger regions of the parameter space of the simulation to be explored by 1D codes as hundreds of simulations can be run in a reasonable amount of time. Exploring the parameter space is also aided in one-dimensional codes by the problem setup being simpler than in higher dimensions. When defining the material boundaries and dimensions of the problem there are fewer options and therefore it is easier to quickly create new problems.

The simplicity of one-dimensional simulations is also what makes them inadequate for certain problems. Take for example, simulating a hohlraum being irradiated by lasers in order to obtain a quantity like the radiation temperature for that hohlraum. The hohlraum's radiation temperature is dependent on the power balance between the walls of the hohlraum and the laser entrance holes. In a cylindrical hohlraum the lasers are incident on a finite area of the hohlraum wall. The hohlraum walls also taper towards the laser entrance holes. Features such as these are inherently two-dimensional and so cannot be captured in one-dimensional simulations. Another important example of where one-dimensional radiation hydrodynamics simulations fall down is on predicting the experimental yields of capsules. Capsule yield is heavily dependent on the growth of hydrodynamic instabilities, a phenomenon that is not captured in one-dimension. Two-dimensional simulations can therefore provide a better understanding of the experimental yields as they can allow for the material boundaries within the capsule to be perturbed and for mixing to occur (note that mixing is not included in h2d).

The ability to capture hydrodynamic instabilities and accurately model the hohlraum both make two-dimensional simulates ideal. However, they are much more demanding on hardware and take a longer amount of time to run than one-dimensional simulations. Another major issue is the re-zoning that is required in two-dimensional Lagrangian fluid codes. This makes running batches of simulations in order to sample a region of the parameter space very difficult, as changes in the initial conditions can cause the computational mesh to behave in different ways. This difference in behaviour necessitates a different rezoning treatment, often making the process of running several hundred two-dimensional simulations very manual and inefficient.

It is for these reasons that in this work the hohlraum and capsule investigations have been treated separately. Investigating the margin for ignition requires the parameter space for the capsule and laser pulse to be sampled with a large number of simulations. It is for this reason that 1D simulations using HYADES have been conducted. For the comparison of the hohlraum physics between a lined and unlined hohlraum the two-dimensional code h2d has been utilised in order to more accurately model laser deposition and power balance in the hohlraum.

3.2 View Factor Method

View-factor codes find common application in fields where the radiation falling on a complex scene from several sources or surfaces needs to be determined. The view-factor method also finds application in architecture where calculations of the thermal radiation balance for building interiors and exteriors is conducted in order to assess building comfort and safety

[123]. Applying the view-factor method in the context of a hohlraum is useful as it allows more flexibility in terms of the problem setup and allows for a greater region of the parameter space to be explored much faster than in a radiation hydrodynamics code. Adjusting hohlraum dimensions, capsule dimensions, and the albedo profile of the wall will alter how the computational mesh behaves thus requiring additional re-zoning in a 2D radiation hydrodynamics simulation. View-factor codes are therefore useful for quickly adjusting laser, hohlraum and capsule parameters to obtain flux symmetries on the capsule.

3.2.1 Radiosity equations

The radiative flux is defined as the amount of radiative power emitted from a surface per unit area in units of W m^{-2}. Calculating the balance of radiative flux between sources and surfaces in a complex scene can be accomplished by splitting the surfaces into infinitesimal sub-surfaces of area dA_i, where i indexes over the total number of sub-surfaces in the scene N. The radiosity equation below can be used to calculate the radiation being emitted by these sub-surfaces given a certain scene geometry and initial conditions.

$$I_i = \sigma T_i^4 + \epsilon_i \sum_{j=1}^{n} F_{i,j} I_j \tag{3.3}$$

where T is the temperature of the surface i, ϵ is the albedo of the surface i, I is the radiative flux in units of W m^{-2} and $F_{i,j}$ is the view factor of surface i onto surface j. The radiosity equation (3.3) can be used to calculate the radiative flux of an elementary surface based on the temperature of the surface and the incident intensity from other emitting surfaces.

In order to solve equation (3.3) we must know the initial conditions of the system, temperatures of the bodies, initial sources of radiative flux, material properties (namely the emissivity) and the geometry of the scene. The view factor $F_{i,j}$ is defined as the fraction of the radiative flux that is emitted by sub-surface i that is incident on sub-surface j and can be written as

$$F_{ij} = \frac{\cos\theta_i \cos\theta_j}{\pi r_{ij}^2} dA_j \tag{3.4}$$

In equation (3.4) $r_{i,j}$ is the vector connecting the two centroids of the ith and jth surface. The centroid is defined here as the mid-point of the triangular subsurface. The variable θ

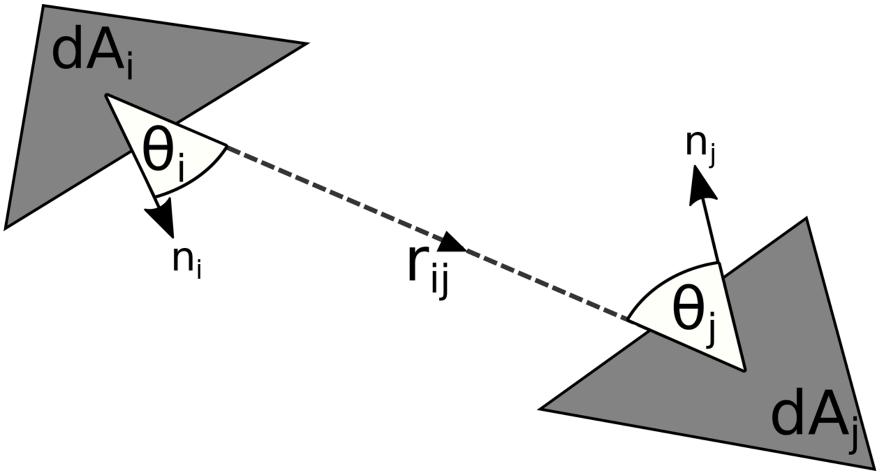

Figure 3.4: Diagram of two sub-surfaces including variables used in equation (3.4), the entire surface that the sub-surfaces approximate is excluded for clarity. Here $r_{i,j}$ is the vector connecting the two centroids of surface i and surface j, n is the normal to the sub-surface and θ is the angle between the normal and the vector $r_{i,j}$.

is the angle between the normal and the vector $r_{i,j}$. The normal, n, is defined as having a cross-product with the tangential vector at that point on the surface of zero. The quantities in equation (3.4) are visualised in figure 3.4.

Most of the computational effort will be involved in calculating the view factors between the various sub-surfaces used in the computation to approximate the real surface. The $F_{i,j}$ ends up being, for a scene subdivided into N sub-surfaces, an N×N matrix. One can already see that for complex scenes requiring many subdivisions in order to accurately represent the real objects the computational cost will increase as N^2. Re-arranging equation (3.3) it can be cast in the form

$$A_{i,j} I_i = B_i \tag{3.5}$$

where

$$A_{i,j} = \begin{pmatrix} 1 & 1-\epsilon_1 F_{1,2} I_2 & \cdots & 1-\epsilon_1 F_{1,N} I_N \\ 1-\epsilon_2 F_{2,1} I_1 & 1 & \cdots & 1-\epsilon_2 F_{2,N} I_N \\ \vdots & \vdots & \ddots & \vdots \\ 1-\epsilon_{\mathrm{N}} F_{\mathrm{N},1} I_1 & 1-\epsilon_{\mathrm{N}} F_{\mathrm{N},2} I_2 & \cdots & 1 \end{pmatrix} \tag{3.6}$$

and

$$B_i = \sigma T_i^4 \tag{3.7}$$

The matrix equation, (3.5), can be solved with the Gauss-Seidel iterative method by splitting the matrix $A_{i,j}$ into it's lower triangular and strictly upper triangular components $L_{i,j}$ and $U_{i,j}$ respectively such that.

$$A_{i,j} = L_{i,j} + U_{i.j} \tag{3.8}$$

The solution for I can be approached by the iteration

$$L_{i,j} I_i^{k+1} = B_i - U_{i,j} I_i^k \tag{3.9}$$

B_i here is a source term and has been set equal to the black-body flux emitted from a surface at temperature T but can represent any source of radiation including laser produced sources of X-rays. Including such a source term would look like this

$$B_i = \sigma T_i^4 + \eta_X I_{\mathrm{las}} \tag{3.10}$$

where η_X is the conversion efficiency of laser energy into X-rays and I_{las} is the laser intensity. Conversion efficiencies exist for hohlraum wall materials [124] but as the view-factor method omits much physics, including hydrodynamic motion of the hohlraum wall, the inclusion of a laser source term can misrepresent the complex process of laser to X-ray conversion. This will be particularly true early in the laser pulse when the heating of the wall is yet to reach a steady-state and late in the pulse when plasma filling the hohlraum will affect laser propagation. For much of the pulse the simplification of using a material specific conversion efficiency that is dependent on I_{las} but not on density, temperature, ionization and so on of the wall material is an adequate approximation for the purposes of symmetry tuning.

Further simplification of the problem is obtained by utilising the property

$$F_{i,j} A_j = F_{j,i} A_i \tag{3.11}$$

equation (3.11) shows that of the N×N surfaces only $N^2/2$ must be calculated. Further reductions can be made due to the fact that a surface's self view-factor is zero ($F_{i,i} = 0$).

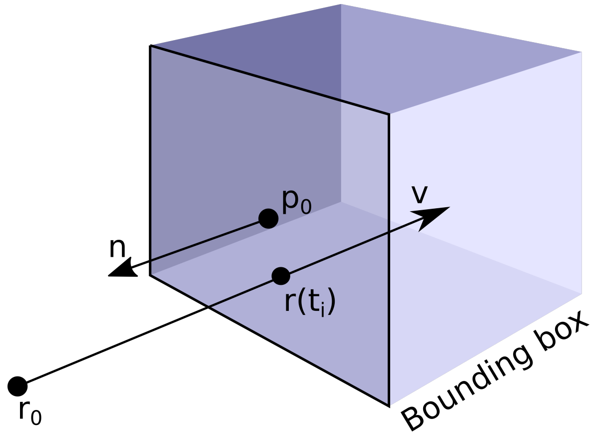

Figure 3.5: Diagram showing the geometry of a ray intersecting with a bounding box used in the view-factor simulation to calculate blocking surfaces. The ray has its origin at the position vector $\mathbf{r_0}$ and a direction vector $\mathbf{v}$. The highlighted face of the bounding box has a centroid at $\mathbf{p_0}$ and a normal vector $\mathbf{n}$. The ray intersects with the bounding box at $t = t_i$ and position $\mathbf{r}(t_i)$.

3.2.2 Intervening Surfaces

In many complex scenes, like that of an inertial confinement fusion hohlraum, there will be surfaces that block a portion of the radiation from a surface, i, to another, j. This surface, b, will either fully or partially block the radiation from i to j depending on its location and its transparency. The effects of blocking like this is important to take into account when modelling hohralums that contain capsules as the presence of the capsule, not being very transparent or reflective, effects the overall power balance in the hohlraum.

A simple method for accounting for surface blocking has been adopted here due to its ease of implementation and its computational speed-up. The method chosen is to create a 'bounding-box' around a specific subset of surfaces that encloses these surfaces. This can be done for any number of surface subsets but ideally the set of surfaces should be local in space to each other and the number of bounding-boxes should be less than the total number of surfaces used in the simulation in order for there to be any utility in using this approach. Once bounding-boxes are created and the surfaces they enclose are noted a ray-tracing calculation from the centroid of surface i to the centroid of surface j can be performed in order to see if the ray intersects with any bounding box we have defined.

The ray-tracing method solves for the intersection between a line and plane where in this case the plane is one of the faces of a bounding-box, see figure 3.5. This implementation ignores ray refraction as there are no semi-transparent volumes used that could introduce refraction into the simulation. The position of the line at a time t is defined as

$$\mathbf{r}(t) = \mathbf{r_0} + \mathbf{v}t \tag{3.12}$$

where $\mathbf{r_0}$ is the position vector for the origin of the ray and $\mathbf{v}$ is the direction of the ray. For a surface defined by a centroid position $\mathbf{p_0}$ and a normal vector $\hat{\mathbf{n}}$ the value of t for which the ray intersects is given by

$$t_i = \frac{(\mathbf{p_0} - \mathbf{r_0}) \cdot \hat{\mathbf{n}}}{\mathbf{v} \cdot \hat{\mathbf{n}}} \tag{3.13}$$

If $\mathbf{r}(t_i)$ lies within a bounding box then the calculation can be repeated over the surfaces within the bounding box until an intersection is found. This method has the advantage that an intersection check only has to be performed on the bounding boxes until an intersection is found. Then checks need only be performed on the surfaces within that bounding box rather than checking for intersections of the ray with all surfaces in the simulation. With this approach rays can be drawn for each pair of surfaces, the blocking can be calculated and the view factor array, $F_{i,j}$ can be re-defined such that it takes into account blocking

$$F_{i,j} = F^{\text{‘}}_{i,j}\Omega_{i,j} \tag{3.14}$$

where $F^{*}_{i,j}$ is the original view-factor matrix without blocking (equation (3.4)) and $\Omega_{i,j}$ is the matrix of blocking factors determined by the ray-tracing method described. The elements of Ω for our purposes are either 0 or 1, corresponding to blocked and un-blocked respectively. A more complex treatment can be applied where the degree of blocking is assessed, which would result in blocking factors between 0 and 1 depending on the fraction of radiation the intervening surface blocks. Using factors that can take values between 0 and 1 is important when surfaces are close together but what inaccuracies the binary blocking factors introduce can be compensated for with increased resolution and should not factor significantly for a hohlraum-capsule scene.

Chapter 4

Mid-Z Lined Hohlraums

4.1 Introduction

The typical hohlraums fielded on the National Ignition Facility are cylindrical and made from high-Z materials such as gold. Other high-Z materials have been proposed such as Pb which may provide a cheaper route to the mass manufacturing of hohlraums that would be required for an operating power plant [125]. It has long been the case that the majority of hohlraums have been made out of gold and uranium due to the ease of fabrication [126] and the wealth of experimental data and experience on the NIF and elsewhere [127, 128]. High-Z elements are used as the hohlraum material due to, ignoring the effect of the radiation confinement, the approximately linear relationship between proton number and X-ray conversion efficiency of the wall [129, 36]. As elements with large numbers of protons have high cross sections for free-bound and bound-bound electron transitions making them efficient converters of laser energy to X-rays and also effective materials for trapping radiation inside the hohlraum due to their high X-ray opacity.

While hohlraums made from high-Z materials are effective at producing the high radiation temperature X-ray environments (280 - 300 eV) required for ignition designs they involve the interaction of high intensity (10^{14}-10^{15} W/cm^{-2}) lasers with high-Z plasma. The main laser absorption process in high-Z plasma is inverse-bremsstrahlung which occurs within the holraum in ‘hot-spots’ located on the inside surface of the hohlraum wall. The plasma in the hot-spot is low density and is heated to several keV by the laser which propagates up to the critical density into the wall. Due to the high temperatures in these hotspots M-band transitions (n=4→3) are readily excited producing X-rays which, in addition to those

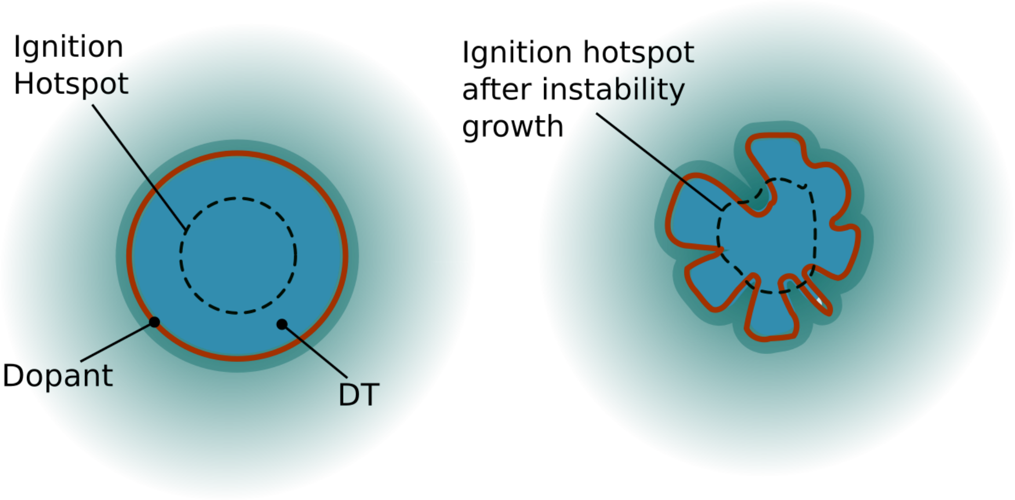

Figure 4.1: The ignition hotspot forms in the capsule during the deceleration stage of the implosion. (Left) Diagram of an ignition hotspot that forms within the capsule absent of the growth of hydrodynamic instabilities. (Right) Ignition hotspot after hydrodynamic instabilities have grown causing the mixing of dopant with the fuel within the hotspot.

produced from the ≈ 300 eV thermal component, increases the amount of energy contained in X-rays with energy greater than 1.8 keV [82]. These high energy X-rays ($hv > 1.8$ keV) have been found to have serious negative effects on capsule implosion performance. High energy X-rays can penetrate further into the ablator than the soft X-ray ablation front causing preheating which raises the internal pressure of the fuel reducing the compressibility of the capsule. Preheat also causes the inner layer of the ablator to expand resulting in an increase in the Atwood number at the fuel-ablator interface [130, 63]. This larger Atwood number results in an increase in Rayleigh-Taylor instability growth and more fuel-ablator mixing which reduces the capsule yield by cooling, deforming and introducing high-Z ablator dopants into the DT fuel, figure 4.1. In addition, due to the localised nature of the hard X-ray laser hot-spot emission the radiation flux symmetry on the capsule is reduced which causes the implosion shape to deviate from spherical and thus reduces the compression and yield [131].

The effect of the M-band radiation on the capsule cannot easily be overcome by making the capsule ablator thicker for a number of reasons. Firstly, a thicker ablator means a greater mass to accelerate, thus requiring more energy. A thicker ablator also implies a larger capsule outer radius, which can increase the amount of energy absorbed by the capsule. However, if taken to an extreme degree the increase in the ratio of the capsule radius to the hohlraum radius will result in a less symmetric implosion.

To prevent preheating of the ice layer by the hohlraum X-rays the ablator is doped with mid-Z number elements [132]. Dopants have also been shown to improve capsule implosion symmetry by smoothing the asymmetry of the X-rays generated by the high M-band laser hotspots [133]. Dopants however introduce other complications and there may be reason to reduce the levels of dopant within the ablator. For example, fuel-ablator mixing now introduces mid-Z material into the hotspot causing greater energy loss via bremsstrahlung radiation [134, 135, 136]. In an un-doped or reduced dopant capsule of equivalent hydrodynamic stability the amount of mixing of the mid-Z dopant into the hotspot would reduce with the reduction in dopant concentration. On the other hand, if the removal of dopant increases the capsule's susceptibility to hydrodynamic instabilities such as the Rayleigh-Taylor instability then the benefit gained from the reduction in dosage of impurities introduced into the hotspot will be offset by the greater amount of mixing occurring due to instabilities. It is also important to note that fuel-ablator mixing is not the only detrimental consequence of the turbulent mixing introduced by hydrodynamic instabilities. The growth of low wavenumber modes ($k = 2\pi/\lambda$) due to hydrodynamic instabilities along with the deviations from sphericity caused by an asymmetric X-ray drive can result in a deformed hotspot [137]. The deformed hotspot has an increased surface area, the optimal surface area being that of a sphere. An increased surface area leads to greater losses due to transport of energy out of the surface, the main mechanism being electron heat conduction. A deformed hotspot also results in a lower conversion efficiency of the ablator kinetic energy into hotspot internal energy upon stagnation. This is necessary to keep in mind as this is not a problem solved by the removal of dopants. In fact the removal of dopants from the ablator will result in a decrease in the radiation confinement within the hotspot. However, the trapping of radiation within the hotspot in central hotspot ignition is not a major concern as it is in ignitions schemes such as volume ignition [138].

There may potentially be another benefit to removing dopants from the ablator and that is the reduction in the number of interfaces within the capsule and the reduced chance for irregularities in target fabrication. Several layers of differing dopant concentrations are required to optimise the capsule density during the pulse. Any non-uniformity in dopant distribution, be it in the radial or azimuthal direction, will result in variations in the Atwood

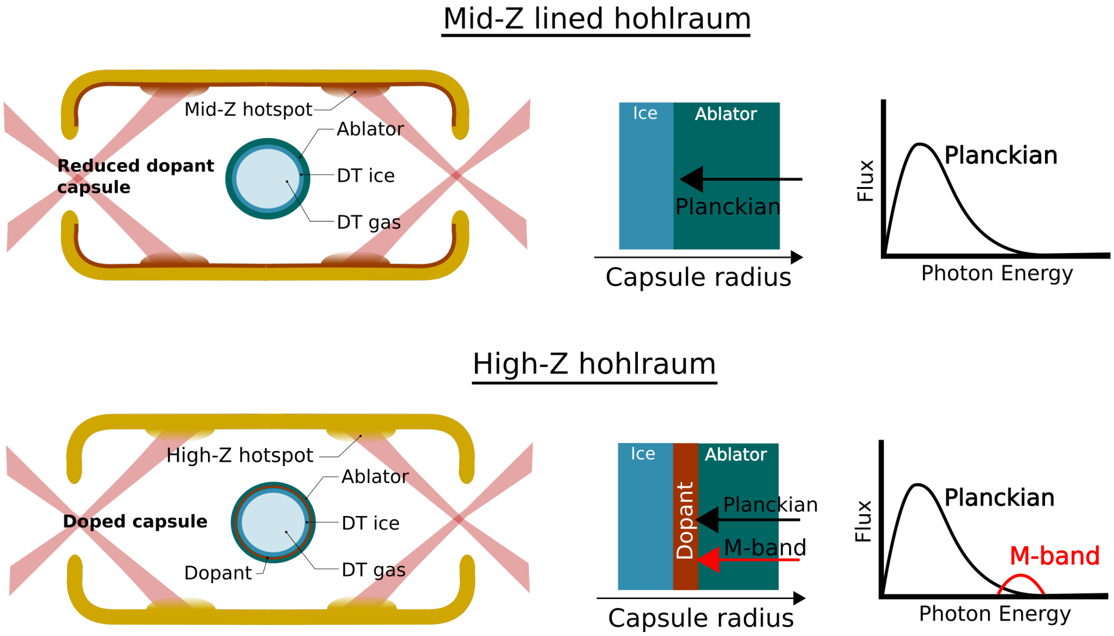

Figure 4.2: Diagram of lined and unlined hohlraums with the corresponding undoped and doped capsule. A 1D slice of the capsule structure with the penetration of the Planckian and M-band components of the X-ray drive included as arrows. The approximate shapes of the drives expected from each hohlraum is also included with the separate drive components labelled.

number and of the ablation rate of the capsule which could contribute to asymmetry in the implosion. The presence of interfaces also increases the chances of seeding instabilities due to surface roughness.

Mid-Z wall liners have been proposed as a means of reducing the fraction of X-rays above 1.8 keV and therefore facilitate the removal of dopants from the capsule ablator [139]. Hohlraums lined with mid-Z elements have also briefly been investigated on the NIF and found to perform promisingly, being capable of reducing the hard X-ray content by a factor of 2 [105]. In addition, metal foams have been investigated [140] and shown to reduce the hard X-ray fraction by a factor of 3 [141]

Lining a hohlraum with a mid-Z element aims to alter the laser deposition and conversion process so that the X-ray spectrum produced has a lower fluence of X-rays with energy greater than 1.8 keV while maintaining an overall X-ray fluence sufficient to drive capsules similar to those used in unlined hohlraums. Altering the spectral properties of the hohlraum drive in this way may allow for capsule designs with increased hydrodynamic stability and an experimental yield more inline with the predicted 1D yield from simulations. This is because the 2D and 3D effects which contribute to degraded performance, such as dopant mixing and drive asymmetry, may be mitigated by the inclusion of a liner.

This work builds upon the work mentioned previously on mid-Z hohlraum liners [139]. by performing 2D radiation hydrodynamics simulations of lined hohlraums and comparing them to an equivalent un-lined hohlraum. Particularly, the time dependent features of such a liner are investigated and how this impacts upon their application to inertial fusion hohlraums. In addition, the effect on the flux symmetry is commented upon and how the issue of excess hohlraum fill may be addressed. The description of the time-dependent processes occurring in the liner is relevant for assessing their application to hohlraums driven by longer pulse lengths.

4.1.1 Conversion process in a lined hohlraum

Laser deposition occurs when the separate beams enter through the laser entrance holes (LEHs) and are incident on the inside of the hohlraum. Due to the intensities found in inertial confinement fusion laser pulses ($> 10^{14}$ W cm^{-2}) the material on the inside of the hohlraum rapidly becomes a plasma as it is heated to several keV. Laser energy is deposited in the hohlraum primarily through the process of inverse bremsstrahlung whereby electrons that quiver in the oscillating field of the laser undergo collisions with ions which transfers energy from the laser field into the plasma [142, 143].

Laser light can travel up to the critical density in a plasma, n_c, which is defined as

$$n_c = 4\pi^2 \frac{\epsilon_0 m_e c^2}{\lambda^2 e^2} \tag{4.1}$$

Where λ is the wavelength of the laser light, m_e is the electron mass, e is the electron charge, c is the speed of light and ϵ_0 the permittivity of free space. Laser photons are absorbed by the atoms in a thin layer of the hohlraum wall via two-photon absorption transitions which increase the population of free electrons at the hohlraum wall surface. These free electrons then oscillate in the electric field of the laser gaining energy via inverse-bremsstrahlung and going on to create more free electrons through free-electron ionization collisions with ions [144]. This hot ionized plasma then expands from the hohlraum wall resulting in a low density region at the surface of the wall known as the ‘laser hotspot’ which is heated by the laser and inflates into the hohlraum cavity [145]. Ions in the laser hotspot radiate energy in the form of X-rays which then propagate both into the hohlraum cavity and back towards

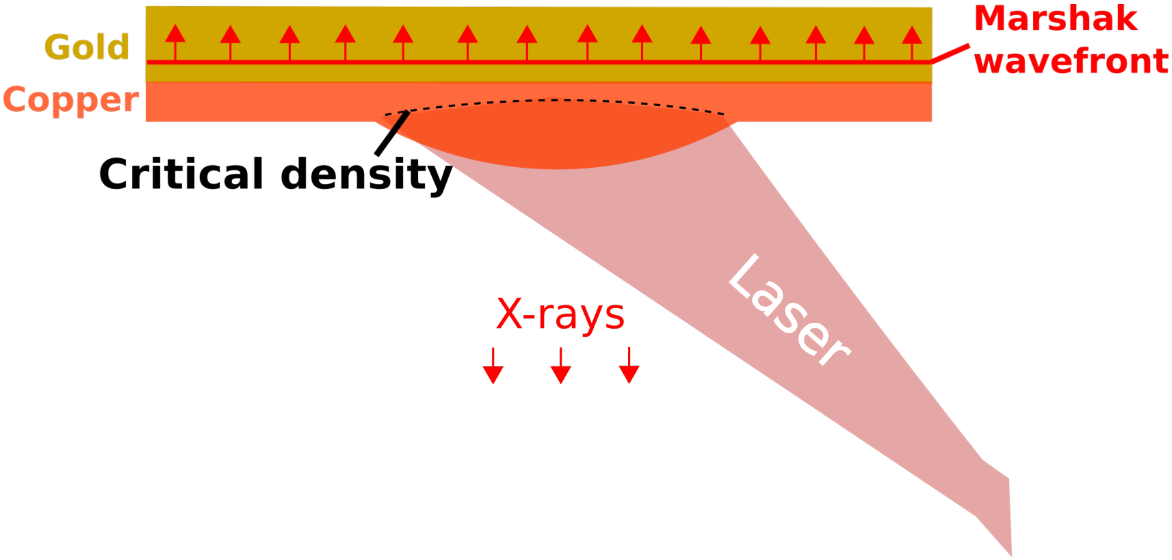

Figure 4.3: Diagram showing the hohlraum wall and laser hotspot at a time when the laser critical density sits within the mid-Z liner and the Marshak wavefront sits in the high-Z hohlraum wall.

the wall to be absorbed and heat the wall. X-rays are attenuated less than the laser photons and so are stopped in higher density plasma than the laser photons which are typically of 0.3 μm wavelength in inertial fusion pulses. The X-rays are not stopped in the laser hotspot and continue to travel into the high-Z hohlraum wall in the form of a diffusive heat wave known as a Marshak wave [98] where they are re-emitted into the hohlraum cavity.

The process of absorption and conversion into X-rays outlined here can be examined further by splitting the hohlraum wall into three distinct regions, the conversion region, the re-emission region and the cold wall. The conversion region is the laser hotspot, the re-emission region is the high opacity region where the Marshak wave propagates and the cold wall is the high density shocked material ahead of the Marshak wave. This model is studied in greater detail by Sigel *et al* in [146] and [147].

High-Z elements are selected for the hohlraum wall for two main reasons, the first being that the high number of atomic transitions available in high-Z elements makes them excellent radiators which is an important property if high radiation temperatures need to be produced. The second reason is that the wall should be able to absorb and re-emit the X-rays efficiently and this amounts to producing a slow-moving Marshak wave. A Marshak wave is formed when radiation is incident upon an optically thick medium such that as it diffuses through it via photon emission and re-emission both the medium and the radiation field are in thermal equillibrium. The speed of the Marshak wavefront is inversely proportional to the opacity of the material it is travelling in so high-Z elements are an ideal choice in this regard also. It is for this reason that mid-Z elements are investigated as liners and not as the sole wall material. The lower opacity to the X-rays coupled with the lower conversion efficiency of laser energy into X-rays of a mid-Z wall would result in much lower radiation temperatures.

The issue of the M-band and its effect on capsule design and performance has been an area that has seen much attention and solutions have been proposed and fielded on the NIF. A 'cocktail' hohlraum is made from a mixture of elements with the goal of increasing the opacity of the hohlraum wall to the X-rays and therefore reducing the overall energy loss into the wall due to the heating and thermal expansion due to the Marshak wave. This is done by using elements with complementary opacity profiles such that gaps in the absorption of each individual element overlap to provide an overall higher opacity. A wall consisting of 20% Au, 20% Dy and 60% U by atomic percentage has been shown to reduce energy losses by 17% over a pure gold wall leading to a reduction in the required laser energy [148]. These hohlraums have been found experimentally on the NIF to improve the drive power by the equivalent of 25 TW of incident laser energy [149]. The inclusion of uranium also has the effect of shifting the energy required to excite the M-band transitions to a higher energy and therefore reduce the fraction of hard X-rays [126, 150]. This has resulted in a 40% reduction in hard X-rays with subsequent increases in capsule ρR, implosion velocity and neutron yield on depleted-uranium (DU) gold hohlraums such that they now represent a large amount of high performance implosion experiments on the NIF [151].

However, the use of DU in hohlraums has obvious negative consequences when projecting the design for use in a future power plant. If we assume that energy demand and economic requirements mean that a GW scale fusion power plant is required and that the energy per shot is somewhere in the tens of MJ then the repetition rate required in order to achieve this is in the 10 Hz range. DU shots on the NIF have typically used a 7 μm layer of uranium which at the hohlraum scales currently used (length $\approx$ 1 cm, diameter $\approx$ 0.5 cm) and the required repetition rate amounts to over 7 tonnes of DU per year assuming non is recycled. DU itself is not highly radioactive or fissile and it is widely used in civilian constructions due to it's high density. However, when exposed to MeV neutrons it can undergo fast-fission into very harmful radioactive products including I-131, Cs-137, Sr-90 and Pu-239. The 14 MeV neutrons produced by the DT fusion reactions can cause this fast-fission reaction to take place within the DU hohlraum layer thereby introducing harmful nuclear waste into the system. This is in opposition to the promise of fusion energy as a clean alternative to fission or at least leads to complications for it's image and the regulatory procedures required to realise a fusion power plant.

Mid-Z liners work by replacing the element present in the conversion region with one of a lower Z and therefore effect the resultant X-ray spectrum. The re-emission region remains high opacity thus increasing the radiation temperature of the hohlraum. The $n=4\rightarrow3$ atomic transitions responsible for the population of high energy X-rays when using a high-Z conversion region are not present with a mid-Z conversion region. L-shell emission with energy below 1.8 keV dominates at the temperatures found in the laser hotspot and the resulting spectrum is predicted to be softer - fewer X-rays with energy greater than 1.8 keV - than that produced by an un-lined hohlraum.

It is important to assess the performance of the hohlraum and caspule together as part of an integrated system due to the complex nature of the physics evolving in the hohlraum. The relative performance of a reduced dopant-capsule when driven by a mid-Z lined hohlraum relative to a doped capsule driven by a conventional gold hohlraum is an important metric to assess. However, this study shall focus on the performance of the hohlraum and the quality of the spectrum produced as many useful capsule independent conclusions can be drawn from this alone. Later work shall address concerns of capsule performance when exposed to different hohlraum drives in order to understand the total energy balance of the system. This being said, due to the comments made earlier on the potential radioactive products produced by fast-fission of DU, a mid-Z lined hohlraum that performs near the levels of a DU-gold cocktail hohlraum in terms of M-band reduction would be preferable at least in terms of looking at a future reactor design.

There are additional considerations when comparing drives from lined and un-lined hohlraums that should be commented on. Comparing total X-ray energy contained in the drive is somewhat capsule dependent as the amount of that X-ray energy absorbed will be determined by the capsule opacity to the drive. For this reason comparing the energy contained in the X-rays with energy < 1.8 keV would be more useful for determining the laser-hohlraum coupling to 'useful' X-rays. While an un-lined gold hohlraum may be found to have a higher overall X-ray energy than a lined gold hohlraum there may be a greater proportion of energy contained in X-rays with energy > 1.8 keV. These X-rays contribute to preheat and asymmetry and therefore are not completely indicative of the performance of the hohlraum. The removal of dopants in the ablator may also increase the drive pressure by reducing the albedo of the capsule and therefore lowering the amount of energy radiated by the ablator.

Here the performance a mid-Z lined hohlraum is investigated in order to determine whether radiation temperatures comparable to an un-lined gold hohlraum can be achieved and to what extent the hard X-ray spectral content is reduced by lining the hohlraum. Copper was chosen as the liner element over an element such as silver (Z=47) due to its lack of n=4→3 transitions. Copper has one electron occupying the n=4 level ([Ar] 3d10 4s1) vs silver which has the following electron configuration [Kr] 4d10 5s1. This work is performed using the radiation hydrodynamics code, h2d [58].

4.2 Problem Description

The hohlraums are cylinders based on the NIF point designs [38] with diameter of 5.57 mm and length 10.1 mm. At each end of the cylinder the hohlraum curves toward the hohlraum axis to form 2 laser entrance holes of diameter 3.37 mm. In these simulations the computational mesh curves around the laser entrance hole and mesh zones at the inner surface of the hohlraum wall face outwards towards the direction of the incoming laser. This region at the edge of the laser entrance hole is designed such that as the hohlraum wall is heated and begins to expand the mesh zones are aligned such that they naturally expand without unwanted shear motion occuring that would deform the mesh zones. All outer mesh boundaries are set to freely expand.

As mentioned in Section 3.1.1 the details on internal energy and pressure for the materials used in these simulations, Cu, Au, He are taken from the SESAME equation of state data tables [152]. Opacities are calculated using h2d's inline non LTE average atom model.

Within the hohlraum is a He gas at 0.1 mg/cc density in order to aid laser propagation and reduce wall losses by reducing the rate at which the wall expands and fills the hohlraum. As the wall expands the space taken up by the He gas shrinks causing it to begin to flow out of each laser entrance hole. This motion of the mesh coupled with the shape of the hohlraum wall mesh at the laser entrance hole ensures the mesh is in a stable configuration throughout the simulation.

To simplify modelling the hohlraum windows are not included. These windows usually are made from a low density polymer with anti reflective coating and function to confine the gas fill. Due to the short time-scales we are looking at the lack of windows does not affect the hohlraum dynamics greatly.

The lasers beams are specified in 3D and enter through the laser entrance holes in two rings. The first ring is comprised of eight beams that impact the hohlraum at the waist (z = +/- 0.5 cm) and the other of 16 that are incident closer to the laser entrance hole (z = +/- 0.25 cm). Each beam is incident on the hohlraum wall with a spot size of approximately 350 μm. The laser has a pulse length of 1ns, a wavelength of 355 nm and rises linearly in 0.5 ns to a maximum power of 250 TW.

When solving the fluid equations using the Lagrangian method the computational mesh is pinned to the fluid such that mass in each mesh zone (defined as the area enclosed by four mesh nodes in h2d) is conserved. As a consequence, the number of mesh zones near the surface of the hohlraum where the laser is absorbed requires a greater density of mesh zones than regions far from the laser hotspot. As the hotspot is heated the zones are advected away from the site of absorption due to the fluid motion. Therefore, during the pulse the resolution at the laser hotspots decreases until we are no longer sufficiently resolving the laser deposition region. For a well characterised laser deposition region the optical depth of the laser should be resolved. To achieve this it is required in Lagrangian codes to 'feather' the computational mesh meaning the spacing between mesh nodes in a certain direction changes in a given direction. For our hohlraum the mesh spacing inside the wall decreases as the inner surface is approached (negative R direction). This results in a sub nanometre resolution at the laser hotspot which is sufficient to resolve the initial optical depth of the laser in the hohlraum wall, which is of the order of nanometres. As the thin outer layer of the wall is heated the mesh expands and the laser predominately is absorbed in under-dense plasma. Additionally, for the fluid equations to be solved accurately the mass in any two neighbouring mesh zones must not differ by more than a factor of 2. This is known as the 'mass-matching' condition and the closer the computational mesh is to all neighbouring zones containing the same mass, the fewer anomalies that are introduced - such as spurious reflections at mesh boundaries that have a large mass difference. In order to fulfil the mass-matching condition it is necessary to feather the mesh where the gold wall, copper liner and helium gas fill meet due to the differences in densities of each material.

These simulations use 150 photon groups logarithmically spaced up to a photon energy of 20 keV. This is sufficient to approximately resolve the M-band region (2 keV - 3.5 keV) as finer resolution would not increase the reliability of the results obtained as the average-atom atomic physics model used is not sufficiently complex to accurately predict the precise position of specific spectral lines in that region of the spectrum. This range of photon groups also captures the Cu K shell emission in the 8 - 9 keV range that will be stimulated in the laser hotspots, though not as strongly as the M-band in gold. Radiation-hydrodynamic codes require atomic physics models that sacrifice accuracy for speed of computation owing to the fact that the atomic physics calculations are required to be done alongside the hydrodynamic calculations. Atomic physics models that include many transitions slow down computation greatly therefore concessions must be made. For our purposes the proportion of energy greater than 1.8 keV is used as a performance metric and details of spectral features in the M-band range are not considered. Of greater interest is the difference in spectral energy distribution when switching to a lined hohlraum and the conversion efficiency.

All aspects of the hohlraum design is kept identical between the two designs used in this investigation apart from a 0.5 μm Cu layer on the inner surface of one of the hohlraums. This lined hohlraum has the same 25 μm Au wall as the unlined hohlraum and both contain a 0.1 mg/cc He gas. A 5 μm thick liner was chosen as this thickness allows the transition of the Marshak wave from the liner to the wall to be observed on the timescale of the simulation. In order to simplify the simulation design the liner is deposited over the entire inner surface of the hohlraum rather than locally on the laser hotspots.

4.3 Results

The peak radiation temperature determines the peak pressure for driving an ICF implosion which then in turn determines the peak implosion velocity of the capsule. Thus, as the energy required for ignition is proportional to $v^{-5.9}$ [100] the peak radiation temperature is an important metric to assess hohlraum performance. Designs that use CH as the ablator typically use peak radiation temperatures of approximately 300 eV. Note that arbitrarily increasing peak radiation temperature does not necessarily result in a higher implosion velocity as the Planckian spectrum has an increasingly large proportion of X-rays with energy greater than 1.8 keV as the temperature is increased. This results in the preheat and low

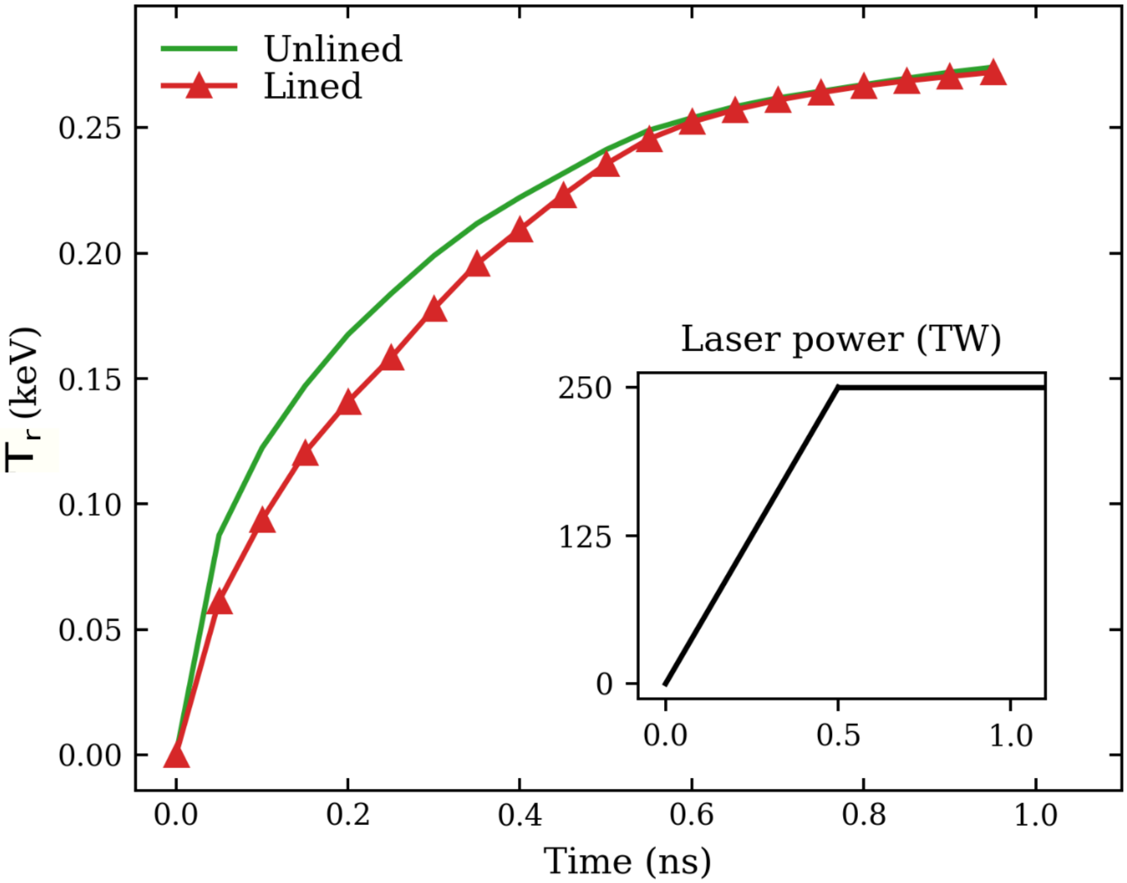

Figure 4.4: The calculated radiation temperature in both the lined and unlined holraum as a function of time with the laser pulse used to drive the hohlraum in h2d shown in the inset figure.

radiation-ablator coupling previously outlined.

The peak radiation temperatures obtained from h2d for the lined an unlined hohlraums show that lining the hohlraum with a less efficient radiator, in our case Cu, results in more hohlraum wall energy loss due to heating and hydrodynamic motion and thus a lower radiation temperature (figure 4.4) for the initial part of the pulse. This is also compounded by the lower laser energy to X-ray radiation conversion efficiency in the Cu liner which in part due to the lower Z of Cu leading to lower inverse-bremsstrahlung absorption and greater hydrodynamic losses because of the lower density of copper compared to gold. Uncertainties in the results for the radiation temperature and radiation energy are dependent on the rezoning operations performed on the mesh and have been found to be on the order of a few percent and so for the purposes of comparing the results of these simulations an error of +/- 5 eV should be applied.

However, observing the radiation temperature at late times the radiation temperature in the lined hohlraum is seen to approach that of the unlined hohlraum. Comparing the two peak radiation temperatures we see that both the lined and unlined hohlraum reach approximately 270 eV at the peak of the laser pulse. The slow increase in radiation temperature of the lined hohlraum relative to the unlined hohlraum can be explained by the gradual heating and expansion of the liner. As the mid-Z liner is heated by both the lasers and the X-rays is becomes more and more optically thin and therefore participates less in the radiation transport. This amounts to saying that the Marshak wave moves from the liner and into the higher-Z, higher opacity gold wall thus decreasing energy loss and increasing the hohlraum radiation temperature.

Looking at the radiation energy distribution within the hohlraum and how it changes with time can inform us of changing atomic physics and radiation transport processes within the hohlraum. Figure 4.5 plots the X-ray energy as a function of time, splitting the energy into that which is contained in X-rays with energy below 1.8 keV (soft X-rays) and those above (hard X-rays). The hydrodynamics of the capsule are sensitive to the balance of energy between hard and soft X-rays and the proportion of hard X-rays influences the design of ablators.

Integrating the curves in figure 4.5 gives a total hard X-ray energy for the lined hohlraum of approximately 60% that of the unlined hohlraum. This suggests that the lined hohlraum has a more favourable balance between hard and soft X-ray energies and that the liner is effective in reducing the hard X-ray content of the drive. In addition, throughout the drive the hard X-ray fraction in the lined hohlraum is lower and rises as the pulse progresses due to the increase in the high energy tail of the Planckian. This high energy tail is unavoidable and presents the risk of capsule preheat even in the absence of higher energy contributions to the Planckian distribution.

The dotted lines in figure 4.5 indicate the soft X-ray energy for both the lined and unlined hohlraums. This energy is more efficiently absorbed by the capsule and does not negatively impact the hydrodynamic performance. For unlined hohlraum doping the capsule increases the absorption of the hard X-ray energy and decreases it's negative effect on the hydrodynamic stability while introducing the negative effects mention previously. Therefore when comparing the two hohlraums in terms of their distribution of energy between hard

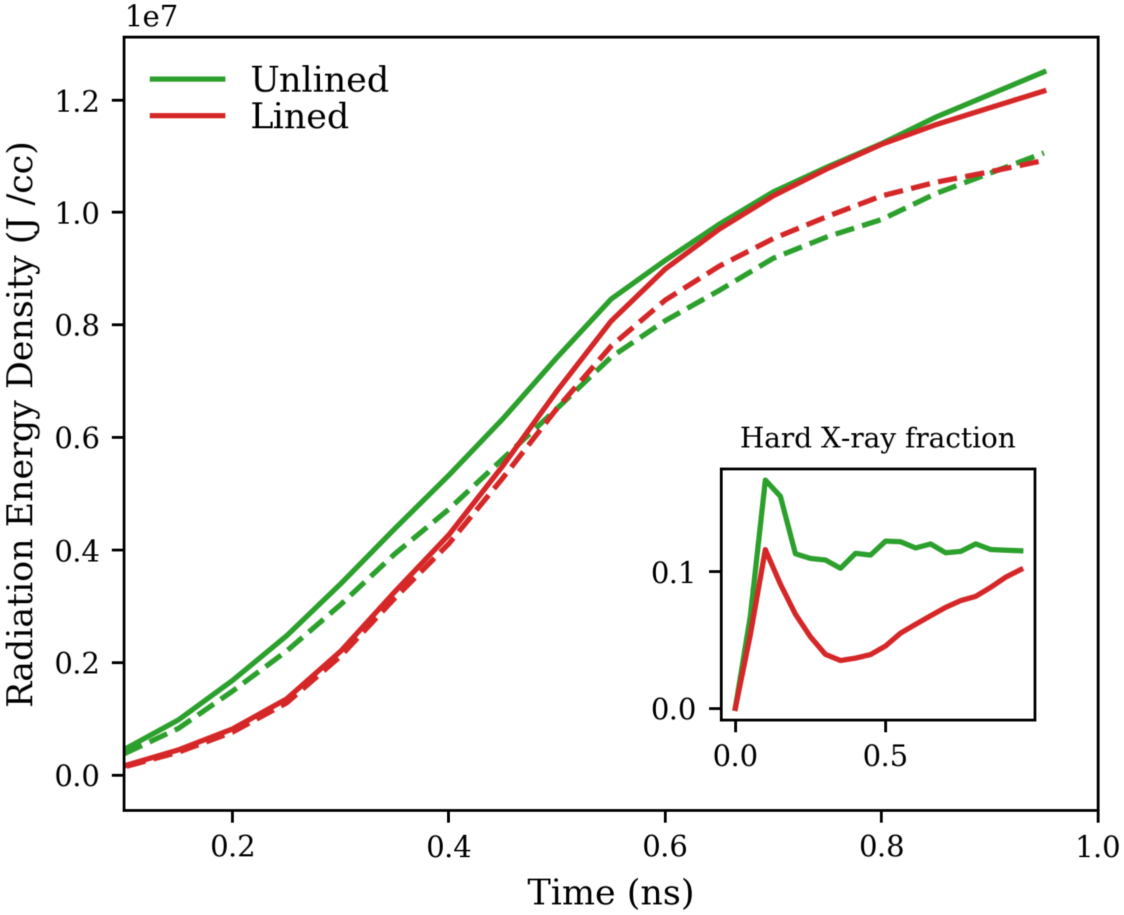

Figure 4.5: The evolution of the X-ray energy is plotted for the lined and unlined hohlraums with the total energy (across all X-ray energies) represented by the solid line and the soft X-ray energy (hv < 1.8 keV) represented by the dashed line. Also inset is the fraction of energy contained in the hard X-rays (hv > 1.8 keV) as a function of time.

and soft X-rays the soft X-ray energy is a better measure of how effective the hohlraum is in producing an efficient drive spectrum. When comparing the total soft X-ray energy it is found that the lined hohlraum has between 97% - 100% of the soft X-ray energy of the lined hohlraum accounting for uncertainty in the result due to potential rezoning effects as mentioned previously.

Full scale ignition laser pulses use a power profile with multiple steps in order to properly maintain an efficient implosion. They typically range from 10 - 20 ns in length, much longer than the pulse used here. The 1 ns pulse used here is to prove that liners can obtain radiation temperatures similar to those obtained by unlined hohlraums and that the removal of the M-band transitions works to reduce the hard X-ray content of the drive.

The time-dependence of the X-ray energy can be explained by considering the radiation transport and hydrodynamic motion occurring in the laser hotspot and in the optically thick re-emission region of the hohlraum wall. In figure 4.5 the soft X-ray energy in the lined hohlraum at 0.5 ns grows larger than that in the unlined hohlraum. The soft X-ray energy in the lined hohlraum then continues to grow while the fraction of energy in the hard X-rays remains lower than in the unlined hohlraum. We can understand this more gradual increase in X-ray energy for the lined hohlraum by looking at the positions of the Marshak wave and of the laser critical density.

Initially the Marshak wave is in the copper liner and so there is more energy lost to heating the copper than there is in the unlined hohlraum where the Marshak wave is in the gold. Line-outs taken at 1 ns show the density and electron temperature profiles along the R axis at one of the laser hotspots, figure 4.6. One can identify the high-temperature low-density conversion region where the laser propagates up to the critical density and is absorbed via inverse-bremsstrahlung. Due to a higher mass ablation rate in the copper liner versus in the gold wall the position of the critical density is further back from the original hohlraum inner surface. The relative speed of the hohlraum wall expansion can be estimated from the sound speed of each material [153]. As can be seen in figure 4.6 by comparing the position of the conversion region with the vertical line indicating the copper-gold boundary in the lined hohlraum the conversion region still lies in the copper liner after 1 ns. This is what ensures that the M-band transitions are not excited in the gold. As soon as the liner is burnt-through and the critical density lies in the gold it will get heated to several keV and M-band transitions will begin to be excited.

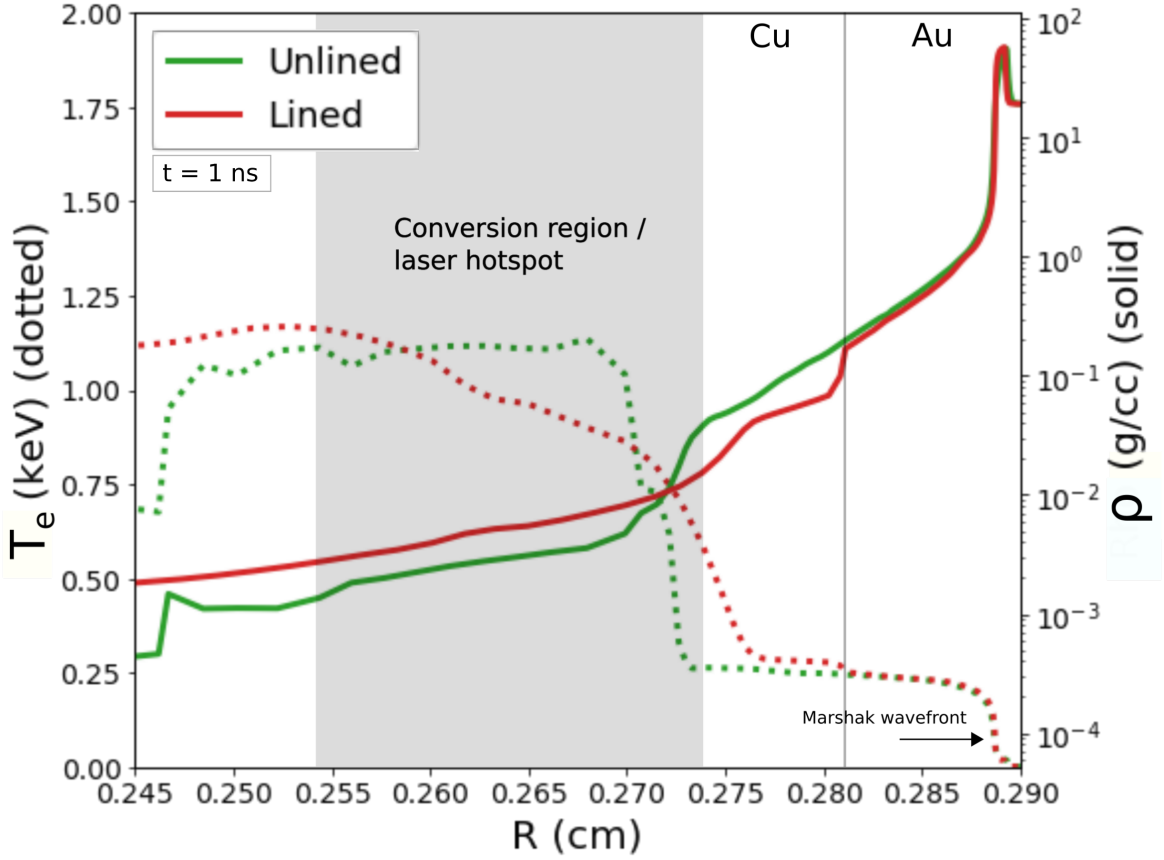

Figure 4.6: A 1D slice of the density (solid line) and the electron temperature (dotted line) in the radial direction at one of the laser hotspots. The slice is taken at a time of 1 ns through the laser pulse. The conversion region can be identified as the low-density high-temperature region in both the lined and unlined hohlraum curves indicated by the shaded region on the figure. Looking at the lined hohlraum curve the electron temperature in the copper re-emission region is slightly higher than in the unlined hohlraum gold re-emission region. This is due to less radiative cooling in the copper layer.

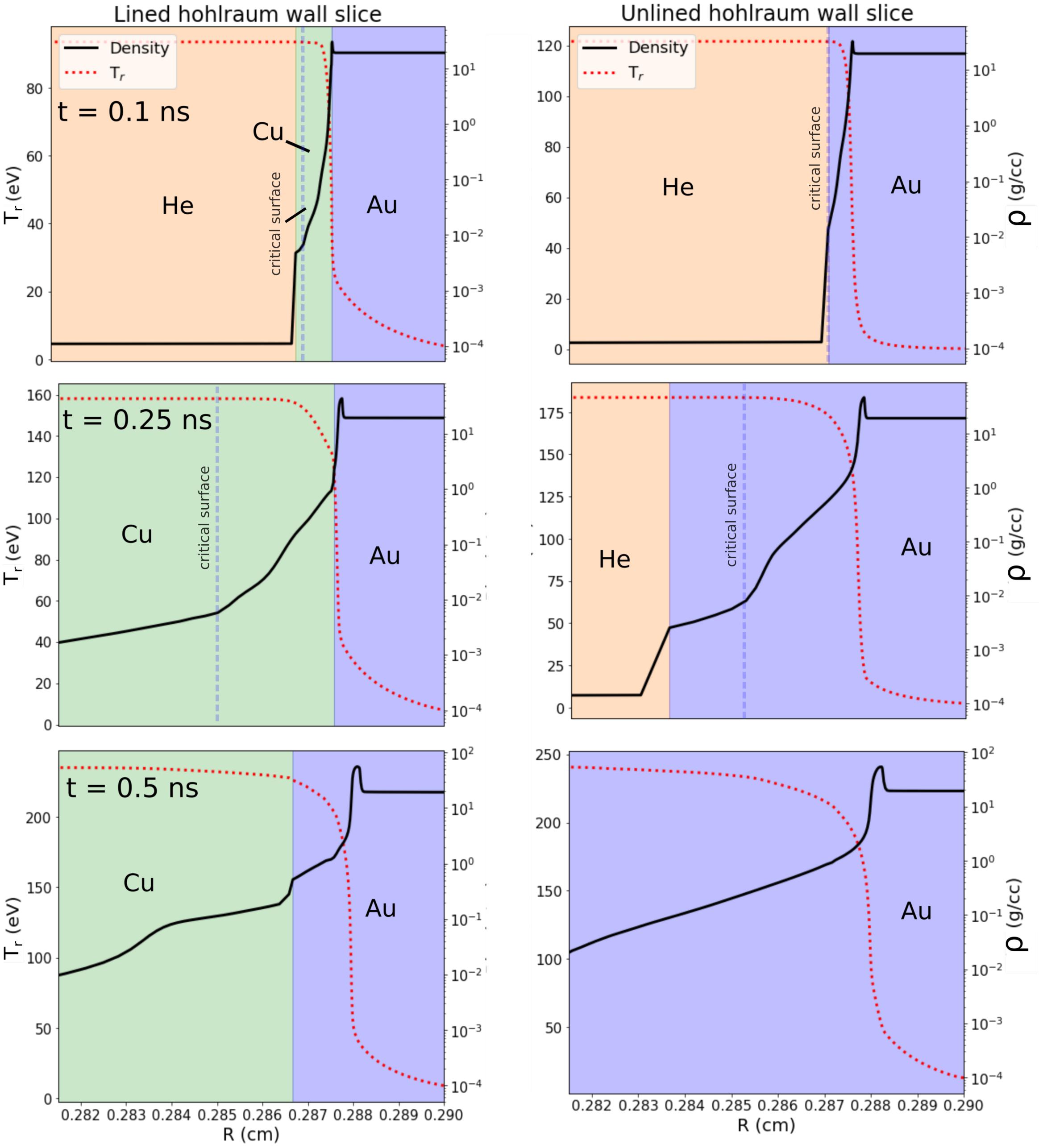

Figure 4.7: 1D slices through the hohlraum wall for lined (left) and unlined (right) hohlraums. Slices are taken in the radial direction at several times throughout the laser pulse. Material regions are coloured and labelled in order to show the position of the Marshak wave, indicated by the red radiation temperature curve, and critical surface (blue dotted line) at various times. Mass density is also plotted so that the three density regions (conversion, re-emission, cold wall) can be observed. One can see that in the lined hohlraum at 0.1 ns and 0.25 ns the Marshak wave sits in the liner material while at 0.5 ns the Marshak wave front has moved into the gold wall.

We can also notice that in figure 4.6 the Marshak wave has propagated into the gold in the lined hohlraum, which can be seen by the approximately 300 eV electron temperature feature ending at the high density shocked wall. The less time the Marshak wave spends in the copper liner the less energy loss and the sooner the rise in radiation temperature can occur.

Observing the Marshak wave position at various times during the laser pulse for lined and unlined hohlraums, figure 4.7, and comparing this to how the X-ray energy content changes with time, figure 4.5, we can see that what material the Marshak wavefront sits in effects the X-ray energy at that time. Before approximately 0.5 ns have passed the X-ray energy in the lined hohlraum is below that of the unlined hohlraum. We can see that in figure 4.7 this corresponds to times when the Marshak wave sits in the copper layer. The X-ray energy in the lined hohlraum rises to meet that contained within the unlined hohlraum at a around 0.5 ns. Again, looking at the 1D slices in figure 4.7 this corresponds to the time when the Marshak wave entered the gold layer.

The difference in expansion rates of the laser hotspot between lined and unlined hohlraums can be estimated from the ratio of the atomic masses of the copper vs gold [153]. The higher expansion rate for the copper liner can also be seen in figures 4.6 and 4.8 where both the plasma ablated from the hohlraum wall and the laser hotspot bubbles have travelled further into the hohlraum for the lined hohlraum. For a laser pulse on the order of tens of nanoseconds the plasma will have had more time to travel further into the hohlraum volume potentially impeding laser propagation. This is already an issue in unlined hohlraums as late into the pulse the high-Z laser hotspot material moves into the path of the inner beam in NIF experiments and reduces the drive at the waist of the hohlraum. Due to the greater rate of expansion of the copper liner the hohlraum will fill with mid-Z material faster than in the unlined case thus potentially impeding the laser beam propagation earlier into the pulse. This would result in a loss of symmetry sooner into the pulse but could be mitigated by changing the hohlraum shape to allow for more space for hotspot expansion [52] or by balancing power to the inner and outer cones in a time dependent way in order to maintain a symmetrical implosion [154]. It is also important to note that the lower Z of the copper that would be present in the hohlraum volume in a lined hohlraum will result in less inverse-bremsstrahlung absorption of the lasers relative to the gold that would otherwise fill the hohlraum in an unlined hohlraum.

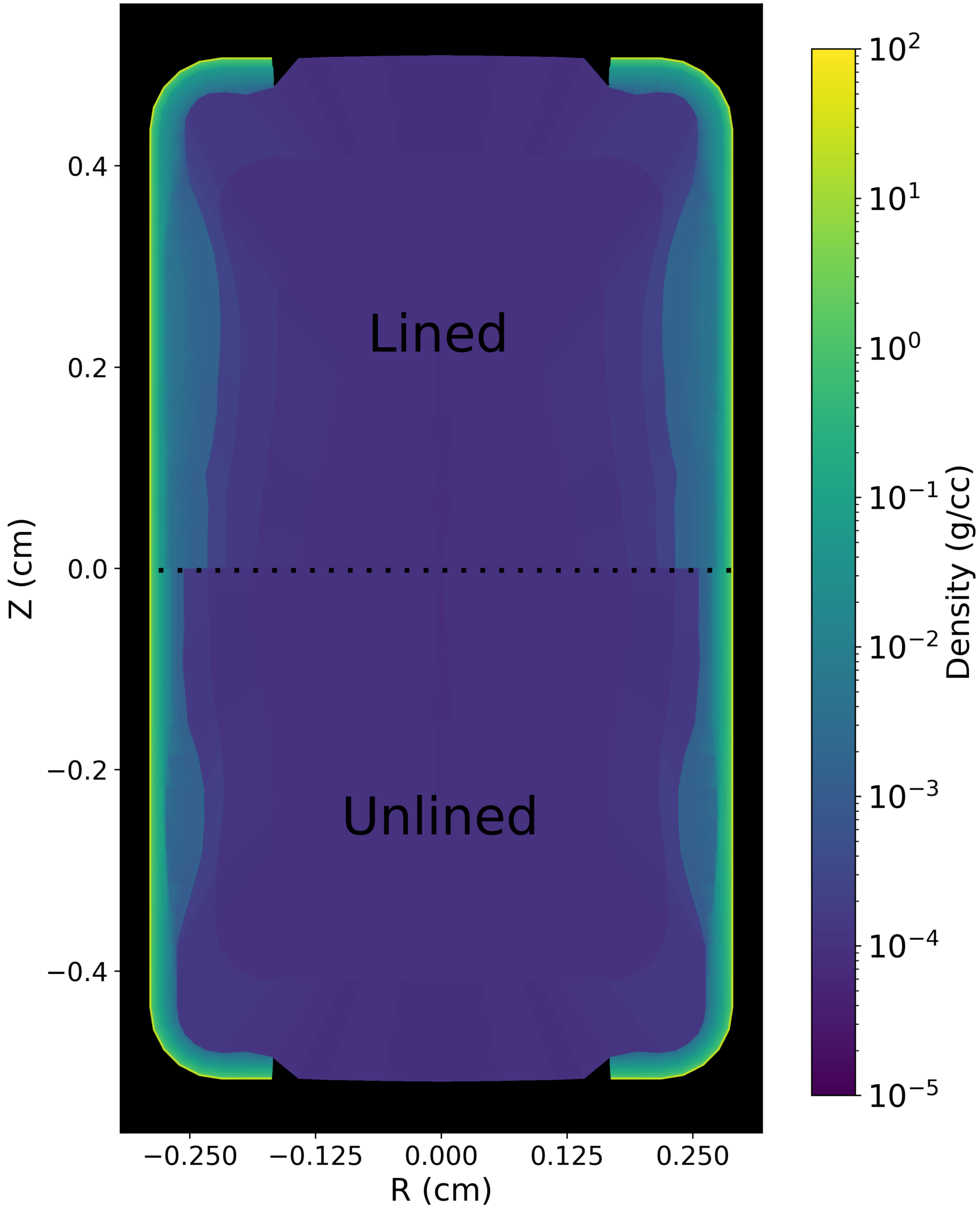

Figure 4.8: 2D plot of the density for a lined (top) and unlined (bottom) hohlraum at a time of 1 ns. The lower mass of the liner results in a greater displacement from the initial position of the hohlraum wall for the lined hohlraum than present in the unlined hohlraum.

As previously mentioned the time taken for the laser critical density to move into the gold wall in a lined hohlraum determines the length of time for which the M-band transitions are suppressed. This depends on the thickness of the liner as a thicker liner for a given mass ablation rate and mass density will take longer to burn through. For M-band suppression to occur for a given length of time, τ, the thickness of the liner, d_l, should be

$$\rho_l d_l \geq \int_0^\tau \dot{m}_a dt \tag{4.2}$$

The mass ablation rate in equation (4.2), $\dot{m}_a$, is dependent on the laser power and so for a pulse designed to implode a capsule will change throughout the implosion hence the need to integrate over time. In equation (4.2) ρ_l is the density of the liner. Using a higher density liner material that still is capable of eliminating M-band radiation would result in a thinner liner being able to be used. This would not improve the performance of the liner however as the speed of the Marshak wave is inversely proportional to the opacity [98] of the material and increasing the density would likewise increase the opacity and slow down the Marshak wave.

For the lined hohlraum to obtain improved performance over a hohlraum made solely of the liner material (for example a copper hohlraum) the time taken for the Marshak wave to traverse the liner and enter the high-Z, high-opacity gold wall should be much less than the pulse length of the laser. This can be expressed as

$$\frac{d_l}{v_M} << \tau \tag{4.3}$$

where v_M is the Marshak wave velocity and τ is the laser pulse length. The ratio of the liner thickness and the Marshak wave speed will determine the rise time of the radiation temperature in a lined hohlraum relative to an unlined hohlraum.

Increasing the thickness of the Cu liner relative to the high-Z wall ad infinitum is equivalent to fielding a pure Cu hohlraum. The Marshak wave would never transit into the high-Z wall and so the losses incurred from the heating and hydrodynamic expansion of the Cu would be large. It has been found that for pure Cu hohlraum, while displaying the same ability produce X-ray drives with a lower component with energy greater than 1.8 keV, they fail to reach the radiation temperatures of lined hohlraums.

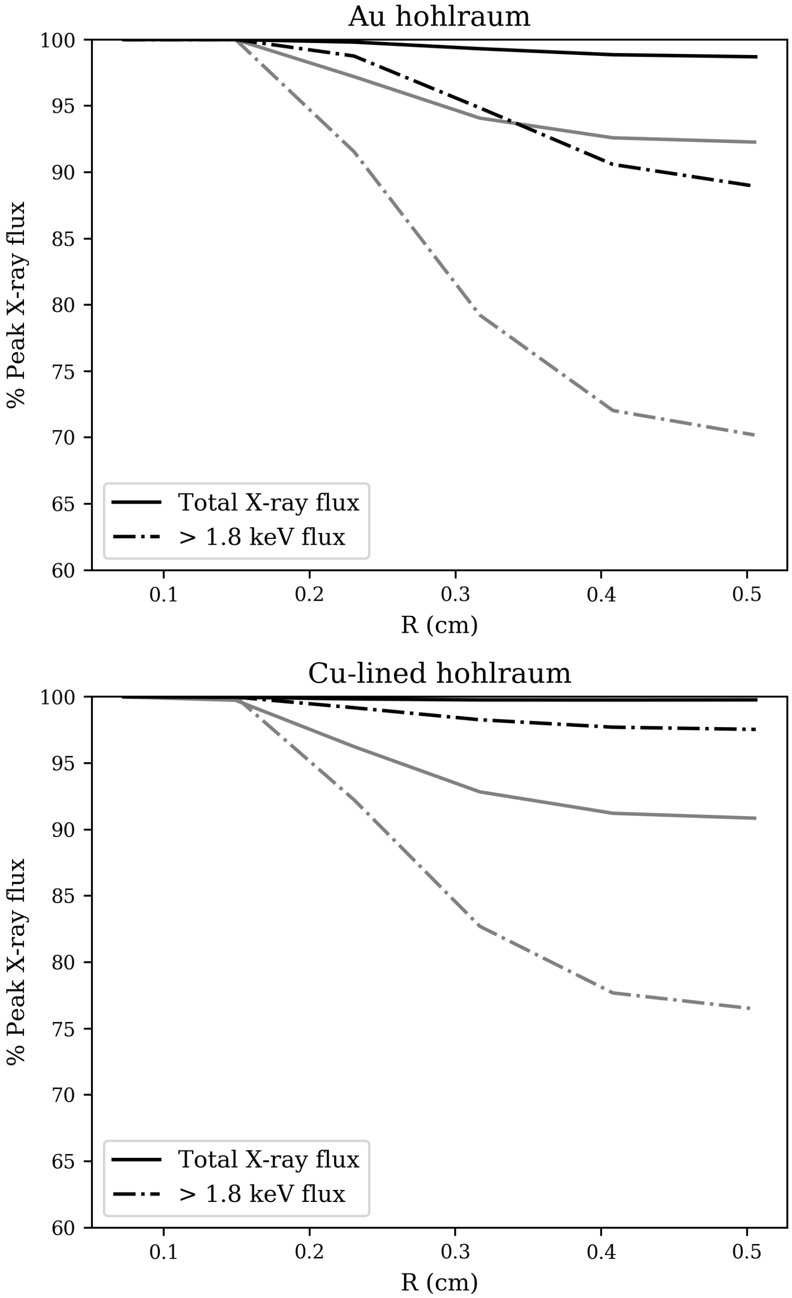

Figure 4.9: Plots of the X-ray flux at the hohlraum axis for the total X-ray flux (solid line) and the > 1.8 keV X-ray flux (dashed line), each normalized respectively. The flux profiles at two times are given: (grey) 0.25 ns, before the marshak wave enters the gold; (black) 0.5 ns, after the Marshak wave has crossed into the gold.

We can also look at the two-dimensional data from h2d in order to better understand how the plasma in the hohlraum evolves over time. This is important to model as a 1D simulation of a hohlraum cannot capture the re-emission and absorption of X-rays that take place in the hohlraum and form the hotspots and re-emission regions. It is also informative to observe the position of the laser hotspot bubbles and the degree of expansion of the hohlraum wall in order to comment on issues that may arise due to impeded laser propagation. Figure 4.8 shows a 2D density plot for the lined and unlined hohlraum at t = 1.3 ns (when the laser hotspot plasma has had time to expand into the hohlraum). The material boundaries are indicated by the black lines and show that for the lined hohlraum, as expected, the copper has travelled further into the hohlraum than the gold in the unlined hohlraum. Looking further towards the hohlraum wall it can also be noted that the gold wall in the lined hohlraum has undergone expansion but does not extend into the hohlraum where it risks impeding laser propagation. The short timescales simulated here mean that though the laser power is near the level used to create the peak radiation drive in a multi-shock structured pulse there has not been sufficient time for the wall plasma to undergo much motion towards the hohlraum axis in either the lined or unlined hohlraum. A fully integrated hohlraum-capsule simulation would have the hohlraum fill with the ablator material (commonly CH) that is ablated as the X-rays from the hohlraum illuminate the capsule. This results in converging plasma flows meeting somewhere between the hohlraum wall and the capsule. Work has been done to study these flows and their effect on laser beam propagation in modelling and experiments [107, 155]. The converging flows present with the inclusion of a capsule make inferring laser beam propagation in the lined hohlraum difficult and further work is required to correctly quantify the effect.

A mechanism that can be commented on is the laser entrance hole closure. This occurs when plasma is ablated around the laser entrance hole and expands towards the hohlraum axis resulting in the area the laser initially had to propagate through unimpeded grows smaller as the pulse evolves. For a lined hohlraum as we have already seen that rate of ablation is higher and so laser entrance hole closure would occur faster thus reducing the laser to hohlraum energy coupling. This however can be mitigated by removing the liner material that is near the laser entrance hole and therefore reducing the ablation rate in that region of the hohlraum.

Though symmetry is not the focus of the work in this chapter it is no doubt an important component of a inertial confinement fusion as it is beneficial to maintain a spherical implosion. Hohlraum already reduce high order spatial modes from the drive due to the multiple re-emission and absorption events that occur within the hohlraum. Low order modes can however still persist and produce final capsule fuel hotspot shapes that are 'pancake' or 'sausage' shaped. One source of radiation asymmetry are the laser hotspots in unlined hohlraums due to them being the source of the M-band X-rays. We can plot the radiation symmetry on the hohlraum axis to get an idea of the uniformity of the drive. Figure 4.9 shows the axis symmetry of the total X-ray energy and the hard X-ray energy for both lined and unlined hohlraums. The lined hohlraum has a lower hard X-ray fraction and so the laser hotspots have a more similar X-ray flux to other parts of the hohlraum and so the drive symmetry is increased over the unlined hohlraum. At the time when the Marshak wave has entered the gold wall in the lined hohlraum (approximately 0.5 ns) the lined hohlraum has a flux uniformity of approximately 2.5% whereas the unlined hohlraum has a flux uniformity of 10%. The degree to which this affects the drive symmetry on the capsule is dependent on several factors such as the dopant levels in the capsule and how much smoothing of the M-band X-rays this provides. Again, integrated capsule-hohlraum simulations are required in order to precisely predict the degree of symmetry improvement but some degree of symmetry increase can be reasonably inferred from these hohlraum only results as they show how removing the M-band X-rays creates a more uniform source..

4.4 Discussion

In this work 2D simulations of inertial confinement fusion hohlraums have been carried out to investigate the effect of lining the hohlraum with a mid-Z element, in this case a 0.5 μm layer of copper. The lined hohlraum has been shown to reduce the hard X-ray fraction in the hohlraum to approximately 60% of the fraction produced by an unlined gold hohlraum. The hard X-ray fraction peaks for both at 0.1 ns due to the dominance of line emission, though the total amount of X-ray energy at early times is relatively low. In the gold hohlraum the hard X-ray fraction is around 10% of the total X-ray energy for the duration of the pulse whereas in the lined hohlraum the fraction begins at 5% rising to 10% towards the end of the pulse, see Figure 4.5. This increase is consistent with the tail of the Plankian shifting to higher energies as the radiation temperature increases and the heating of the gold wall as the liner is ablated. This is beneficial to the overall performance of the inertial fusion target as it allows the dopant levels to be reduced in the capsule thus preventing the mixing and stability issues previously discussed.

When comparing the total soft X-ray energy of the two hohlraums the lined hohlraum contained, within tolerance, equal (97% - 99%) energy relative to the lined hohlraum. The decrease in the M-band component of the X-ray drive is at the expense of the energy required to heat the liner. It is required that this energy deficit be recouped in the hydrodynamic performance of the capsule. This may be through increased implosion velocity due to lowering the mass of the ablator by removing dopants. This energy may also be regained through the improved hydrodynamic stability of the capsule leading to less energy loss from the hotspot at stagnation. Importantly, any improvement that puts capsule performance closer to 1D simulated performance is of benefit. Potential reductions to two and three dimensional instabilities that could push capsules over the ignition threshold far outweigh losses in conversion efficiency even if reducing dopant levels in the capsule does not provide sufficient compensation for lining the hohlraum.

Further work is required in order to properly assess the issue of increased hohlraum fill in mid-Z lined hohlraums. Longer pulses introduce the potential for mechanisms such as laser cross-beam energy transfer [156] to introduce symmetry swings in the hohlraum drive as well as the bremsstrahlung losses caused by the copper filling the hohlraum. Hohlraum wall motion is already an issue that is being investigated and novel hohlraum designs aim to reduce the effect of this by improving the laser's path to it's intended deposition site [52, 157]. These designs may help alleviate the extra fill rate of lined hohlraums and in addition ways that liners may be selectively deposited on the hohlraum wall could reduce the fill rate issue. Liners may be deposited on laser deposition sites only or in band-like patterns to reduce the total mass of mid-Z material that is required to be heated thereby reducing the total energy loss incurred.

Chapter 5

Liner-driven Reduced M-band 1D Implosions

5.1 Introduction

One of the primary applications of hohlraums is in the generation of X-rays with sufficiently high temperature to drive the implosion of an ICF capsule. Whereas in the previous section the efficiency of a particular lined hohlraum was examined, in this section the performance of several variations on capsule designs shall be studied in order to understand the potential benefit of utilizing a drive spectrum that lacks a significant high energy component. The primary motivation for lining the hohlraum is to reduce the high energy X-ray population so as to reduce the need to include dopant in the capsule ablator. The following section aims to understand better the trade-offs between dopant concentrations when capsules are exposed to drives with varying degrees of M-band content.

The effect of varying dopant concentrations and their distribution throughout the ablator has been examined in several works by other authors [132, 158]. The simulations performed here mean to examine the effect of lowering the dopant concentration in conjunction with a Planckian X-ray spectrum in order to assess the 1D threshold for ignition and also make predictions of 2D performance by looking at the Atwood number of the fuel-ablator interface. While the benefits in terms of M-band removal and lower radioactive waste have been previously stated in Chapter 4 regarding a lined hohlraum, the relative performance of the corresponding un-doped capsule is also of interest. Firstly, as ignition of the capsule and energy gain is the goal of inertial confinement fusion the removal of the dopant should not cause the capsule to fail to ignite in 1D. Secondly, quantities that allow us to infer hydrodynamic stability in 2D such as the Atwood number and the Rayleigh-Taylor instability growth rate should be similar or improved over those of an equivalent doped capsule driven by a gold hohlraum. This work adds to the current understanding of the effect of dopant on the ignition threshold for X-ray drives with and without an m-band component. It also highlights the importance of radiative cooling by the dopant layers and how this impacts the overall power balance of the capsule. Mixing of impurities is a major concern in inertial fusion [134] and this work aims to further quantify the effect of removing dopant from the ablator in conjunction with removing the m-band component from the drive.

Capsule ignition thresholds obtained from 1D simulations are increased by 2D and 3D hydrodynamic phenomena and so when making any comparison or prediction of the performance of a design done through 1D simulations it is essential to look at the physical quantities that predict performance in higher dimensions. For this reason the 1D yields and ignition thresholds in this work give the optimal performance of un-doped capsules relative to doped capsules with no hydrodynamic mixing. Drawing conclusions on the stability of material interfaces within the capsules in 1D should provide a better understanding of performance in higher dimensions.

5.2 Simulation Description

The simulations contained within this section were carried out using the 1D radiation hydrodynamics code HYADES [58]. The capsule was created in a 1D spherical geometry with mesh resolution increasing toward the outer surface of the capsule to maintain mesh resolution of gradients within the expanding plasma as X-ray energy is deposited into the capsule. Distances between zones have been adjusted within the capsule such that the mass matching criteria for a Lagrangian mesh holds. Specifics of capsule dimensions and composition are included in the proceeding section.

The ablator mesh consists of 300 cells with the outer cells feathered such that the mesh resolution increases towards the capsule outer radius resulting in cells near the capsule outer surface of approximately 70 nm. This resolution and degree of feathering has been found to be suitable over a range of X-ray drive power and M-band X-ray fraction. This suitability is assessed over the different capsule configurations using convergence testing of the ablation density profile and laser deposition profile. All other boundaries in the capsule are mass matched in order to prevent spurious shock reflection and unphysical transport.

Equation of state tables are taken from the SESAME library [152] and the inclusion of small amounts of dopant into some of the capsule layers is assumed to have a negligible effect on the equation of state used to model the capsule ablator material. Opacity data required for the radiation transport is taken from the SESAME tables and opacity in doped regions is handled by the HYADES inline average atom atomic physics model. The radiation transport calculation is done in the diffusive approximation with 50 energy bins spaced up to 2 keV with 10 larger bins logarithmically spaced between 2 keV - 10 keV in order to resolve the M-band component of the spectrum that lies approximately between 2 keV - 3 keV. All regions of the simulation assume local thermodynamic equilibrium in order to calculate ionization states.

Upon stagnation the temperature in the core of the capsule will increase and thermonuclear reactions will begin to occur at high rates. A Maxwellian averaged cross-section is used to determine the reaction rates in HYADES. It is assumed that the reaction products transport their energy according to a multi-group diffusive energy transport equation. The multi-group structure has been set to the default in HYADES with alpha particles having 5 bins between the thermal energy of the plasma and 3.54 MeV and 8 bins between 3.54 MeV and 12.3 MeV. Nuclear reactions can occur and isotope concentrations are tracked within the capsule for nuclei up to B-11, though only light nuclei up to He-4 are included in the multi-group transport.

The simulation domain is set up with the mesh regions that denote the capsule extending from the centre of the domain to the outer radius of the capsule. The source of the pressure driving the capsule is generated by the absorption of X-rays in the capsule ablator layer. These X-rays are introduced into the simulation domain as a radiation source incident upon the outermost mesh zone.

5.2.1 Capsule Designs

The capsules used in these simulations follow similar designs as those in [38] with a CH ablator shell surrounding a cryogenic DT ice and gas centre, see figure 5.1. The CH ablator shell has doped layers at various depths and concentrations in order to mitigate X-ray preheat, figure 5.1. This gives the ablator shell a radially dependant dopant profile which increases

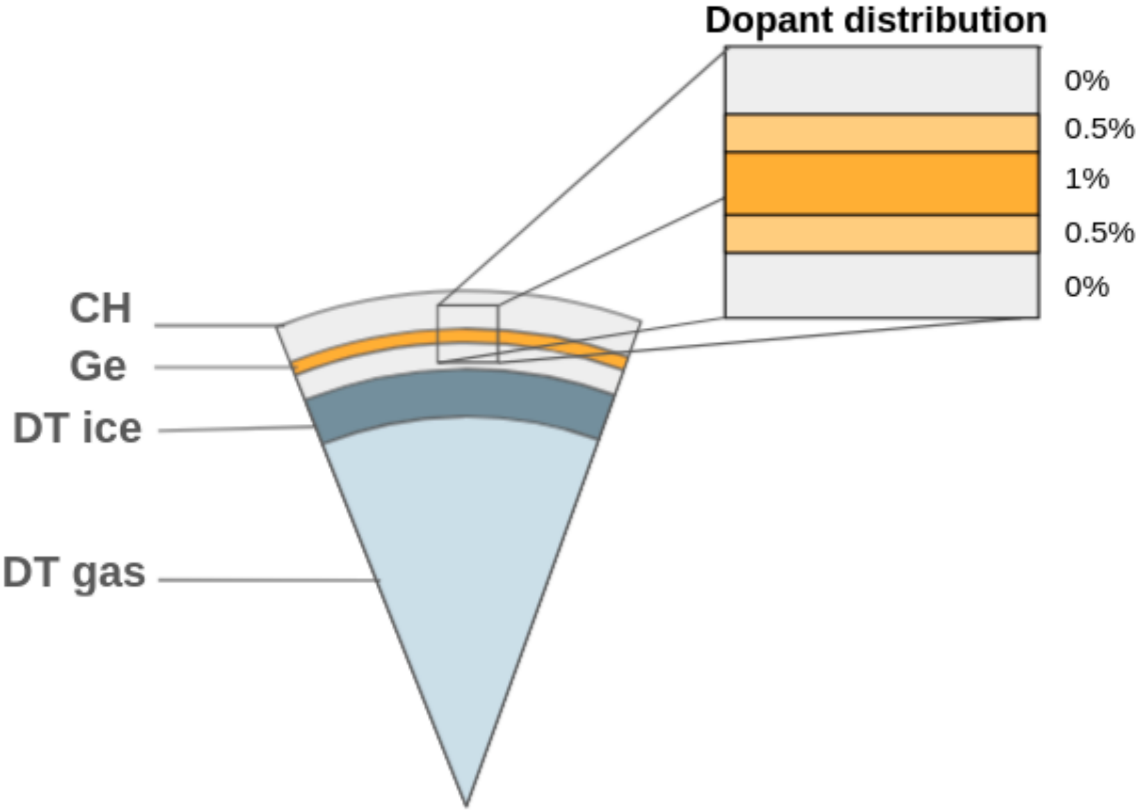

Figure 5.1: A diagram of a 2D segment of the capsule used in these simulations with the locations of the various layers indicated with different colors and the graded dopant layers inlaid.

Outer radius (μm)	Material	Density (g/cc)
850	DT	0.3×10^{-3}
918	DT	0.255
923	CH	1.069
928	CH + 0.5% Ge	1.108
962	CH + 1.0% Ge	1.147
975	CH + 0.5% Ge	1.108
1108	CH	1.069

Table 5.1: Table containing the dimensions of the capsule used in this study. The 'outer radius' indicates where the given material and density region ends and the region below begins. Capsule design taken from work published by Haan *et al* [38].

the stability of the shell by reducing the sharpness of the density jump from doped to undoped layers. Decreasing the density jump also decreases the amount of energy reflected by a passing shock during the implosion increasing energy coupling to the capsule. This design feature has been included to make the simulations more similar to capsules used at facilities such as the NIF.

Several dopant elements have been investigated by other authors such as Ge and Si in order to improve the performance of capsules with regards to reducing hard X-ray preheat. Si has replaced Ge as the ablator dopant due to its lower Z which allows more X-ray flux to reach the ablation from, thus increasing drive pressure and implosion velocity [159]. However, compared to Si, Ge has been found to prevent more preheat due to its L-shell absorption edge being at 1.3 keV vs the K-shell absorption edge of Si which sits at 1.8 keV [160]. As this work aims to quantify the effect of reducing dopant concentrations in conjunction with lowering the m-band fraction the choice of Ge as the dopant has been made. The higher opacity of Ge to the hard X-rays will aid in the interpretation of the results as preheat effects can be assumed to be low for the highly doped capsules. Using Si as the dopant would mean that some of the low dopant concentration design would ignite over a smaller range of parameters, or not at all, reducing the number of data points for the investigation.

The peak concentration of Germanium dopant in the ablator is varied between the different capsules used in this simulation from 0% to 1% where the dopant is distributed with the radial profile shown in figure 5.1.

5.2.2 Pulse Designs

The pulses used follow a 4-shock structure as shown in figure 5.2. The first shock, known as the ‘foot’ of the pulse, sets the adiabat of the capsule while the remaining pressure jumps drive subsequent shocks that are timed to keep the DT ice layer on the lowest possible adiabat. As features of the capsule are altered the pulse must also be altered in order to ensure that no shock mistiming occurs. As the dopant concentration in the capsule is changed small tweaks to the pulse should be sufficient to ensure that no capsule is failing to ignite due to entropy added by shock mistiming. Changes to the energy distribution of the X-rays will also require that the pulse timing is changed to reflect whatever changes to shock velocity may occur as a result. Changes in the energy profile of the X-rays may cause different shock velocities due to both producing different drive pressures and by altering the material conditions ahead of the shock due to X-rays depositing their energy beyond the main shock front. Recent work from Ghosh *et al* [161] has studied the effect of M-band content on various dopant concentrations and found that with a higher proportion of hard X-rays the shock velocity increases slightly. This will be taken into account when adjusting shock timings between drive and capsule combinations.

A large number of pulse designs capable of igniting a capsule exist in 1D and the choice of which one is the best comes down to how the 1D performance, the 'clean' performance, translates to performance in higher dimensions and at the experimental level. Pulse shapes commonly used in experiments trade-off capsule compression, and therefore yield in 1D, for a greater hydrodynamic stability in higher dimensions. For the purposes of this investigation the exact structure of the pulse is not important rather how the hard X-ray content of the drive effects the conditions within capsule and the energy required for ignition. For this reason a 4-shock pulse has been chosen and only minor changes to the shock timings have been made between the different capsule and drive combinations.

The main pulse feature that can be used to scan over capsule implosion velocities is the peak height of the final shock. This is where most of the energy is delivered to the capsule and consequently where most of the hard X-ray energy is incident on the capsule. As the capsule yield is most sensitive to the capsule implosion velocity this is a good parameter to vary in order to find the cut-off energy required for ignition where the yield sharply increases. For this set of simulations the final peak drive temperature is varied between 285 eV and 310 eV and it is designed to be a 'no-coast' implosion where there is no switching-off of the radiation drive until bang-time, where the peak neutron yield occurs.

5.2.3 X-ray Spectrum

The spectral shape of the X-ray drive used is a Planckian with a gaussian shaped M-band component given, in units of W cm^{-2} Hz^{-1}, by the equation [162]

$$J = \sigma T_r^4 \Big((1-\alpha)\hat{I}_P + \alpha \hat{I}_G \Big) \tag{5.1}$$

For a given radiation temperature the spectral shape of the X-ray drive can be found from equation (5.1) where α is the peak fraction of the M-band gaussian relative to the Planckian peak. In equation (5.1) $\hat{I}_P$ and $\hat{I}_G$ are the Planckian and Gaussian functions respectively

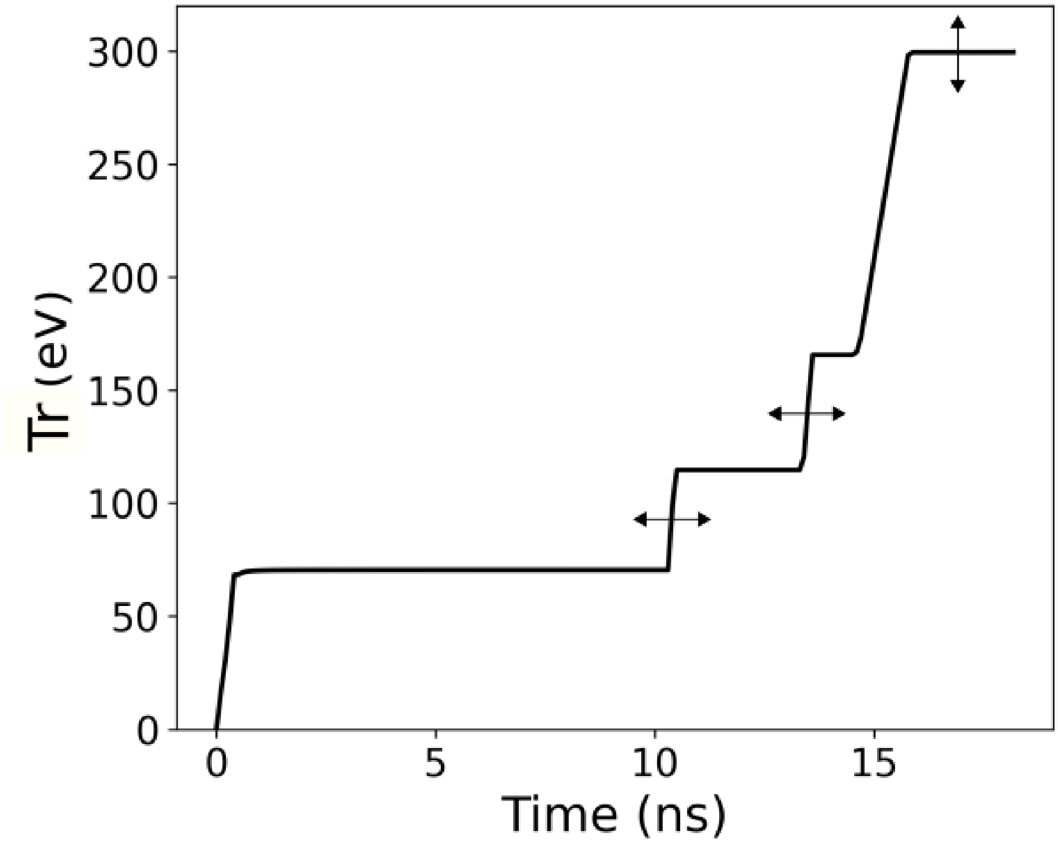

Figure 5.2: Figure showing the basic pulse profile used to implode the capsules in this study. Arrows indicate where slight adjustments to the 2nd and 3rd shock timings are made in order to ensure that no shocks merge before exiting the ice layer and where the peak drive is adjusted to scan over implosion velocities.

with their integrals normalized to unity.

$$\hat{I}_P(E_{\text{ph}}, T_r) \propto \frac{E_{\text{ph}}}{\exp(E_{\text{ph}}/T_r) - 1} \quad \text{such that} \quad \int_0^{\infty} \hat{I}_P dE_{\text{ph}} = 1 \tag{5.2}$$

$$\hat{I}_G(E_{\text{ph}}, E_{\text{ph},0}, \Delta) \propto \exp\left(-4\log 2 \frac{(E_{\text{ph}} - E_{\text{ph},0})^2}{\Delta^2}\right) \quad \text{such that} \quad \int_0^{\infty} \hat{I}_G dE_{\text{ph}} = 1 \tag{5.3}$$

Equations (5.2) and (5.3) define the shapes of the two components to the spectrum where E_{ph} is the photon energy, $E_{\text{ph, 0}}$ is the location of the M-band peak, Δ is the full width half maximum of the M-band gaussian and T_r is the radiation temperature of the drive. For

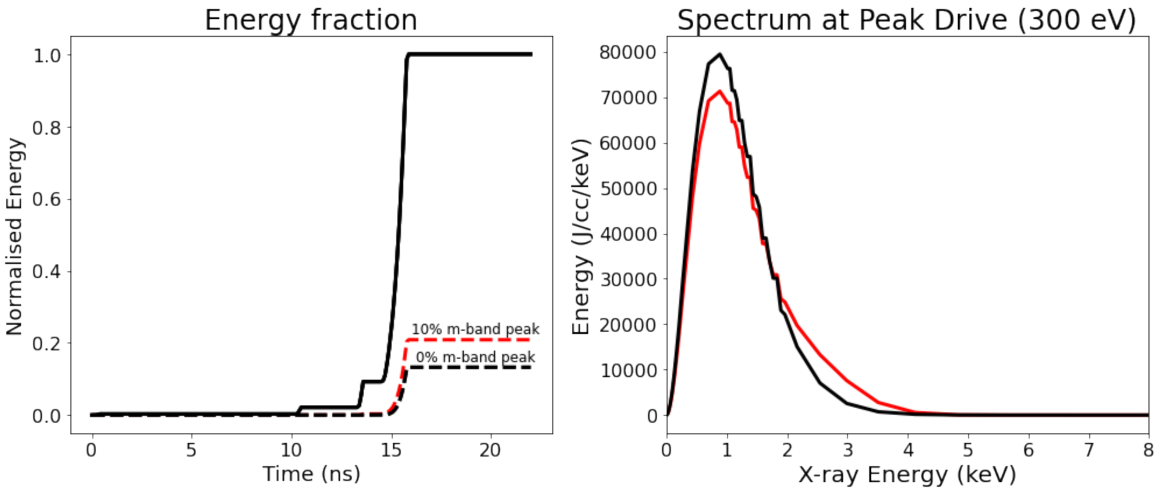

Figure 5.3: (Left) Plot of the radiation drive energy over time (solid line) along with the energy of X-rays with hν > 1.8 keV (dashed line). (Right) Spectral shape of the radiation drive at peak drive power for a Planckian drive (solid) and a Planckian drive with an approximation of a 10% M-band peak included.

these simulations $E_{\mathrm{ph},0} = 3$ keV and $\Delta = 1$ keV have been used in order to approximate the M-band which lies between 2 - 4 keV in gold. The exact structure of the M-band is difficult to model and for the current study it is not necessary to include a detailed M-band component.

The value of α used in equation (5.1) is obtained by fitting to the spectral data obtained in Chapter 4 such that the total energy for X-rays with hν > 1.8 keV (M-band X-rays) is consistent with the gold hohlraums simulated using h2d. This results in the hard X-ray energy profile shown in figure 5.3. For the purposes of this study the values of α used in these simulations, which to clarify is the M-band peak fraction, are values 0%, 5% and 10%. These values do not correspond to the total energy in the hard X-rays, both the M-band gaussian and the tail of the Planckian drive components contribute to the hard X-ray energy.

5.2.4 Shock Timings

The X-ray drive pulse is designed to put the capsule on a low adiabat ($\alpha = 1.4$) by gradually stepping up drive power in order to introduce the minimal amount of entropy according to equation (2.41). Each shock driven by the steps in the pulse leading to the final peak must be timed correctly to break out of the gas-ice layer in sequence. Shock trajectories can be visualised by plotting the following quantity, K on an radius-time axis where K is defined as

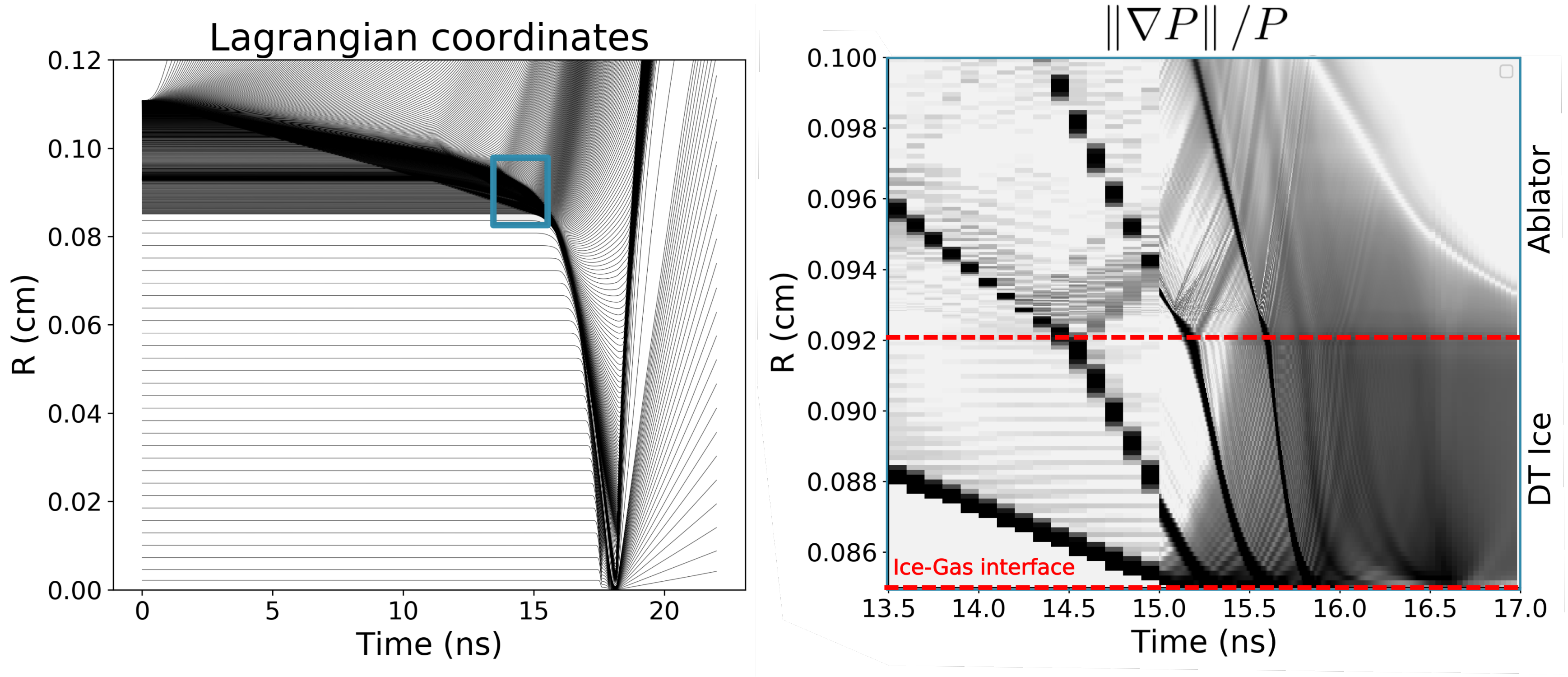

Figure 5.4: (Left) Lagrangian mass coordinates plotted as a function of time for a 1D capsule implosion driven by an X-ray source. (Right) Shock trajectories plotted as a function of time. Four shocks can be seen merging at the gas-ice DT boundary, the zoomed in section where the shocks merge is highlighted in blue.

$$K = \left\| \frac{\frac{dP}{dR}}{P} \right\| \tag{5.4}$$

where P is the pressure and R the radial position, see figure 5.4. In order to expedite the simulation of many different capsule and drive combinations the first three shocks are individually adjusted for each combination. The position of the final shock is then adjusted such that when the drive power of the final peak is adjusted the shocks remain well-timed and the adiabat of the capsule is constant between runs. This is achievable because so long as the final shock is kept from merging with the preceding shocks in or before the DT ice layer the capsule adiabat is fairly insensitive to small deviations in the final shock timing. By keeping the shocks from merging the differences in capsule entropy between the different capsule-drive combinations can be attributed to other factors such as X-ray preheat.

5.3 Results

5.3.1 1D Implosion Performance

We can use the following equation to describe the energy balance within the hohlraum

$$\eta E_{\text{laser}} = \sigma T^4 \left(A_{\text{cap}}(1 - \alpha_{\text{cap}}) + A_{\text{wall}}(1 - \alpha_{\text{wall}}) + A_{\text{leh}} \right) \Delta t \tag{5.5}$$

where η is the laser to X-ray conversion efficiency, A_{cap}, A_{wall} and A_{leh} are the areas of the capsule, the hohlraum wall and the laser entrance holes respectively, α_{cap} and α_{wall} are the albedos of the capsule and wall respectively. E_{laser} is the sum of the laser energy incident on the hohlraum and Δt is the pulse length. In equation (5.5) the radiation energy within the hohlraum has been dropped as it is negligible at these time and length scales. For the case of an empty cylinder the ratio of energy absorbed by the walls to the radiation energy ($E_V = 4V\sigma T^4/c$) contained in the volume, V is $\propto c\Delta t/d$ where d is the diameter of the cylinder. For hohlraums with d $\approx$ 0.5 cm and $\Delta t \approx 10^{-8}$ the radiation energy within the hohlraum is several orders of magnitude lower than the energy absorbed by the walls. To calculate the required laser energy the capsule albedo must first be determined from the 1D simulations. The surface area of the capsule is also required and will decrease in time as the implosion progresses. Due to the convergence, the time dependent ionization states and the changing composition of the capsule coronal plasma the $A_{\text{cap}}(1 - \alpha_{\text{cap}})$ term in equation

(5.5) will be time dependent. However, the terms relating to the hohlraum wall and the laser entrance holes shall be assumed constant for the analysis. In reality the re-emission region of the hohlraum wall would move inwards due to the heating by the X-rays and plasma would fill the hohlraum introducing other sources of energy loss and impeding laser beam propagation. The laser entrance holes would also begin shrink due to X-ray ablation, decreasing A_{leh} as time progresses. In addition, any higher dimensional effects that would impede the propagation of the laser are also neglected for simplicity.

Dopant (% Ge)	M-band (%)	Threshold laser energy (kJ)
1.00	0	827
1.00	5	811
1.00	10	800
0.50	0	800
0.25	0	783
0.00	0	752

Table 5.2: Table containing the calculated ignition threshold laser energies for each ablator dopant level with the M-band fraction of the drive pulse. Configurations that did not ignite over the range of parameters used in this investigation are not included.

For a hohlraum with a diameter of 5.75 mm, a length of 10.1 mm and an albedo of 0.9 equation 5.5 can be used to estimate the laser energy required for each of the capsule implosions simulated, see table 5.2. Assuming a total backscatter of 20% [163] and of the remaining 80% a laser conversion efficiency of 0.9 [164].

Table 5.2 shows the threshold laser energies required to achieve ignition for each capsule dopant level and M-band fraction. For the 1% Ge doped capsules the threshold laser energy decreases as the M-band fraction increases. This is in part can be explained by higher ablation pressures generated by the harder X-ray drives as more energy is deposited at the ablator surface than goes into heating the blow-off plasma for the more penetrating high M-band drives. Additionally, 0%, 0.25% and 0.5% doped capsules with M-band fraction above 0% do not ignite over the range of parameters used in this investigation and so are not present in Table 5.2.

The positions of each energy threshold for the 0% M-band simulations are plotted in figure 5.5 along with the data points for each dopant concentration. The locations of the ignition thresholds can be determined as the yield shows a sharp increase once it is reached. This threshold is the point at which the conditions in the DT fuel hotspot and the surrounding

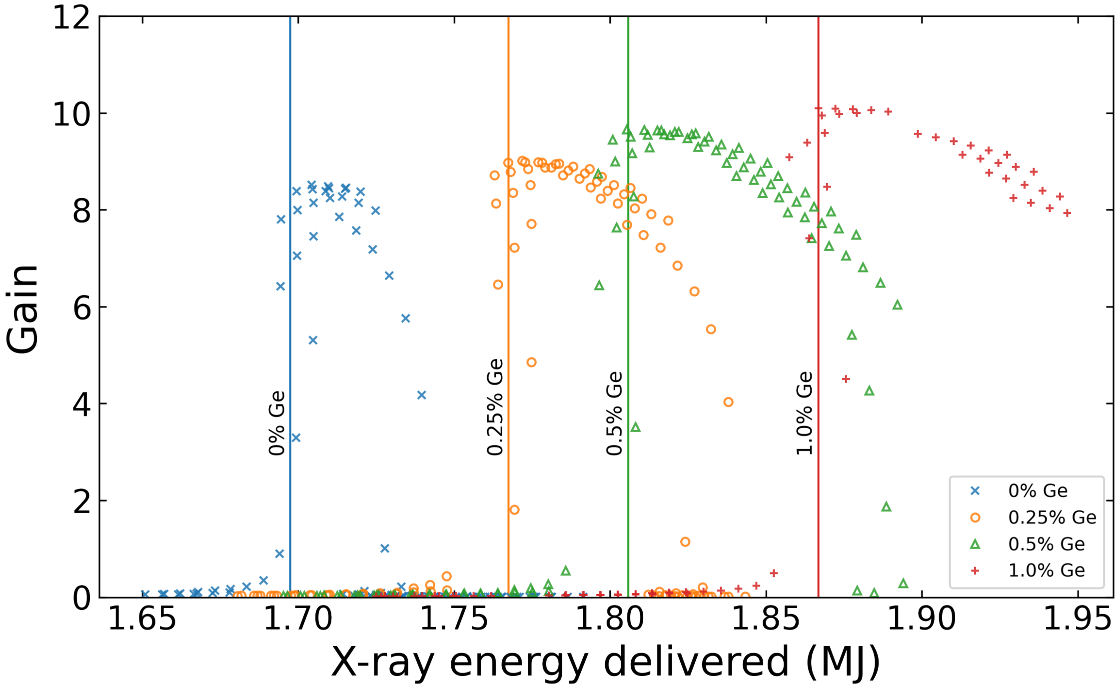

Figure 5.5: Total thermonuclear yield as a function of laser energy delivered to the capsule, inferred from the drive temperature and power balance equation obtained from the 0% m-band 1D hyades simulations. Results for each concentration of dopant are included.

dense DT is such that the alphas in the hotspot can initiate the self-sustaining thermonuclear burn-wave which continues until the capsule disassembles. This leads to the large difference in yields before and after the threshold as once the alpha deposition sets up the burn-wave a great amount of fuel can be burnt whereas without this mechanism the yield solely originates from the increased density and temperature in the hotspot from the PdV work performed on the hotspot by the decelerating shell. The PdV yields are on the order of hundreds of kJ which can be seen from figure 5.5 and amount to gains below 1. Here the gain is defined as the ratio of the energy from thermonuclear reactions to the total laser energy delivered to a given hohlraum.

$$\text{Gain} = \frac{E_{\text{Yield}}}{E_{\text{Laser}}} \tag{5.6}$$

It is observed that as the dopant concentration in the ablator is reduced the energy required for ignition also reduces. Going from 1% dopant concentration to 0% results in a decrease in the ignition threshold energy by almost 10%. Another feature present in figure 5.5 is a drop-off in gain beyond the ignition threshold. The ignition threshold has been obtained by scanning over various final peak drive temperatures and therefore for the capsules driven by the higher temperature pulses there is a greater amount of hard X-ray energy delivered in the final peak. This results in higher levels of preheat and a reduced final ρR. As the pulses with higher temperature final peaks contain more energy we see that for each dopant concentration there is an energy, or rather radiation temperature, beyond which the capsule fails to ignite. As the dopant concentration is reduced so to is the maximum drive temperature the capsule can be driven with before the opacity of the ablator becomes insufficient to prevent the X-rays in the high energy tail of the Planckian distribution from penetrating and preheating the fuel. This manifests in figure 5.5 as a narrowing of the range of energies where ignition occurs as the dopant concentration is reduced. For an un-doped (0% Ge) ablator the ignition energy range is quite narrow while for a 1% Ge doped ablator the capsule is still ignited even at the highest drive temperature used in this set of simulations of 310 eV.

Most of the decrease in the margin for ignition as the ablator dopant concentration is reduced is due to the reduced mass of the ablator. This can be seen from the scaling for the ignition energy $E_{\text{ign}} =\propto \alpha^{1.9} v^{-5.9}$ [100] where v is the implosion velocity and α is the adiabat at stagnation. Assuming a scaling for the implosion velocity from the equation for the kinetic energy of the imploding shell of $E = mv^2/2$ and the ignition energy scaling we can expect between the 1% doped and 0% doped capsules, which corresponds to a mass reduction of 1.3%, a reduction in the energy required for ignition of approximately 4%. This leaves around 6% of the observed energy reduction between the 1% doped and 0% doped capsules to account for, see table 5.2. This extra energy could be due to a deviation in the scaling law or from some other difference in the hydrodynamics or X-ray absorption caused by reducing dopant levels. Though out of the scope of this investigation it is important to note that the ignition threshold can also be affected by changing the composition of the hotspot. A different mixture of DT or different elements entirely will require a different hotspot temperature to reach the ignition criteria. In addition, other fuels will create products from the fusion reaction that differ from the alpha particles used to bootstrap the thermonuclear burn wave produced in DT hotspot ignition.

Coupled with the reduced-mass effect that removing dopant from the ablator has on the ignition threshold energy there is also an increase in ablation pressure observed as the ablation front enters the doped layers. Removing dopant from the ablator lowers the amount

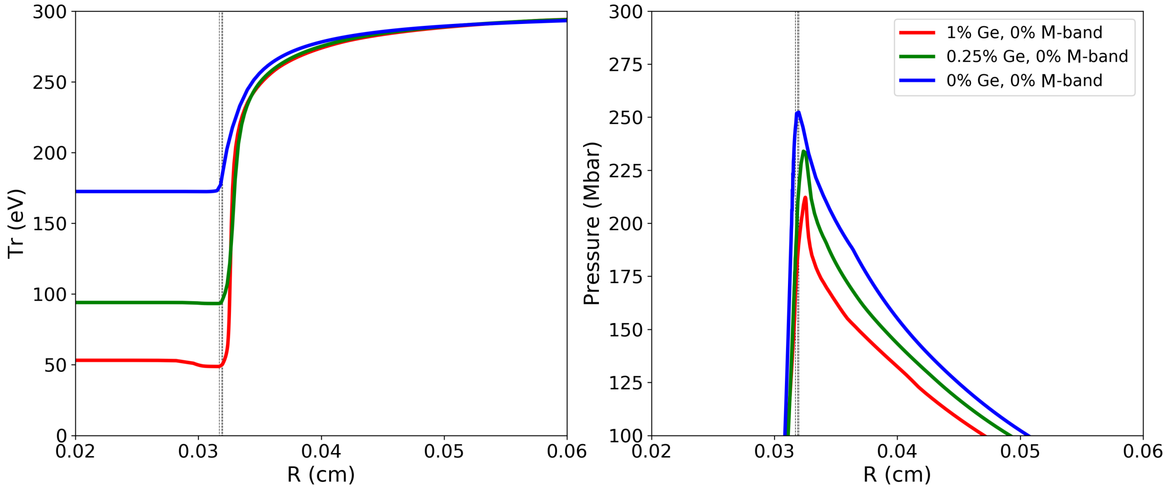

Figure 5.6: (Left) Radial profile of the radiation temperature at t = 17.5 ns inside the ablator for 1%, 0.25% and 0% dopant concentrations driven by a 4-shock 300eV peak X-ray drive with 0% M-band peak component. Each time snapshot has been adjusted slightly to ensure each capsule ablator is at the same radial position where the ice-ablator boundary is indicated by the vertical line. (Right) Corresponding pressure plotted as a function of radius for each dopant concentration again with the position of the ice-ablator boundary indicated by a vertical line.

of mid or high Z material that can radiate power away from the ablation front and reduce the ablation pressure. The presence of dopant at the ablation front or in the capsule coronal plasma will reduce the X-ray to capsule energy coupling in the final few nanoseconds of the drive pulse. This effect does not manifest earlier in the implosion as the doped layers have not yet been heated to sufficiently high temperatures. As can be seen in figure 5.6 higher ablation pressures are observed in the capsules with lower concentrations of dopant in the ablator at the time shown in the figure of 17.5 ns. The reduction in ablation pressure by dopant ions at the ablation front is compounded by a reduction in the X-ray flux reaching the ablation front by dopant in the coronal plasma. Additionally the removal of dopant from the ablator increases the radiation temperature beyond the ablator-ice boundary due to decreased opacity of the ablator to the high energy tail of the Planckian.

Looking at the ablation pressure as a function of time, in figure 5.7, the effect of the dopant at late times in the pulse can be investigated. The range of times in figure 5.7 cover the point shortly after the drive pulse reaches peak radiation temperature and ends once stagnation pressure becomes dominant. Ablation pressure begins to differentiate between the three dopant concentrations after the ablation front reaches the 1st dopant layer. At this stage the opacity of the ablation front to the drive X-rays increases and the ablation

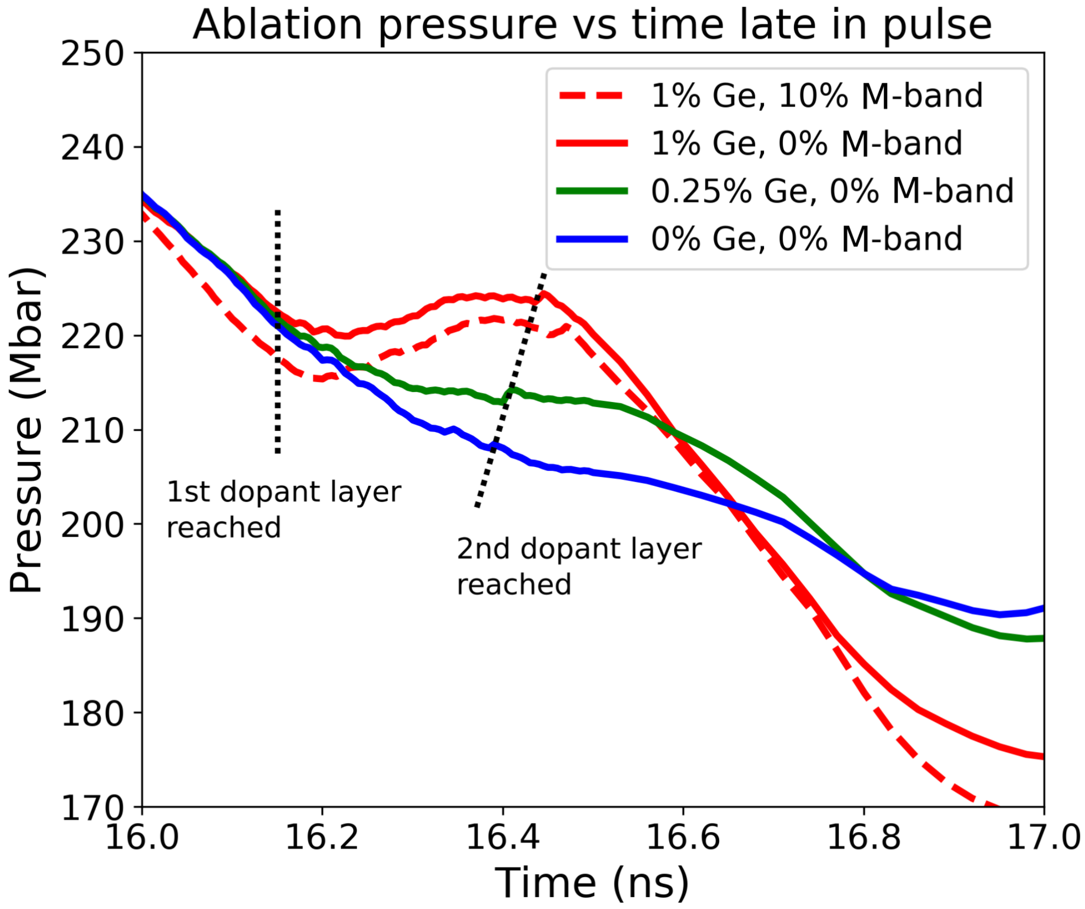

Figure 5.7: The ablation pressure over time for three different concentrations of dopant in the ablator driven by a multi-shock structured pulse with a 300 eV peak drive temperature. Points where the ablation front reaches the different doped layers are indicated with dotted lines (in the 1% doped ablator the layers go (1) 0.5%, (2) 1% and (3) 0.5%).

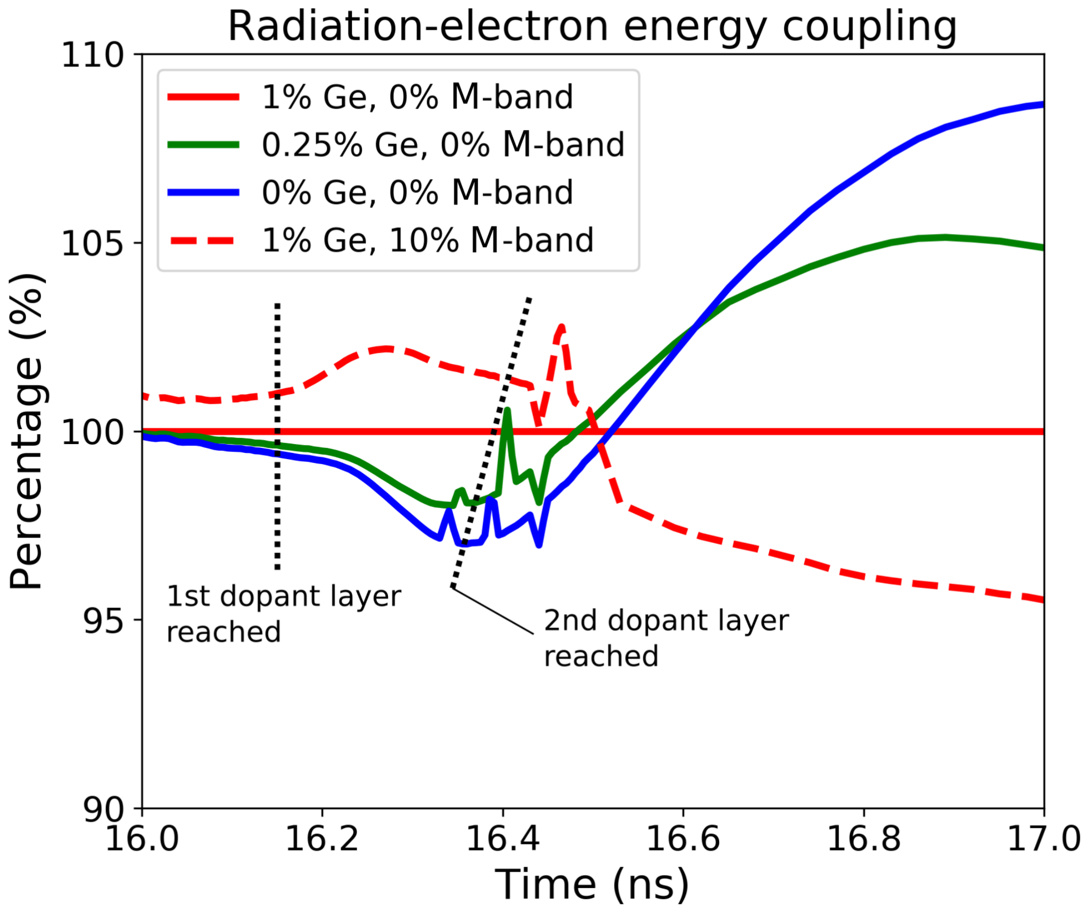

Figure 5.8: The electron energy coupling (the net amount of radiation energy absorbed / emitted by electrons in the plasma) for several dopant concentrations is plotted relative to the 1% doped capsule driven by a 0% M-band drive. Points when the ablation front reaches the doped layers are indicated by the dotted lines.

pressure is seen to be higher for capsules with a higher dopant concentration. Once the ablation front reaches the 2nd doped layer there is sufficient dopant near the ablation front and in the coronal plasma that the power being radiated lowers the ablation pressure. The higher the dopant concentration the greater the drop in pressure. As can be seen from the time-dependent ablation pressure when the dopant concentration is increased there is competition between the increase in X-ray absorption and the increase in the power radiated by the ablator.

Included in figure 5.7 is the ablation pressure for a 1% doped capsule driven by a spectrum with a 10% M-band peak (dashed) for comparison with the same capsule driven by a 0%

M-band spectrum (solid). In comparison, the doped capsule driven by a spectrum with an M-band component has a lower ablation pressure than the doped capsule driven by a purely Planckian spectrum. This is due to the higher energy M-band X-rays penetrating and heating deeper into the ablator, spreading their energy deposition, and thus heating a larger mass. This leads to a lower ablation pressure in the capsule driven by the 10% M-band spectrum than in the same capsule driven by a 0% M-band spectrum. This is due to the fact that the X-ray drives have been set up such that the energy of a drive with temperature T is the same regardless of the presence of an M-band component.

Figure 5.8 shows the radiation-to-electron energy coupling relative to the 1% doped capsule, $E_{\mathrm{r}\to\mathrm{e}}$. As previously stated, the capsules with lower dopant concentrations have an initially lower radiation-electron coupling due to the initially lower opacity. However, as dopant layers are heated and enter the coronal plasma the radiation-energy coupling increases for the reduced dopant capsules relative to the 1% doped capsule. Also, relative to the 1% doped capsule it can be seen that more power is being delivered to the electrons by the drive early in figure 5.8 when driven by a 10% M-band spectrum.

Accounting for the decreasing radius, R, of the capsule gives a better picture of the relative radiation-electron energy coupling between the capsule and drive combinations. As the capsule converges the surface area that can absorb the drive X-rays decreases and so the total power absorbed by the capsule decreases proportional to R^2. X-ray energy is coupled to the ablator through inverse bremsstrahlung by free electrons in the plasma and line absorption from bound electrons, predominately in the dopant layers. Energy is then coupled to the ions in the ablator through electron-ion collisions. Figure 5.9 plots $E_{\mathrm{r}\to\mathrm{e}}/R^2$ relative to the 1% doped 0% M-band implosion. It can be seen that the relationship between the decreased dopant concentrations and the radiation-electron coupling persists however the 1% doped capsule driven by the 10% M-band spectrum shows a consistently higher amount of total power delivered to the electrons. This is due to the harder spectrum penetrating more deeply into the doped layers and thus causing the ablator to expand such that the density of the ablator is lower. The lower density doped layers are then heated to higher temperatures than in the 1% doped capsules driven by a 0% M-band spectrum resulting in a higher level of ionization and a lower amount of power radiated, see figure 5.10. This still leads to the observed lower ablation pressure for the 1% Ge capsule driven by the 10% M-band spectrum due to the fact that the energy deposition is spread over a larger depth

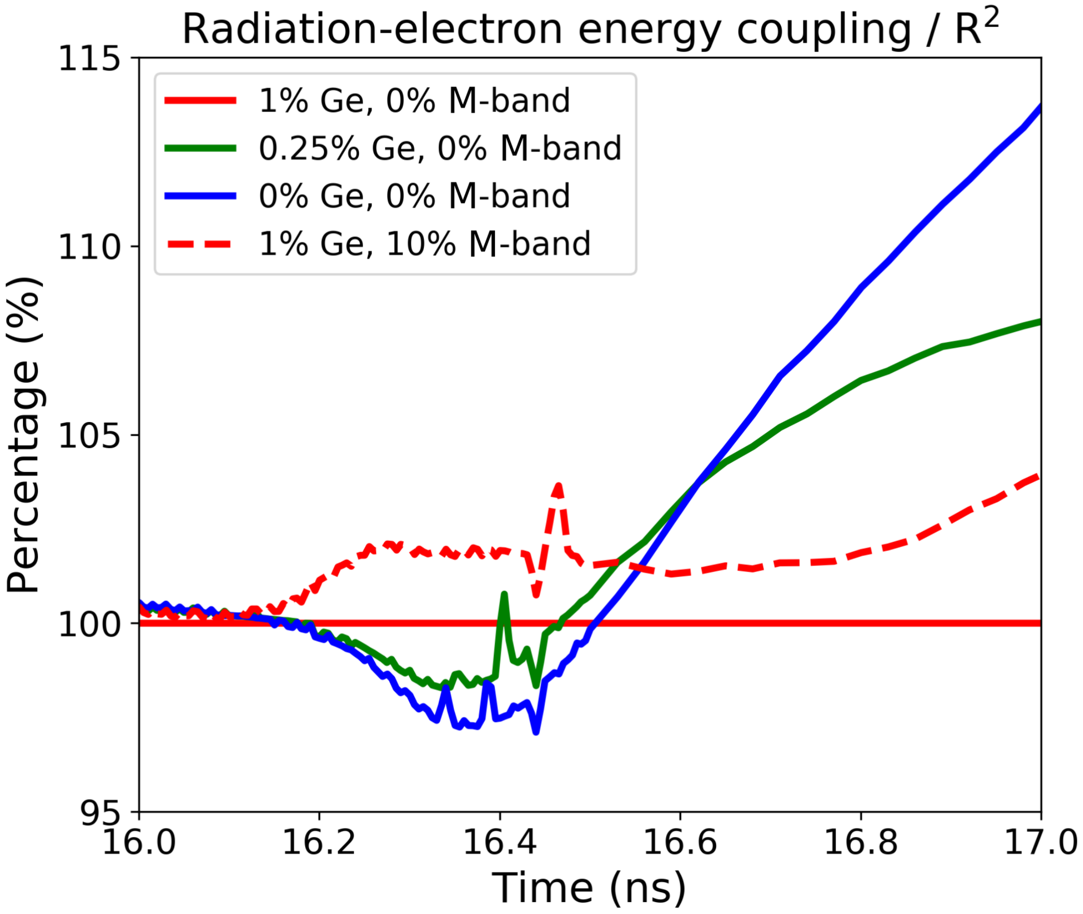

Figure 5.9: The electron energy coupling divided by the capsule radius squared is plotted relative to the 1% doped capsule driven by a 0% M-band drive.

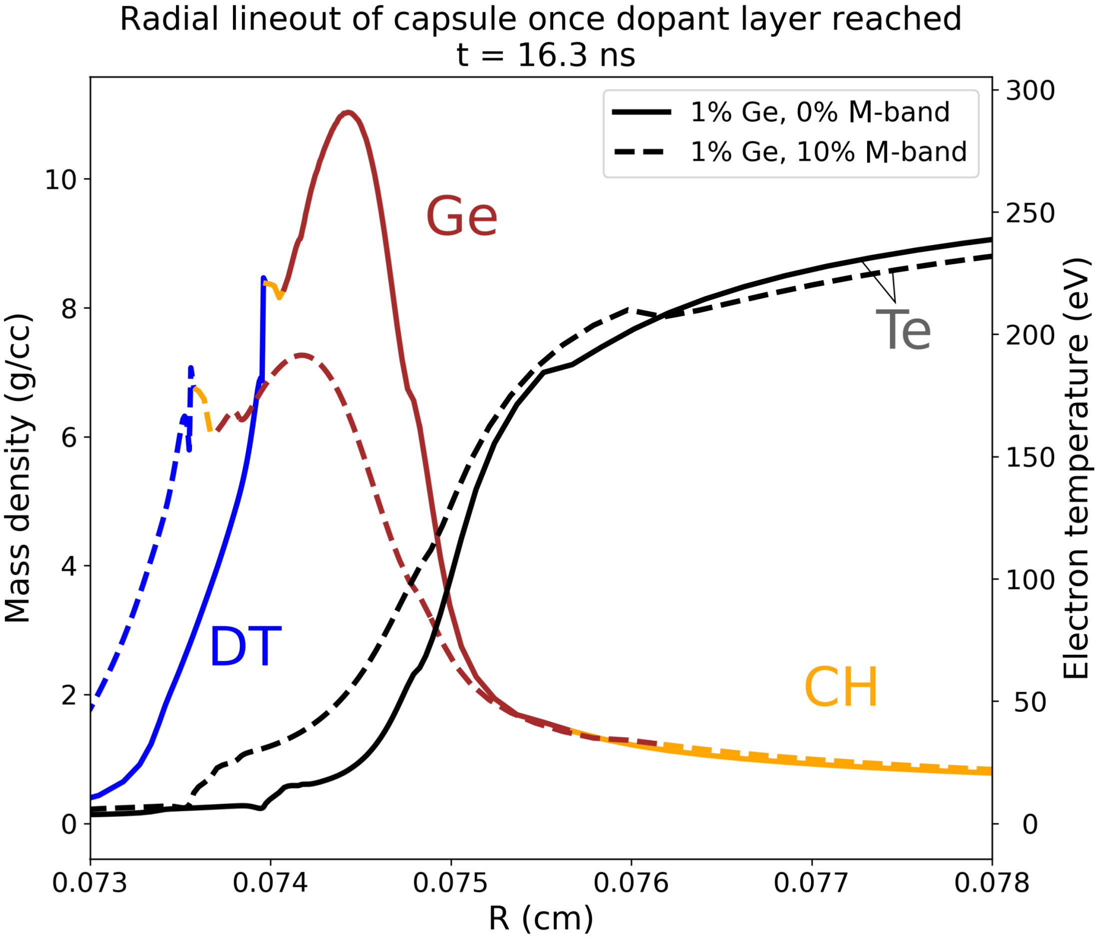

Figure 5.10: Radial snapshot of the mass density and electron temperature profile for a 1% Ge doped capsule once the ablation front moves into the 2nd doped layer at $t = 16.3$ ns. Different material regions are coloured and labelled. The dashed line corresponds to a capsule driven by a drive spectrum with a 10% M-band component.

than in the same capsule driven by a Planckian spectrum.

Figure 5.10 contains high density features in the doped layers near the ablator-ice interface. These features are due to the passage of the shocks through the doped layers. Due to the multiple doped layers present in the capsule each shock upon traversing has some portion of its energy transferred into an outwardly propagating reflected shock. The multiple incoming and reflected shocks thus create a complex density profile in the doped region.

To summarise, the reduced dopant capsules have a lower relative radiation-electron coupling (approximately -2.5%) compared to the 1% doped capsule. This lower coupling lasts for around 300 ps until it increases to upwards of 15% for the 0% doped capsule due to the reduced high-Z material in the capsule coronal plasma. This period of increased radiation-electron coupling lasts for around 600 ps thus creating a net increase in the efficiency of the target during the final few nanoseconds of the drive.

5.3.2 Predicted 2D Stability

One of the most important processes not captured in these 1D simulations is the perturbation and mixing of material at the various density interfaces in the ablator that become hydrodynamically unstable during the implosion. The later into the implosion we observe in 1D the less likely the results are to be consistent with higher dimensional simulations and experimental capsule implosions.

It is nevertheless important to quantify the stability of the capsule particularly comparing between different dopant concentrations and drives. As one of the motivations of removing the dopant in addition to the reduced ablator mass is the removal of material interfaces. This leads to a lower Atwood number of the ablator therefore reducing the rate at which hydrodynamic instabilities grow.

Figure 5.11 shows in arbitrary units the linear growth rate, ignoring the stabilizating mechanisms described in equation (2.23), of the Rayleigh-Taylor instability $\hat{\gamma}$ for a wavenumber $k = 1$ defined as

$$\gamma = \Re\{\sqrt{gA}\} \tag{5.7}$$

where $\Re$ denotes the real part of the bracketed expression, g is the acceleration of the shell and A is the Atwood number given by equation (2.22).

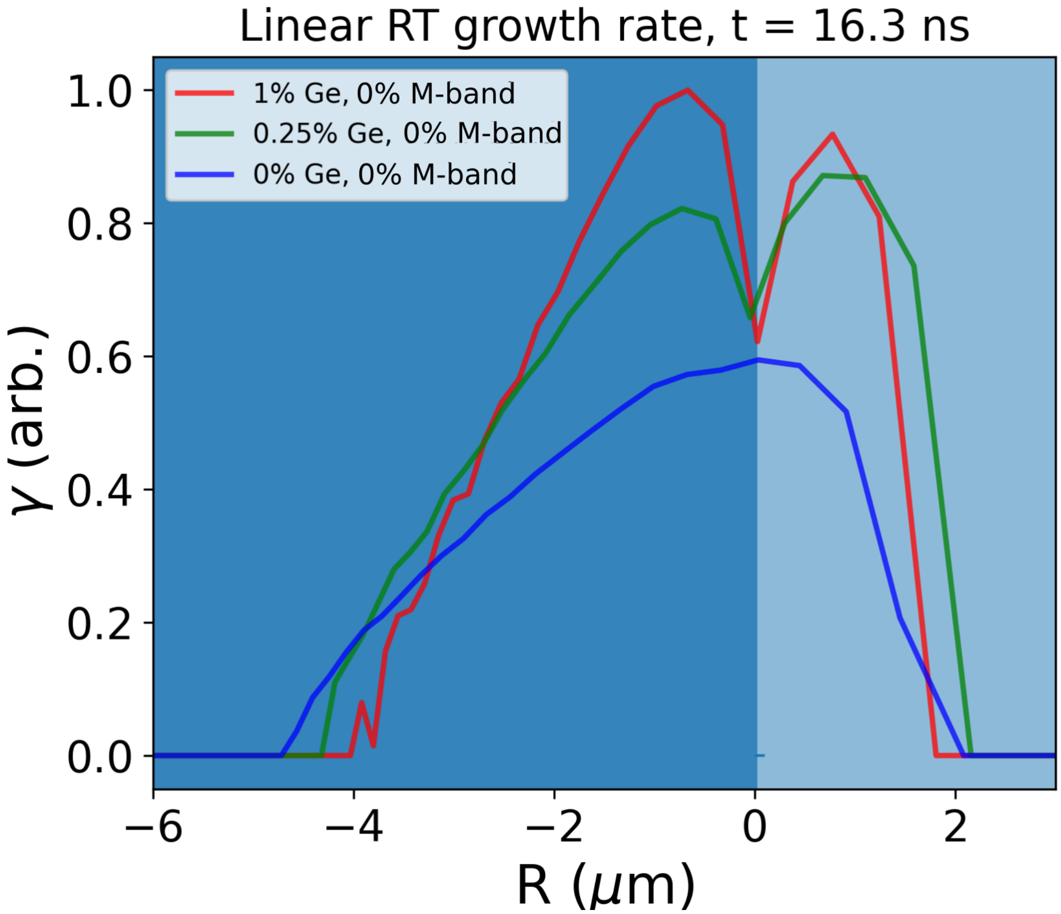

Figure 5.11: The linear growth rate of the Rayleigh-Taylor instability for a wavenumber k=1 expressed in arbitrary units at the time the ablation front has reached the doped layers as a function of radial distance. Distances on the x-axis are given relative to the boundary between the first and second doped layer. The shaded regions indicate the locations of the doped layers; layer 2 (dark) and layer 1 (light).

In figure 5.11 the RT growth rate for three capsules with varied dopant concentrations driven by a Planckian spectrum are compared. The final peak radiation temperature of the drive pulse is 300 eV as with the results discussed previously. The radial snapshot is taken at the time used in figure 5.10 when the ablation front has reached the doped layers. It can be seen that the 0% Ge doped capsule has approximately a 40% reduction in the 1D linear RT growth rate when compared to the 1% Ge doped capsule. A smaller reduction in the growth rate is observed in the 0.25% Ge doped capsule of approximately 20%. While this results demonstrates that the removal of dopant layers lowers the instabilitiy growth at the locations in the ablator where the dopant usually sits 2D or 3D simulations are required in order to properly quantify the reduction in instability growth and subsequent mixing of ablator material. The presence of imperfections at the interfaces created within the ablator by introducing dopant layers and their effect on seeding instability growth is also something that would be reduced by their removal which is not captured in the 1D simulations.

Another boundary that becomes important late in the implosion is the boundary between the DT ice and the ablator. In the capsules used in this study the inner ablator surface is undoped and the doped layers are offset from the ice-ablator boundary. Late into the pulse the X-ray ablation front will reach the doped layers and the higher energy X-rays in the drive spectrum originating from the tail of the Planckian distribution plus any M-band component will be able to penetrate and heat the ablator near the ice-ablator boundary.

Figure 5.12 plots the Atwood number of the ice-ablator boundary as a function of time for the three dopant concentrations driven by the Planckian spectrum. As the dopant concentration is reduced the high energy X-rays are allowed to heat and expand the inner ablator material more, reducing the density there and therefore increasing the Atwood number at the ice-ablator boundary making it unstable to the RT instability late in the pulse. This effect is present even when utilising a drive with no M-band component as the high energy tail of the Planckian is sufficient to penetrate and preheat the material at the boundary.

Looking at this effect late into the implosion can be misleading as the RT instability in other regions of the ablator seeded near the beginning of the implosion will have had sufficient time to grow large. This will create deformations to the ablator and mixing of ablator material that may affect the occurrence of this late-time ice-ablator instability. In addition, the length of time that the ice-ablator instability has to grow is smaller than that of the ablation front instability shown in figure 5.11 which occurs earlier in the implosion.

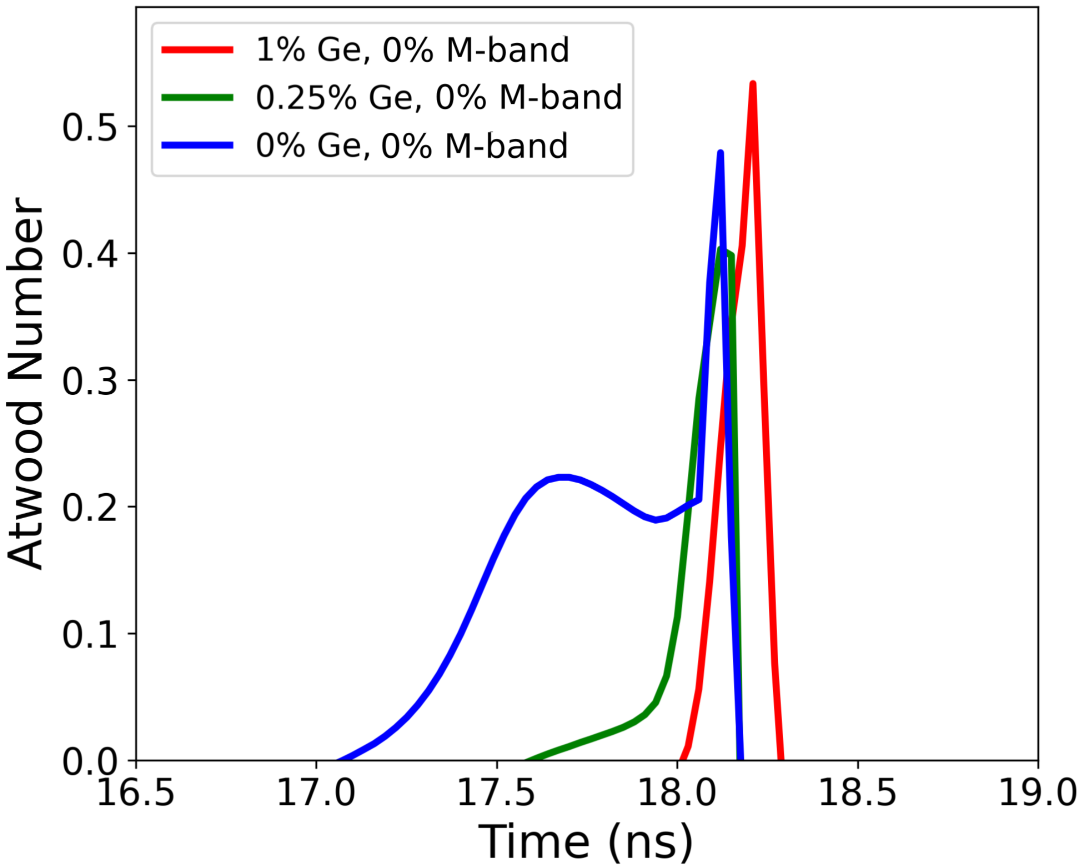

Figure 5.12: The Atwood number for the ice-ablator interface is plotted as a function of time for three dopant concentrations driven by a Planckian spectrum with a final peak temperature of 300 eV. The sharp peak in each of the Atwood number curves corresponds to the point at which ignition occurs and the burn wave propagates outward from the hotspot.

While the precise effect of the ice-ablator instability cannot be determined by these 1D simulations its presence and relative magnitude as a function of dopant concentration still demonstrates some potential limit to the amount of dopant that can be removed from the capsule.

5.4 Discussion

In this work we have examined the effect of varying both the M-band component of the X-rays drive and the dopant concentation in the ablator. This has been done in conjunction with varying the peak drive temperature and therefore the peak implosion velocity of the capsule in order to scan over implosion velocities and determine the threshold for ignition.

When looking at removing dopant from the ablator the corresponding mass reduction and increase in drive coupling results in a lowering of the threshold energy required for ignition by approximately 7.3% going from 1% Ge to 0% Ge. The 0% Ge doped CH ablator ignites only for the Planckian drive spectrum as a 5% and 10% M-band component results in too much preheat and therefore insufficient compression of the fuel. The 0% Ge doped capsule also exhibits a narrower range of peak drive temperatures at which ignition occurs. This points towards the 0% Ge doped capsule being more sensitive to the high energy X-ray content of the drive as is expected from removing the high opacity Ge layer. The 0.25% Ge doped design provides a wider range of peak drive temperatures in which ignition occurs while reducing the capsule sensitivity to high energy X-rays.

The ablation pressure has been found to be sensitive to changes in the dopant concentrations. This is due to an increase in the X-ray to electron energy coupling in the reduced dopant capsule relative to the 1% doped capsule. This relative increase in coupling is preceeded by a decrease due to the lower opacity of the reduced dopant capsules relative to the 1% Ge doped capsule. However, this lower relative coupling (approximately a -2.5%) lasts for around 300 ps while the relative increase (approximately a $+15\%$) in coupling due to the reduced high-Z material in the capsule coronal plasma lasts for around 600 ps. This is a benefit as it increases the efficiency of the target during the final few nanoseconds of the drive.

The trade-off between sensitivity to high energy X-ray preheat and a decreased threshold for ignition has been demonstrated in 1D. Though some small amount of dopant may be required in order to ensure ignition for other pulses with higher peak drive temperatures, in 1D the 0% doped capsules have been shown to ignite over a small range of laser energies while having a lower Rayleigh-Taylor growth rate and fewer boundary sites at which hydrodynamic instabilities may be seeded. Though the ignition criterion may not be met when going to 3D, accounting for hydrodynamic instabilities and mixing, the fundamental principle of removing dopant and its relative effect on the threshold energy for ignition implies a potential avenue for approaching ignition. The removal of dopant will be a trade-off between capsule sensitivity to hard X-rays and the energy gains due to lower losses and reduced ablator mass. If hohlraums that can produce an X-ray drive spectrum close to a Planckian can be realised then the removal of dopant from the capsule could lower both the energy thresholds for ignition and the effect of hydrodynamic instabilities and mixing.

Chapter 6

Hohlraum Albedo Profiling

Using a hohlraum to generate X-rays comes with many benefits in regards to inertial confinement fusion. A motivation for their use is in order to smooth the deposition of energy spatially over the capsule ablator surface. Also, by moving the laser-plasma interaction sites away from the capsule and onto the surface of the hohlraum walls there is less opportunity for harmful laser-plasma interactions within the capsule coronal plasma.

A drawback of using hohlraums is that they require the laser beams to travel through an environment where high-Z plasma is expanding and often impeding the propagation of the laser beams to their intended deposition site on the hohlraum wall. This can affect the implosion symmetry by altering the pattern of energy deposition on the hohlraum wall and also lowers the laser-hohlraum energy coupling efficiency by causing more energy to be reflected out of the laser entrance holes.

The size and shape of a hohlraum is determined by several factors. Firstly, the peak radiation temperature required from the hohlraum will be determined from the capsule implosion conditions needed to achieve ignition - most ignition designs sit somewhere around a 300 eV peak radiation temperature. With this the available power of the laser then sets the volume of the hohlraum required to achieve these temperatures, as radiation energy density of a Planckian depends on T^4 the radiation temperature will scale as the hohlraum volume $V^{-1/4}$ ($R^{-3/4}$ for a spherical hohlraum of radius R for example). The size and shape is also restricted by the required symmetry smoothing where the parameter of importance is the case-to-capsule ratio. This ratio is the relative size of the capsule radius to the hohlraum radius, the larger case-to-capsule ratio the greater the smoothing effect on the radiation field incident on the capsule surface.

These two fundamental hohlraum parameters are determined by the requirements of the capsule but are linked themselves to the laser interaction with the hohlraum as they will determine the extent and location of the high-Z plasma that is ablated from the walls during the pulse. For this reason the shape of the hohlraum is an important feature as it will determine both the symmetry smoothing and the environment in which the laser will propagate. Reducing the coupling between the shape of the hohlraum and the radiation symmetry may allow for a greater variety of hohlraum designs aimed at minimising the effect of high-Z hohlraum plasma on the propagation of the laser beams.

To do this hohlraums with a z-axis dependent albedo profile are proposed. In current cylindrical hohlraum designs there are two cones of laser beams: the inner cone, which is incident on the hohlraum wall close to the waist of the capsule; and the outer cone, which impacts the hohlraum wall closer to the laser entrance holes. This setup is used in order to maintain a spherical implosion by adjusting the power delivered by the inner or outer cones so to balance between a waist heavy (sausage shaped) or a pole heavy (pancake shaped) implosion respectively. The expansion of the high-Z hohlraum wall plasma can change the relative locations of laser hotspots therefore creating a time-dependent symmetry swing in the capsule drive. Adjusting the relative power of the inner and outer cone during the implosion is a way of counteracting this symmetry swing.

During the laser pulse the propagation of the inner cone of the laser beam becomes impeded by plasma which expands from the hohlraum wall due to laser and X-ray ablation. As the density of the high-Z hohlraum wall plasma in the path of the inner cone increases less and less of the laser energy reaches the desired location on the waist of the hohlraum. This results in an X-ray flux profile from the hohlraum which drives the poles of the capsule (areas closest to the laser entrance holes) harder. An uneven drive such as this results in pancake shaped capsule implosions thus reducing the efficiency of the compression and increasing energy loss from the fuel hotpot.

When going to lower hohlraum fill densities in order to increase laser to hohlraum coupling by reducing laser-plasma instabilities the problem of symmetry swings caused by expanding hohlraum plasma is exacerbated [165]. In order to account for the propagation of the laser beams in hohlraums with lower gas-fill density several solutions have been investigated such as altering the hohlraum geometry [52, 53, 101] and making use of beam phasing [166, 167] available due to the reduction in cross-beam-energy transfer in near-vacuum hohlraums.

Hohlraums that consist of a doped wall with an albedo that varies over the length of the hohlraum may be able to provide another option to target designers by separating hohlraum drive symmetry from laser propagation. In reality this amounts to allowing the hohlraum dimensions to remain fixed while using an albedo profile in order to augment the symmetry tuning. Having another avenue in which to tune the symmetry of the implosions would allow for more flexibility in terms of the laser hotspot location and the overall shape of the hohlraum. Increasing the albedo of the wall has already been demonstrated with cocktail hohraums [148]. Decreasing the albedo of the wall amounts to choosing an element that is a less efficient radiator (lower Z), though this will also impact the laser to X-ray conversion efficiency. Determining the exact material composition required to achieve the albedo differences presented in this work is out of scope.

In this work a view factor model is used to assess the level of low order symmetry control obtainable from a hohlraum with an albedo profile. Symmetry tuning has not been performed on the initial uniform albedo hohlraum as this study intends only to look at the possible symmetry control possible from an albedo profiled hohlraum. The combined design that would achieve the required levels of drive symmetry onto the capsule (<1%) would contain a combination of tuning the case-to-capsule ratio, adjusting laser pointing and relative power between cones and altering the hohlraum shape. In a time-dependent treatment the relative power to laser cones would also be varied in order to compensate for the convergence of the capsule as it is compressed by the drive and for the movement of the hohlraum walls.

6.1 Albedo profiling of a laser driven hohlraum

The following function, y_1 has been used to obtain a linear albedo gradient on the inside wall of the hohlraum, reaching a maximum of a_0 at the top and bottom of the hohlraum ($-L/2 \leq z \leq L/2$) where L is the length of the hohlraum.

$$y_1(z) = 2a_0(1 - C)\frac{\|z\|}{L} + Ca_0 \tag{6.1}$$

In equation (6.1) C is the fractional decrease in albedo relative to the maximum, a_0, at the middle of the hohlraum ($z = 0$).

Term 2 on the right-hand side of equation (5.5) represents the power absorbed into the wall for a hohlraum with a wall area A_{wall} and an albedo of α_{wall}. Equation (5.5) assumes a

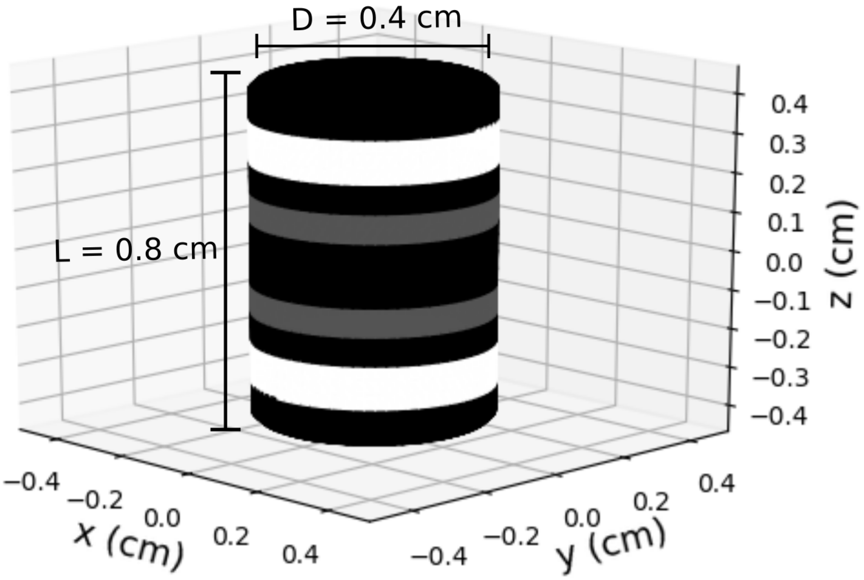

Figure 6.1: The source profile on the hohlraum for a 2 ring source consisting of two sets of inner and outer beams.

constant hohlraum albedo with respect to the wall coordinates, in our case cylindrical. To treat the hohlraums studied in this chapter the following expression is evaluated, A'.

$$A'_{\text{wall}} = \pi D \int_{-L/2}^{+L/2} \alpha(z) dz \tag{6.2}$$

where $\alpha(z)$ is the hohlraum wall albedo as a function of the coordinate and D is the hohlraum diameter, which is constant. The higher the integral in equation (6.2), the higher the radiation temperature within the hohlraum, all other terms in equation (5.5) being kept constant. Substituting the function in equation (6.1) for the albedo and integrating gives

$$A'_{\text{wall}} = \pi D L a_0 \left(\frac{(1-C)}{2} + C \right) \tag{6.3}$$

Letting $A'_{\text{wall, 0}}$ be $A'(C)$ at $C = 1$, a hohlraum with constant albedo with respect to z, the percentage change in absorbed power as a function of C can be expressed as

$$\frac{A'_{\text{wall}}(C)}{A'_{\text{wall, 0}}} = \frac{(1-C)}{2} + C \tag{6.4}$$

Applying the linear albedo profile y_1, equation (6.1), to the hohlraum wall the laser arrangement shown in figure 6.1 for several values C the pole to waist flux symmetry can be adjusted. These results are shown in figure 6.2 where it can be seen that varying the value of C from 0.8 - 1.0 the pole to waist symmetry can be adjusted through approximately $+5\%$ to -10%. Pole to waist flux percentages have been determined as a function of C to within 1% based on the resolution of the mesh used. From equation (6.4) this corresponds to a range of total power radiated by the cylinder from $100\% - 90\%$, excluding the material surrounding the laser entrance holes. The drop in power required to bring the pole to waist flux symmetry to 0% for this specific laser pointing and power distribution amounts to approximately 96%.

If we assume that, keeping all other dimensions fixed, the P_2 symmetry on the capsule scales with the inverse of the hohlraum radius [168], R_h, then in order to create the 15% pole to waist symmetry swing by changing the case to capsule ratio of the hohlraum the area of the hohlraum will increase by approximately 32%. This implies that, ignoring the increase in laser entrance hole size, at least 32% more laser power would be required to generate the same radiation temperature. This sort of symmetry control is usually achieved via laser pointing and altering the amount of power in each of the laser beam cones. This calculation is merely to put the 10% drop in absorbed power into context. In the application of hohlraum albedo profiling the required symmetry swing from albedo profiling would be lower as it would be achieved in conjunction with the laser pointing and power adjustments.

Equation (6.1) can be written in a generalised form in terms of n, where n determines the slope of the function. For $+dy_n/d\|z\|$ (increasing albedo away from the hohlraum waist)

$$y_n = a_0(1-C)\left(\frac{\|z\|}{L/2}\right)^n + Ca_0 \tag{6.5}$$

and for $-dy_n/d\|z\|$ (decreasing albedo away from the hohlraum waist)

$$y_n = a_0(C-1)\left(\frac{\|z\|}{L/2}\right)^n + a_0 \tag{6.6}$$

This leads to a general form of the percentage change in absorbed power A'

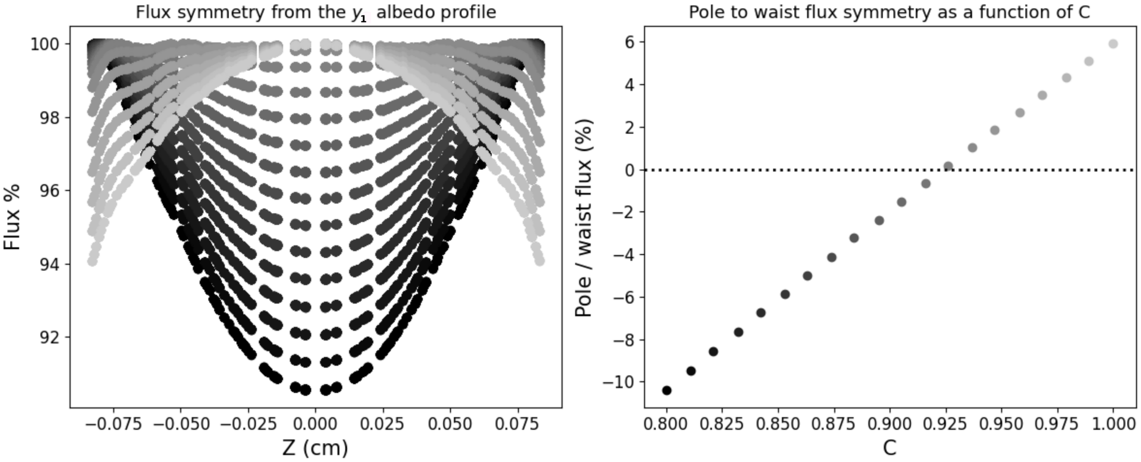

Figure 6.2: (Left) The flux symmetry onto the capsule as a function of z-axis position for each value of C for the y_1 albedo profile. (Right) The ratio of the pole flux to the waist flux onto the capsule as a function of C. Pole to waist flux ratio passes through 0% at approximately a C value of 0.925 which corresponds to a drop in total radiated power to 96.25% of the total radiated power of a uniform albedo hohlraum.

$$\frac{A'_{\text{wall}}(C,n)}{A'_{\text{wall, 0}}} = \frac{(1-C)}{n+1} + C \tag{6.7}$$

Where it can be seen that as $n \to \infty$ equation (6.7) tends toward C, though changes in the absorbed power can be expected to go below 1% for values of n > 100. For high values of n a greater area of the hohlraum wall will have a lower albedo and therefore it follows that the loss in radiated power increases correspondingly. There will therefore be a trade-off between loss in radiated power by the hohlraum wall and the symmetry control possible from an albedo profiled hohlraum.

The pole to waist symmetry symmetry obtained at the National Ignition Facility for a low gas fill hohlraum is approximately 5% falling to below 1% at the peak of the pulse due to capsule convergence [169]. Similar levels degrees of symmetry have been demonstrated here using albedo profiling in conjunction with keeping the positions of the lasers fixed. However, the primary importance of albedo profiling in the context of a laser driven hohlraum is to allow the lasers to be pointed in such a way as to maximise the coupling of laser energy to the hohlraum while using albedo profiling to adjust the flux symmetry.

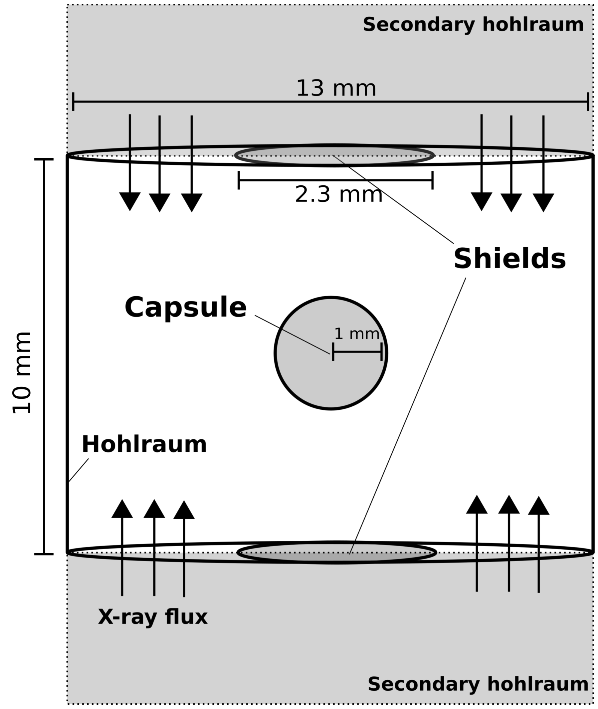

Figure 6.3: Diagram showing a double-ended Z-pinch hohlraum containing radiation shields. The region labelled 'secondary hohlraum' would consist of a wire array that creates the radiation field that drives the capsule in the main hohlraum, specific details are omitted from the diagram.

6.2 Albedo profiling of a Z-pinch hohlraum

A double-ended Z-pinch hohlraum consists of a hohlraum that contains a pair of wire arrays through which a large current is passed in order to heat and compress the arrays. Due to the $v \times B$ force the wire arrays converge towards the center of the hohlraum where they stagnate, converting kinetic energy into heat and an thus act as an intense X-ray source.

Double-ended Z-pinch hohlraums consist of two secondary hohlraums each containing a wire array and a main hohlraum containing the capsule. Upon the heating, compression and convergence of the wire arrays they produce a source of X-rays which rise in intensity once the array has converged and stagnated on the hohlraum axis. The secondary hohlraums are typically made from a high-Z material (usually gold) in order to enhance the radiation confinement. The X-ray flux from the secondary hohlraums enters into the main hohlraum, figure 6.3. This radiation flux is then confined within the main hohlraum and drives the implosion of the capsule. Radiation shields are required in order to prevent the poles of the capsule being driven harder than the waist of the capsule thus resulting in an asymmetric implosion. The case-to-capsule ratio of the main hohlraum can also be adjusted in order to alter the radiation symmetry onto the capsule. Capsules are designed to achieve ignition via volume ignition, an inertial confinement fusion scheme where the hotspot, either through its size or by including a high Z tamping layer, absorbs the bremsstrahlung radiation generated at stagnation thus reducing losses and raising the hotspot temperature. The capsules are also designed to not require careful tailoring of the pulse shape to drive shocks. These double shell capsules [170] drive multiple shocks by accelerating an outer shell until it impacts an inner shell thus creating a second shock via the collision. That shock then merges with the initial shock that originated from the X-ray drive in the outer shell and has been travelling through the outer shell during the acceleration. This design does not require a drive pulse with the structure of a traditional hotspot ignition capsule as the shock timing is predominantly determined by the dimensions and composition of the capsule.

Unlike in a laser driven hohlraum, Z-pinch driven hohlraums do not benefit from the symmetry tuning available via adjusting laser pointing. The absence of laser beams does however mean that there is no requirement to consider the propagation of the beams through the hohlraum plasma. The primary means of adjusting the low-order radiation symmetry onto the capsule is then down to the size and shape of the main hohlraum and the position and size of the radiation shields. For Z-pinch hohlraums where the flux to the waist needs to be increased the radius of the main hohlraum should be decreased thus reducing the case-to-capsule ratio. The case-to-capsule ratio can only be reduced so far as a small case-to-capsule ratio results in lower levels of radiation smoothing and a less uniform drive. Albedo profiling of the main hohlraum wall allows the case-to-capsule ratio to remain fixed (or be freely varied) alongside adjusting radiation symmetry onto the capsule.

Here the application of an albedo profiled hohlraum is applied to a cylindrical hohlraum of diameter 13mm and length 10mm with radiation shields at either end of radius 2.3 mm. The capsule situated in the centre of the hohlraum has a radius of 1mm.

Using the linear variation in hohlraum albedo given in equation 6.1 for the Z-pinch hohlraum it is possible to reduce the pole to waist flux ratio to below 1% using a C value of 0.8 corresponding to a reduction in radiated power to 90%, figure 6.4. As with the laser driven hohlraum example, this is comparable to the increase in drive power required to drive a larger hohlraum with a larger capsule to case ratio. There exists a variation in capsule flux between the pole and waist of approximately $< 2\%$ which by using a more

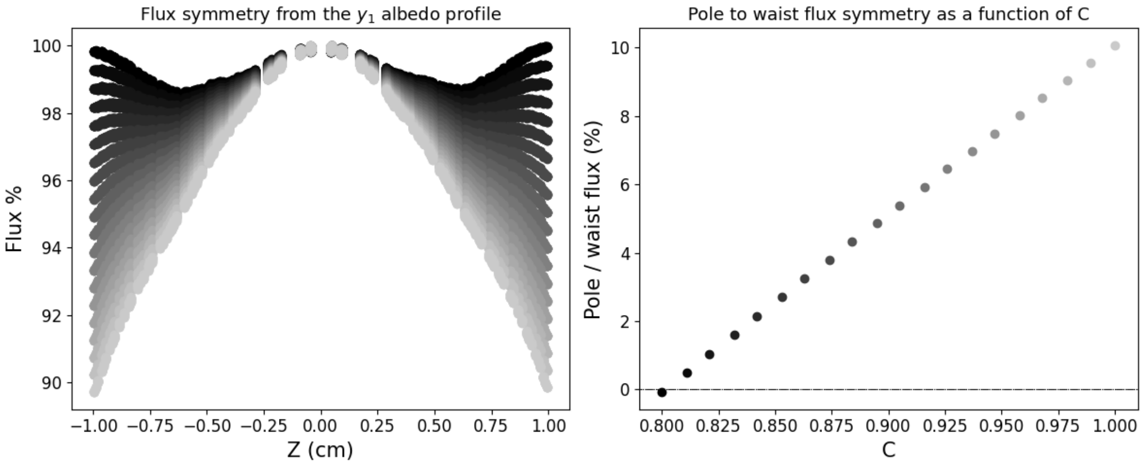

Figure 6.4: (Left) The flux symmetry onto the capsule as a function of the z-axis position for different values of C for the y_1 albedo profile mapped onto a double-ended Z-pinch hohlraum. (Right) The ratio of the pole flux to the waist flux onto the capsule as a function of C is plotted with the pole to waist flux ratio being brough to below 1% at a C value of approximately 0.8. Variation in the flux over the capsule is also of the order of 1% at C = 0.8.

structured hohlraum albedo profile could be reduced in order to increase flux uniformity onto the capsule. For comparison, adjusting target dimensions such as the case to capsule ratio and size of shields in Z-pinch experiments has lead to pole to waist symmetries of approximately 3% [171].

6.3 Discussion

In this work the symmetry control obtainable from an albedo profile applied to laser driven cylindrical hohlraum has been investigated and found to, over a power reduction from 100% to 90%, be able to provide a pole to waist symmetry swing of 15%. In this configuration of hohlraum, capsule, and laser beams the low order symmetry onto the capsule can be reduced to below 1%. Though symmetry tuning can be performed by changing the power ratio between the inner and outer cones and the case-to-capsule ratio this technique provides an additional means by which to achieve symmetrical implosions. This method may open up designs in which the propagation and absorption of the laser beams is prioritized by altering the hohlraum geometry while keeping the radiation symmetry at tolerable levels with the use of albedo-profiling on the hohlraum wall.

The losses in radiated power calculated in this work take into account the losses due to the reduction in reflected power from the low albedo regions of the hohlraum. This does not take into account the potential drop in laser to X-ray conversion efficiency from the low albedo regions of the hohlraum. As low albedo regions would likely consist of materials that have been doped or replaced with some other material with a lower Z number it would necessarily mean that the conversion efficiencies would also be reduced. This means that the overall drop in radiated power predicted from albedo profiling the hohlraum will be larger when accounting for this effect. In addition, there is the potential for an increased relative expansion velocity of the lower albedo regions due to the lower mass that naturally follows from a reduction in the Z number of the wall material. Both these features may be mitigated through the use of foam liners in order to more precisely control expansion velocity and conversion efficiency of laser energy into X-rays as has been found in previous works by other authors [172, 173, 141, 174].

A further restriction to this technique is that as the hohlraum fills with plasma and the capsule converges during the laser pulse the time-dependent drive symmetry on the capsule will change. The static nature of the albedo profile on the hohlraum wall means that during the implosion further tuning of the drive symmetry may be required thus the need for techniques such as CBET in higher hohlraum gas fill experiments and beam phasing may be required in order to maintain a symmetrical implosion through to late times.

In addition, the same technique has been investigated applied to a setup similar to those found in double-ended Z-pinch hohlraum experiments. The restrictions in symmetry tuning imposed by the double-ended Z-pinch hohlraum means that the additional option for albedo lining of the main hohlraum provides an alternative to increasing the case-to-capsule ratio. The pole to waist symmetry was able to be reduced to below 1% while keeping the case-to-capsule ratio constant. While these results do not provide an optimized setup in terms of radiation symmetry they demonstrate the possibility of applying albedo lined hohlraums to this type of experiment and others which involve X-ray sources with a fixed location relative to the capsule or main hohlraum.

Chapter 7

Conclusions

The work contained within Chapter 4 involved a comparison of lined and un-lined gold hohlraums with regard to the suppression of the M-band radiation and overall drive temperature. Particular attention was paid to the time-dependent nature of the liner and how this affects its application to pulse lengths used on the National Ignition Facility of between 10 - 20 ns. The liner consisted of a 0.5 μm copper layer applied to the inside surface of the hohlraum so as to provide a lower-Z environment for laser absorption but retain the high opacity radiation confinement properties of the gold hohraum wall. Simulations were carried out using the 2D radiation hydrodynamics code h2d and the properties of the radiation produced by the lined and un-lined hohlraums were compared. The work contained in the chapter is important for understanding how lining the hohlraum may affect the hard X-ray content in addition to quantifying by how much the hydrodynamic expansion of the liner lowers the radiation temperature of the hohlraum.

The radiation drive produced by the lined hohlraum was found to contain approximately 60% of the high energy X-ray ($hv > 1.8$ keV) energy content of the un-lined hohraum. Regarding the energy contained in the remaining X-rays ($hv < 1.8$ keV) the unlined hohlraum had a comparable performance to the lined hohlraum, within the uncertainty introduced by the rezoning operations. This corresponded to a peak radiation temperature of approximately 270 eV for both the lined and unlined hohlraum though the steepness of the rise to the peak radiation temperature was steeper in the un-lined hohlraum due to the energy loss incurred in the lined hohlraum by the heating and expansion of the liner material.

The lower energy contained in the high energy X-rays for the lined hohlraum shows that by restricting the laser conversion region to the mid-Z copper liner the M-band component of the drive can be suppressed. This benefits capsule design by reducing the requirement for dopant in the ablator, potentially leading to improvements in capsule performance by mitigating some of the detrimental effects of ablator-fuel mixing and improving capsule stability. This work has shown that comparable radiation temperatures can be obtained using a lined hohlraum to an un-lined hohlraum. These results are promising for the future application of mid-Z liners to inertial fusion experiments as the peak radiation temperature is a key determiner of the implosion velocity. However, through looking at the time-dependent processes, this work has highlighted that for longer pulses burn-through of the laser from the liner into the gold wall may lead to a return of the hard X-ray population towards the end of the pulse.

The tendency of the 2D computational mesh to become tangled as the complex hohlraum environment evolves over the course of the laser pulse means that the pulses used in these simulations do not encompass the entire length of a multi-shock pulse. Though the laser power is indicative of the power of the final peak in an inertial fusion laser pulse there is no preceding pulse structure that would usually accompany the final rise. Capturing the effect on the liner and hohlraum environment of a full-length laser pulse is required in order to be able to assess the performance of a lined hohlraum through-out the duration of the capsule implosion. The liner in this case will have had, depending on the type of pulse used, approximately 10-15 ns to expand. The enhanced expansion of the wall due to the presence of a liner may also affect laser-plasma instabilities and propagation of the beams [156] [52, 157].

In Chapter 5 the results obtained in Chapter 4 were built upon by investigating the potential benefits of a reduced M-band spectrum with regards to capsule performance. This was carried out by simulating several capsule and drive combinations with the capsule designs spanning a number of dopant concentrations from 0% to 1% Ge and the X-ray drive spanning a number of M-band peak intensity values from 0% to 10% of the Planckian peak intensity. The peak power of the X-ray drive was varied in order to alter the final implosion velocity in conjunction with adjusting the shock timing in order to maintain low levels of entropy introduced into the DT fuel. Scanning over implosion velocities for the different combinations of capsule dopant concentrations and M-band peaks allowed the ignition threshold for each combination to be obtained.

The ignition threshold energies were found to decrease by nearly 10% when going from a 1% Ge doped ablator to 0%. This was due in part to the reduced mass of the ablator and to the increase in energy coupling to the ablator late in the laser pulse due to lower concentrations of high-Z ions in the capsule coronal plasma. This increases the radiative cooling of the ablator thus lowering the ablation pressure and also reduces the X-ray flux reaching the ablation front. For the conditions obtained in the simulations these effects counter the increased opacity that a higher level of dopant concentration lends. The growth rate of the Rayleigh-Taylor instability at the ablation front was shown to decrease as dopant concentration was reduced. In contrast, as dopant levels were decreased the Atwood number of the ice-ablator interface increased late into the pulse when X-ray preheating begins to set in, even in the case of a 0% M-band spectrum.

By showing a reduction in the energy required for ignition in these 1D simulations the potential benefit of mid-Z lined hohlraums is better understood. Tying the performance in 1D of these implosions to the indicators of hydrodynamic stability in higher dimensional simulations does something to address the incomplete picture that the 1D simulations provide. Though the evolution of the hydrodynamic instabilities and their effect on the shape and composition of the ablator during the implosion is not accounted for in these 1D simulations the rationale behind the reduction in dopant concentrations and its effect on Atwood number and Rayleigh-Taylor growth are still somewhat quantifiable. The choice to use graded dopants in the ablator was made in order to more accurately replicate conditions in NIF targets, as graded dopants are utilised on experiments there in order to increase hydrodynamic stability. However, future simulations in 2D are required in order to more accurately assess the benefits to capsule stability that the combination of decreased dopant levels and decreased M-band content has on capsule performance. However, this work has quantified in 1D the reduction in the ignition threshold and has demonstrated that radiative cooling of the ablator is a large contributor to the increase in threshold energy for more heavily doped capsules.

Contained in Chapter 6 is an investigation into albedo-profiling as a method for increasing the low-order symmetry in inertial fusion experiments. Two cases were considered, that of a laser driven cylindrical hohlraum and that of a double-ended Z-pinch driven cylindrical hohlraum. In each case it was assumed that through doping the hohlraum wall a z-position dependent profile could be achieved that could then be used to affect the radiation symmetry onto the capsule. This technique was investigated using a view-factor code that calculates the radiation balance between surfaces by solving the radiosity equation, equation (3.3). This novel technique is intended to augment the current methods used to adjust the X-ray flux symmetry onto the capsule.

In the case of the laser-driven cylindrical hohlraum the pole-to-waist symmetry onto the capsule was able to be adjusted to $< 1\%$ at the cost of a drop in radiated power by the hohlraum of 10%. Similar results were obtained for the double-ended z-pinch driven hohlraum though it is important to note that neither result represents an optimum configuration with regards to capsule symmetry. The intent of this study was to demonstrate the extent of symmetry control and corresponding loss in radiated power obtained by using this technique. In the case of the laser-driven hohlraum this work is important as it helps to decouple considerations of the laser propagation from the X-ray drive symmetry when designing a hohlraum. This allows for a hohlraum to be shaped such that the laser propagation and deposition is optimized while the drive symmetry is then adjusted after the fact by albedo-profiling the hohlraum. This work also has consequences for double-ended z-pinch hohlraums as the symmetry onto the capsule can be adjusted by albedo-profiling the hohlraum while keeping the case-to-capsule ratio the same. Keeping the same case-to-capsule ratio means that the same levels of geometrical smoothing of the higher order non-uniformity in the radiation field can be maintained.

This work has been focussed on how modifications to the hohlraum can affect the overall performance of the target in indirect-drive inertial confinement fusion. It has been found that by lining a hohlraum with a mid-Z element the conversion of laser energy into X-rays can be made to occur away from the high-Z gold plasma of the hohlraum wall. This results in the removal of the M-band component of the X-ray drive and therefore opens up the possibility of lowering the dopant concentration of capsule ablators. The performance of these reduced dopant capsules was then investigated and the threshold for ignition for a low dopant capsule was found to be lower than that of a more highly doped counterpart. Finally, by modifying the hohlraum wall further via albedo-profiling it was found that symmetry control was possible while maintaining hohlraum dimensions - decoupling hohlraum symmetry from laser propagation and capsule-to-case ratio. These results show that with small modifications to the hohlraum environment gains can be made in terms of capsule implosion performance.

Ignition is a boundary in the conditions of the hotspot that once passed increases the yield of the capsule significantly. Small increments in capsule performance are therefore important in pushing the conditions within the capsule over the ignition boundary. Each step towards inertial fusion whether it be improving the performance of inertial fusion targets or increasing the efficiency of the laser systems used all contribute to the goal of producing a fusion reactor that can output a constant supply of green energy to the grid. Indirect-drive is not without its unique challenges however. In order to realise a reactor based on indirect-drive the issue of target material is of primary importance. Aside from the physics occurring within the target, the high-Z hohlraum needs to not contribute harmful radioactive elements to the power plant cycle. If cheap, low activation targets can be created then indirect drive could deliver on its promise of green energy.

Fusion is an essential part of the future landscape of energy production as the presence of a diverse range of green energy technologies in the future will create a more robust electrical grid that can serve more people, with greater reliability. The abundance and more equal distribution of the fuels needed for nuclear fusion over alternative forms of energy also provides the opportunity to allow a greater range of countries access to this safe, green form of energy.

List of References

[1] Ibrahim Dincer. Renewable energy and sustainable development: a crucial review. *Renewable and Sustainable Energy Reviews*, 4(2):157–175, June 2000.

[2] Thomas M. Brooks, Russell A. Mittermeier, Cristina G. Mittermeier, et al. Habitat loss and extinction in the hotspots of biodiversity. *Conservation Biology*, 16(4):909–923, 2002.

[3] Sajib Mandal, Md. Sirajul Islam, and Md. Haider Ali Biswas. Modeling the potential impact of climate change on living beings near coastal areas. *Modeling Earth Systems and Environment*, July 2020.

[4] Filip Johnsson, Jan Kjärstad, and Johan Rootzén. The threat to climate change mitigation posed by the abundance of fossil fuels. *Climate Policy*, 19(2):258–274, February 2019.

[5] Michael Jakob and Jérôme Hilaire. Unburnable fossil-fuel reserves. *Nature*, 517(7533):150–151, January 2015.

[6] Paris agreement to the united nations framework convention on climate change, 12 2015.

[7] Henrik Zsiborács, Nóra Hegedűsné Baranyai, András Vincze, et al. Intermittent Renewable Energy Sources: The Role of Energy Storage in the European Power System of 2040. *Electronics*, 8(7):729, July 2019.

[8] Dominik Heide, Lueder von Bremen, Martin Greiner, et al. Seasonal optimal mix of wind and solar power in a future, highly renewable Europe. *Renewable Energy*, 35(11):2483–2489, November 2010.

[9] Cory Budischak, DeAnna Sewell, Heather Thomson, et al. Cost-minimized combinations of wind power, solar power and electrochemical storage, powering the grid up to 99.9% of the time. *Journal of Power Sources*, 225:60–74, March 2013.

[10] F. M. Mulder. Implications of diurnal and seasonal variations in renewable energy generation for large scale energy storage. *Journal of Renewable and Sustainable Energy*, 6(3):033105, 2014.

[11] R. A. Bullen, T. C. Arnot, J. B. Lakeman, and F. C. Walsh. Biofuel cells and their development. *Biosensors and Bioelectronics*, 21(11):2015–2045, May 2006.

[12] R.J. Kurtz, A. Alamo, E. Lucon, et al. Recent progress toward development of reduced activation ferritic/martensitic steels for fusion structural applications. *Journal of Nuclear Materials*, 386-388:411–417, apr 2009.

[13] Massimo Zucchetti, Luigi Candido, Vladimir Khripunov, et al. Fusion power plants, fission and conventional power plants. Radioactivity, radiotoxicity, radioactive waste. *Fusion Engineering and Design*, 136:1529–1533, November 2018.

[14] Günther Kessler. Environmental Impacts and Risks of Nuclear Fission Energy. Topics in Energy, pages 191–251. Springer, Vienna, 1983.

[15] Sandro Sandri, Gian Marco Contessa, Marco D'Arienzo, et al. A Review of Radioactive Wastes Production and Potential Environmental Releases at Experimental Nuclear Fusion Facilities. *Environments*, 7(1):6, January 2020.

[16] Gholam A. Kazemi. Deuterium. In *Water Encyclopedia*, pages 438–441. American Cancer Society, 2005.

[17] T. Ihli, T. K. Basu, L. M. Giancarli, et al. Review of blanket designs for advanced fusion reactors. *Fusion Engineering and Design*, 83(7):912–919, December 2008.

[18] A. L. Kritcher, T. Döppner, D. Swift, et al. Probing matter at Gbar pressures at the NIF. *High Energy Density Physics*, 10:27–34, March 2014.

[19] H.-S. Bosch and G. M. Hale. Improved formulas for fusion cross-sections and thermal reactivities. *Nuclear Fusion*, 32(4):611–631, April 1992.

[20] G.H. Miley, H. Towner, and N. Ivich. Fusion cross sections and reactivities. Technical report, jun 1974.

[21] James W. Mayer and E. Rimini. *Ion Beam Handbook for Material Analysis*. Elsevier, December 2012. Google-Books-ID: RYWSgenCMbMC.

[22] M. R. Gilbert, S. L. Dudarev, D. Nguyen-Manh, et al. Neutron-induced dpa, transmutations, gas production, and helium embrittlement of fusion materials. *Journal of Nuclear Materials*, 442(1, Supplement 1):S755–S760, November 2013.

[23] Steven J. Zinkle. Fusion materials science: Overview of challenges and recent progress. *Physics of Plasmas*, 12(5):058101, 2005.

[24] Hiroyasu Tanigawa, Kiyoyuki Shiba, Hideo Sakasegawa, et al. Technical issues related to the development of reduced-activation ferritic/martensitic steels as structural materials for a fusion blanket system. *Fusion Engineering and Design*, 86(9):2549–2552, October 2011.

[25] Masaaki Yamada. Progress in understanding magnetic reconnection in laboratory and space astrophysical plasmas. *Physics of Plasmas*, 14(5):058102, may 2007.

[26] S. V. Bulanov, T. Zh. Esirkepov, D. Habs, et al. Relativistic laser-matter interaction and relativistic laboratoryastrophysics. *The European Physical Journal D*, 55(2):483, May 2009.

[27] J D Lawson. Some Criteria for a Power Producing Thermonuclear Reactor. *Proceedings of the Physical Society. Section B*, 70(1):6–10, jan 1957.

[28] L. A. Artsimovich. Tokamak devices. *Nuclear Fusion*, 12(2):215–252, March 1972.

[29] Lyman Spitzer. The stellarator concept. *Physics of Fluids*, 1(4):253, 1958.

[30] J. D. Jukes. Micro-instabilities in magnetically confined, inhomogeneous plasma. *Physics of Fluids*, 7(9):1468, 1964.

[31] Harold P. Furth. Nonideal magnetohydrodynamic instabilities and toroidal magnetic confinement. *Physics of Fluids*, 28(6):1595, 1985.

[32] John Nuckolls, Lowell Wood, Albert Thiessen, and George Zimmerman. Laser Compression of Matter to Super-High Densities: Thermonuclear (CTR) Applications. *Nature*, 239(5368):139–142, sep 1972.

[33] Moshe Lubin and Arthur Fraas. *Fusion by Laser*, volume 224, pages 21–33. 9 1971.

[34] G. Zimmerman. *Inertial Confinement Fusion*. Lawrence Livermore Laboratory, 1996.

[35] M Roth. *Plasma Phys. Control. Fusion*, 47:B841, 2005.

[36] John Lindl. Development of the indirect-drive approach to inertial confinement fusion and the target physics basis for ignition and gain. *Physics of Plasmas*, 2(11):3933–4024, nov 1995.

[37] R. Kidder. Energy gain of laser-compressed pellets: a simple model calculation. 1976.

[38] S. W. Haan, J. D. Lindl, D. A. Callahan, et al. Point design targets, specifications, and requirements for the 2010 ignition campaign on the National Ignition Facility. *Physics of Plasmas*, 18(5):051001, may 2011.

[39] S. H. Glenzer, D. A. Callahan, A. J. MacKinnon, et al. Cryogenic thermonuclear fuel implosions on the National Ignition Facility. *Physics of Plasmas*, 19(5), may 2012.

[40] K. S. Anderson, C. J. Forrest, O. M. Mannion, et al. Effect of cross-beam energy transfer on target-offset asymmetry in direct-drive inertial confinement fusion implosions. *Physics of Plasmas*, 27(11):112713, nov 2020.

[41] D. H. Froula, D. T. Michel, I. V. Igumenshchev, et al. Laser–plasma interactions in direct-drive ignition plasmas. *Plasma Physics and Controlled Fusion*, 54(12):124016, November 2012.

[42] A. R. Christopherson, R. Betti, C. J. Forrest, et al. Direct Measurements of DT Fuel Preheat from Hot Electrons in Direct-Drive Inertial Confinement Fusion. *Physical Review Letters*, 127(5):055001, July 2021.

[43] S. P. Regan, N. B. Meezan, L. J. Suter, et al. Suprathermal electrons generated by the two-plasmon-decay instability in gas-filled <i>Hohlraums</i>. *Physics of Plasmas*, 17(2):020703, feb 2010.

[44] D. H. Kalantar, T. W. Barbee, L. B. DaSilva, et al. X-ray laser radiography of perturbations due to imprint of laser speckle in 0.35 μm laser irradiation of a thin si foil. *Review of Scientific Instruments*, 67(3):781–785, mar 1996.

[45] M. Tabak, D. H. Munro, and J. D. Lindl. Hydrodynamic stability and the direct drive approach to laser fusion. *Physics of Fluids B: Plasma Physics*, 2(5):1007–1014, may 1990.

[46] J Peebles, S Hu, W Theobald, et al. *Phys. Rev. E*, 99:63208, 6 2019.

[47] Joshua E. Rothenberg. Comparison of beam-smoothing methods for direct-drive inertial confinement fusion. *JOSA B*, 14(7):1664–1671, July 1997.

[48] M Vandenboomgaerde, J Bastian, A Casner, et al. *Phys. Rev. Lett*, 99:65004, 8 2007.

[49] Ke Lan and Wudi Zheng. Novel spherical hohlraum with cylindrical laser entrance holes and shields. *Physics of Plasmas*, 21(9):090704, sep 2014.

[50] Ke Lan, Jie Liu, Zhichao Li, et al. Progress in octahedral spherical hohlraum study. *Matter and Radiation at Extremes*, 1(1):8–27, jan 2016.

[51] M. Vandenboomgaerde, A. Grisollet, M. Bonnefille, et al. Hollow wall to stabilize and enhance ignition hohlraums. *Physics of Plasmas*, 25(1):012713, jan 2018.

[52] H. F. Robey, L. Berzak Hopkins, J. L. Milovich, and N. B. Meezan. The I-Raum: A new shaped hohlraum for improved inner beam propagation in indirectly-driven ICF implosions on the National Ignition Facility. *Physics of Plasmas*, 25(1):012711, January 2018.

[53] Peter Amendt, Darwin Ho, Yuan Ping, et al. Ultra-high (>30%) coupling efficiency designs for demonstrating central hot-spot ignition on the National Ignition Facility using a Frustraum. *Physics of Plasmas*, 26:082707, August 2019.

[54] Hye-Sook Park, J. S. Ross, C. M. Huntington, et al. Laboratory astrophysical collisionless shock experiments on Omega and NIF. In *Journal of Physics: Conference Series*, volume 688, page 012084. IOP Publishing, 2016.

[55] M. Hohenberger. Exploring Deuterium-Tritium Gas-Filled Hohlraums as a High-Yield Neutron Source. Technical report, 2019.

[56] Mark Bowers, Jeff Wisoff, Mark Herrmann, et al. Status of NIF laser and high power laser research at LLNL. In Abdul A. S. Awwal, editor, *High Power Lasers for Fusion Research IV*. SPIE, feb 2017.

[57] J. Molitoris, Richard Lee, and D. Kalantar. *Warm Dense Matter: An Overview*. April 2004.

[58] Jon T. Larsen and Stephen M. Lane. HYADES—A plasma hydrodynamics code for dense plasma studies. *Journal of Quantitative Spectroscopy and Radiative Transfer*, 51(1-2):179–186, jan 1994.

[59] H.J. Kull. Theory of the rayleigh-taylor instability. *Physics Reports*, 206(5):197–325, aug 1991.

[60] David L. Youngs. Numerical simulation of turbulent mixing by rayleigh-taylor instability. *Physica D: Nonlinear Phenomena*, 12(1-3):32–44, jul 1984.

[61] B. A. Hammel, S. W. Haan, D. S. Clark, et al. High-mode Rayleigh-Taylor growth in NIF ignition capsules. *High Energy Density Physics*, 6(2):171–178, jun 2010.

[62] E. N. Loomis, S. R. Greenfield, R. P. Johnson, et al. Investigations into the seeding of instabilities due to x-ray preheat in beryllium-based inertial confinement fusion targets. *Physics of Plasmas*, 17(5):056308, may 2010.

[63] Jianfa Gu, Shiyang Zou, Yongsheng Li, et al. Sensitivity study of ignition capsule implosion performance on the hard x-ray spectral distribution of hohlraum. *Cite as: Phys. Plasmas*, 19:122710, 2012.

[64] H. Takabe, K. Mima, L. Montierth, and R. L. Morse. Self-consistent growth rate of the Rayleigh–Taylor instability in an ablatively accelerating plasma. *Physics of Fluids*, 28(12):3676, sep 1985.

[65] Subrahmanyan Chandrasekhar. *Radiative Transfer*. Courier Corporation, April 2013. Google-Books-ID: 1YHCAgAAQBAJ.

[66] J. P. Apruzese, J. Davis, K. G. Whitney, et al. The physics of radiation transport in dense plasmas. *Physics of Plasmas*, 9(5):2411–2419, 2002.

[67] H. W. Drawin. Validity conditions for local thermodynamic equilibrium. *Zeitschrift fur Physik*, 228(2):99–119, apr 1969.

[68] Tudor Wyatt Johnston and John M. Dawson. Correct values for high-frequency power absorption by inverse bremsstrahlung in plasmas. *The Physics of Fluids*, 16(5):722–722, May 1973.

[69] Su Ming Weng, Zheng Ming Sheng, and Jie Zhang. Inverse bremsstrahlung absorption with nonlinear effects of high laser intensity and non-Maxwellian distribution. *Physical Review E - Statistical, Nonlinear, and Soft Matter Physics*, 80(5), nov 2009.

[70] A. G. R. Thomas, M. Tzoufras, A. P. L. Robinson, et al. A review of Vlasov–Fokker–Planck numerical modeling of inertial confinement fusion plasma. *Journal of Computational Physics*, 231(3):1051–1079, February 2012.

[71] M Seaton. Radiative recombination of hydrogenic ions. *Mon. Not. Roy. Astron. Soc*, 119:81, 1959.

[72] Yu. P. Raizer Ya. B. Zel'dovich. *Physics of shock waves and high-temperature hydrodynamic phenomena*. Dover Publications, 2002.

[73] P. Fromy, C. Deutsch, and G. Maynard. Thomas–fermi-like and average atom models for dense and hot matter. *Physics of Plasmas*, 3(3):714–730, mar 1996.

[74] Vladimir G. Novikov. Average Atom Approximation in Non-LTE Level Kinetics. Springer Series on Atomic, Optical, and Plasma Physics, pages 105–126. Springer International Publishing, Cham, 2016.

[75] M.D. Rosen, H.A. Scott, D.E. Hinkel, et al. The role of a detailed configuration accounting (DCA) atomic physics package in explaining the energy balance in ignition-scale hohlraums. *High Energy Density Physics*, 7(3):180–190, sep 2011.

[76] M.J. Seaton. The theory of excitation and ionization by electron impact. In *Atomic and Molecular Processes*, pages 374–420. Elsevier, 1962.

[77] J. Davis, P.C. Kepple, and M. Blaha. Electron impact excitation coefficients for laboratory and astrophysical plasmas. *Journal of Quantitative Spectroscopy and Radiative Transfer*, 16(12):1043–1055, dec 1976.

[78] H. W. Drawin. Influence of atom-atom collisions on the collisional-radiative ionization and recombination coefficients of hydrogen plasmas. *Zeitschrift fur Physik*, 225:483–493, October 1969. ADS Bibcode: 1969ZPhy..225..483D.

[79] W. J. Karzas and R. Latter. Electron radiative transitions in a coulomb field. *The Astrophysical Journal Supplement Series*, 6:167, may 1961.

[80] V. L. Jacobs and J. Davis. Effects of collisions on level populations and dielectronic recombination rates of multiply charged ions. *Physical Review A*, 18(2):697–710, August 1978.

[81] W. A. Lokke and W. H. Grasberger. XSNQ-U: a non-LTE emission and absorption coefficient subroutine. Technical report, January 1977.

[82] H. F. Robey, T. S. Perry, H. S. Park, et al. Experimental measurement of Au M -band flux in indirectly driven double-shell implosions. *Physics of Plasmas*, 12(7):1–7, jul 2005.

[83] W. J. M. Rankine. XV. on the thermodynamic theory of waves of finite longitudinal disturbance. *Philosophical Transactions of the Royal Society of London*, 160:277–288, dec 1870.

[84] Burkhard Militzer. Path integral calculation of shock hugoniot curves of precompressed liquid deuterium. *Journal of Physics A: Mathematical and General*, 36(22):6159–6164, may 2003.

[85] Miguel A. de Avillez, Gervásio J. Anela, and Dieter Breitschwerdt. Variability of the adiabatic parameter in monoatomic thermal and non-thermal plasmas. *Astronomy & Astrophysics*, 616:A58, aug 2018.

[86] Damian C. Swift, Richard G. Kraus, Eric N. Loomis, et al. Shock formation and the ideal shape of ramp compression waves. *Physical Review E*, 78(6):066115, December 2008.

[87] David Munro, Peter Celliers, G. Collins, et al. Shock timing technique for the National Ignition Facility. *Physics of Plasmas*, 8, May 2001.

[88] H. F. Robey, T. R. Boehly, P. M. Celliers, et al. Shock timing experiments on the National Ignition Facility: Initial results and comparison with simulation. *Physics of Plasmas*, 19(4), apr 2012.

[89] O. L. Landen, D. T. Casey, J. M. DiNicola, et al. Yield and compression trends and reproducibility at NIF*. *High Energy Density Physics*, 36:100755, August 2020.

[90] H. F. Robey, V. A. Smalyuk, J. L. Milovich, et al. Performance of indirectly driven capsule implosions on the National Ignition Facility using adiabat-shaping. *Physics of Plasmas*, 23(5), may 2016.

[91] J.A. Gaffney, S.X. Hu, P. Arnault, et al. A review of equation-of-state models for inertial confinement fusion materials. *High Energy Density Physics*, 28:7–24, sep 2018.

[92] E I Moses. The national ignition facility and the national ignition campaign. *IEEE Transactions on Plasma Science*, 38(4):684–689, apr 2010.

[93] A. J. MacKinnon, N. B. Meezan, J. S. Ross, et al. High-density carbon ablator experiments on the National Ignition Facility. *Physics of Plasmas*, 21(5):056318, may 2014.

[94] T. R. Dittrich, O. A. Hurricane, D. A. Callahan, et al. Design of a high-foot high-adiabat ICF capsule for the national ignition facility. *Physical Review Letters*, 112(5), feb 2014.

[95] O. A. Hurricane, D. A. Callahan, D. T. Casey, et al. The high-foot implosion campaign on the National Ignition Facility. *Physics of Plasmas*, 21(5), 2014.

[96] D. T. Casey, V. A. Smalyuk, K. S. Raman, et al. Reduced instability growth with high-adiabat high-foot implosions at the National Ignition Facility. *Physical Review E - Statistical, Nonlinear, and Soft Matter Physics*, 90(1), jul 2014.

[97] D. A. Callahan, O. A. Hurricane, D. E. Hinkel, et al. Higher velocity, high-foot implosions on the National Ignition Facility laser. *Physics of Plasmas*, 22(5), may 2015.

[98] R. E. Marshak. Effect of Radiation on Shock Wave Behavior. *Physics of Fluids*, 1(1):24, nov 1958.

[99] John D. Lindl, Peter Amendt, Richard L. Berger, et al. The physics basis for ignition using indirect-drive targets on the National Ignition Facility. *Physics of Plasmas*, 11(2):339–491, feb 2004.

[100] M. C. Herrmann, M. Tabak, and J. D. Lindl. A generalized scaling law for the ignition energy of inertial confinement fusion capsules. *Nuclear Fusion*, 41(1):99–111, January 2001.

[101] Peter Amendt. Progress in High Capsule-Energy-Coupling Studies on the NIF Using Advanced Hohlraums. 2020:KI02.004, January 2020. ADS Bibcode: 2020APS..DPPK02004A.

[102] Edward I. Moses and Craig R. Wuest. The National Ignition Facility: Laser Performance and First Experiments. *Fusion Science and Technology*, 47(3):314–322, apr 2005.

[103] Edward Moses. Overview of the National Ignition Campaign (NIC). 52:MR1.001, November 2010. ADS Bibcode: 2010APS..DPPMR1001M.

[104] E L Dewald, L J Suter, C Thomas, et al. First hot electron measurements in near-ignition scale hohlraums on the national ignition facility. *Journal of Physics: Conference Series*, 244(2):022074, aug 2010.

[105] J. D. Moody, D. A. Callahan, D. E. Hinkel, et al. Progress in hohlraum physics for the National Ignition Facility. *Physics of Plasmas*, 21(5), 2014.

[106] D. Turnbull, L. F. Berzak Hopkins, S. Le Pape, et al. Symmetry control in subscale near-vacuum hohlraums. *Physics of Plasmas*, 23(5):52710, 2016.

[107] L. F. Berzak Hopkins, N. B. Meezan, S. Le Pape, et al. First High-Convergence Cryogenic Implosion in a Near-Vacuum Hohlraum. *Physical Review Letters*, 114(17):175001, apr 2015.

[108] Hans G. Rinderknecht, P. A. Amendt, S. C. Wilks, and G. Collins. Kinetic physics in ICF: Present understanding and future directions. *Plasma Physics and Controlled Fusion*, 60(6), apr 2018.

[109] G. N. Hall, O. S. Jones, D. J. Strozzi, et al. The relationship between gas fill density and hohlraum drive performance at the national ignition facility. *Physics of Plasmas*, 24(5):052706, may 2017.

[110] J. L. Kline, S. H. Batha, L. R. Benedetti, et al. Progress of indirect drive inertial confinement fusion in the United States. *Nuclear Fusion*, 59(11), jul 2019.

[111] A. B. Zylstra, A. L. Kritcher, O. A. Hurricane, et al. Record Energetics for an Inertial Fusion Implosion at NIF. *Physical Review Letters*, 126(2):025001, January 2021.

[112] V. A. Smalyuk, H. F. Robey, D. T. Casey, et al. Mix and hydrodynamic instabilities on NIF. *Journal of Instrumentation*, 12(06):C06001–C06001, June 2017.

[113] C. R. Weber, D. T. Casey, D. S. Clark, et al. Improving ICF implosion performance with alternative capsule supports. *Physics of Plasmas*, 24(5):056302, may 2017.

[114] Andrea Kritcher. Achieving Record Hot Spot Energies with the Largest HDC Implosions on NIF in HYBRID-E. In *APS Division of Plasma Physics Meeting Abstracts*, volume 2020 of *APS Meeting Abstracts*, page KI02.003, January 2020.

[115] A. L. Kritcher, A. B. Zylstra, D. A. Callahan, et al. Achieving record hot spot energies with large HDC implosions on NIF in HYBRID-e. *Physics of Plasmas*, 28(7):072706, jul 2021.

[116] Lyman Spitzer. Physics of Fully Ionized Gases. *American Journal of Physics*, 31(11):890–891, November 1963.

[117] M. M. Marinak, G. D. Kerbel, N. A. Gentile, et al. Three-dimensional HYDRA simulations of national ignition facility targets. *Physics of Plasmas*, 8(5):2275–2280, may 2001.

[118] M. Holec, J. Nikl, and S. Weber. Nonlocal transport hydrodynamic model for laser heated plasmas. *Physics of Plasmas*, 25(3):032704, March 2018.

[119] G. P. Schurtz, Ph. D. Nicolaï, and M. Busquet. A nonlocal electron conduction model for multidimensional radiation hydrodynamics codes. *Physics of Plasmas*, 7(10):4238–4249, October 2000.

[120] R. C. Malone, R. L. McCrory, and R. L. Morse. Indications of Strongly Flux-Limited Electron Thermal Conduction in Laser-Target Experiments. *Physical Review Letters*, 34(12):721–724, March 1975.

[121] M. D. Rosen, D. W. Phillion, V. C. Rupert, et al. The interaction of 1.06 μm laser radiation with high Z disk targets. *The Physics of Fluids*, 22(10):2020–2031, October 1979.

[122] O. S. Jones, L. J. Suter, H. A. Scott, et al. Progress towards a more predictive model for hohlraum radiation drive and symmetry. *Physics of Plasmas*, 24(5):056312, may 2017.

[123] Ariane Middel, Jonas Lukasczyk, and Ross Maciejewski. Sky View Factors from Synthetic Fisheye Photos for Thermal Comfort Routing—A Case Study in Phoenix, Arizona. *Urban Planning*, 2:19, March 2017.

[124] E. L. Dewald, M. Rosen, S. H. Glenzer, et al. X-ray conversion efficiency of high-Z hohlraum wall materials for indirect drive ignition. *Physics of Plasmas*, 15(7):072706, jul 2008.

[125] J. S. Ross, P. Amendt, L. J. Atherton, et al. Lead (Pb) Hohlraum: Target for Inertial Fusion Energy. *Scientific Reports*, 3(1):1453, dec 2013.

[126] H. L. Wilkens, A. Nikroo, D. R. Wall, and J. R. Wall. Developing depleted uranium and gold cocktail hohlraums for the National Ignition Facility. In *Physics of Plasmas*, volume 14, 2007.

[127] E. F. Gabl, B. H. Failor, Gar E. Busch, et al. Plasma evolution from laser-driven gold disks. I. Experiments and results. *Physics of Fluids B*, 2(10):2437–2447, 1990.

[128] D. Ress, L. J. Suter, E. F. Gabl, and B. H. Failor. Plasma evolution from laser-driven gold disks. II. Computational design and analysis. *Physics of Fluids B*, 2(10):2448–2455, 1990.

[129] M. Murakami and J. Meyer-ter Vehn. Indirectly driven targets for inertial confinement fusion. *Nuclear Fusion*, 31(7):1315–1331, jul 1991.

[130] R E Olson, R J Leeper, A Nobile, and J A Oertel. Preheat Effects on Shock Propagation in Indirect-Drive Inertial Confinement Fusion Ablator Materials.

[131] Yongsheng Li, Jianfa Gu, Changshu Wu, et al. Effects of the P2 M-band flux asymmetry of laser-driven gold Hohlraums on the implosion of ICF ignition capsule. *Physics of Plasmas*, 23(7):072705, jul 2016.

[132] S. W. Haan, M. C. Herrmann, T. R. Dittrich, et al. Increasing robustness of indirect drive capsule designs against short wavelength hydrodynamic instabilities. In *Physics of Plasmas*, volume 12, pages 1–8, may 2005.

[133] Yongsheng Li, Chuanlei Zhai, Guoli Ren, et al. P2 asymmetry of Au's M-band flux and its smoothing effect due to high-Z ablator dopants. *Matter and Radiation at Extremes*, 2(2):69–76, mar 2017.

[134] S. P. Regan, R. Epstein, B. A. Hammel, et al. Hot-spot mix in ignition-scale inertial confinement fusion targets. *Physical Review Letters*, 111(4), jul 2013.

[135] T. Ma, P. K. Patel, N. Izumi, et al. Onset of hydrodynamic Mix in high-velocity, highly compressed inertial confinement fusion implosions. *Physical Review Letters*, 111(8), aug 2013.

[136] A. Pak, L. Divol, C. R. Weber, et al. Impact of Localized Radiative Loss on Inertial Confinement Fusion Implosions. *Physical Review Letters*, 124(14):145001, April 2020.

[137] G. P. Grim, N. Guler, F. E. Merrill, et al. Nuclear imaging of the fuel assembly in ignition experiments. *Physics of Plasmas*, 20(5), may 2013.

[138] H. Hora, S. Eliezer, J. M. Martinez-Val, and G. H. Miley. High-gain volume ignition for inertial confinement fusion (ICF). *AIP Conference Proceedings*, 318(1), October 1994.

[139] R. E. Olson, G. A. Rochau, E. L. Dewald, et al. Modification of a laser Hohlraum spectrum via a Mid-Z Wall Liner. *Bulletin of the American Physical Society, Program of the 46th Annual Meeting of the Division of Plasma Physics*, 2004.

[140] A. S. Moore, N. B. Meezan, J. Milovich, et al. Foam-lined hohlraum, inertial confinement fusion experiments on the national ignition facility. *Physical Review E*, 102(5):051201, nov 2020.

[141] Paul Fitzsimmons, Fred Elsner, Reny Paguio, et al. Zinc Oxide–Coated Poly(HIPE) Annular Liners to Advance Laser Indirect Drive Inertial Confinement Fusion. *Fusion Science and Technology*, 73(2):210–218, February 2018.

[142] R. Cauble and W. Rozmus. The inverse bremsstrahlung absorption coefficient in collisional plasmas. *The Physics of Fluids*, 28(11):3387–3392, November 1985.

[143] Patrick Mora. Theoretical model of absorption of laser light by a plasma. *Physics of Fluids*, 25(6):1051, 1982.

[144] M. Kundu. Collisional absorption of laser light in under-dense plasma: The role of Coulomb logarithm. *Physics of Plasmas*, 21(1):013302, January 2014.

[145] C. E. Max. Physics of laser fusion. Vol. I. Theory of the coronal plasma in laser-fusion targets. Technical report, December 1981.

[146] R. Sigel, K. Eidmann, F. Lavarenne, and R. F. Schmalz. Conversion of laser light into soft x rays. Part I: Dimensional analysis. *Physics of Fluids B: Plasma Physics*, 2(1):199–207, jan 1990.

[147] K. Eidmann, R. F. Schmalz, and R. Sigel. Conversion of laser light into soft x rays. Part II: Numerical results. *Physics of Fluids B: Plasma Physics*, 2(1):208–217, jan 1990.

[148] O. S. Jones, J. Schein, M. D. Rosen, et al. Proof of principle experiments that demonstrate utility of cocktail hohlraums for indirect drive ignition. *Physics of Plasmas*, 14(5):056311, may 2007.

[149] T. Döppner, D. A. Callahan, O. A. Hurricane, et al. Demonstration of High Performance in Layered Deuterium-Tritium Capsule Implosions in Uranium Hohlraums at the National Ignition Facility. *Physical Review Letters*, 115(5):055001, July 2015.

[150] Liang Guo, Yongkun Ding, Pifeng Xing, et al. Uranium hohlraum with an ultrathin uranium-nitride coating layer for low hard x-ray emission and high radiation temperature. *New Journal of Physics*, 17(11), oct 2015.

[151] E. L. Dewald, R. Tommasini, N. B. Meezan, et al. First demonstration of improved capsule implosions by reducing radiation preheat in uranium vs gold hohlraums. *Physics of Plasmas*, 25(9):092702, September 2018.

[152] B. I. Bennett, J. D. Johnson, G. I. Kerley, and G. T. Rood. Recent developments in the Sesame equation-of-state library. Technical report, February 1978.

[153] J. E. Ralph, O. Landen, L. Divol, et al. The influence of hohlraum dynamics on implosion symmetry in indirect drive inertial confinement fusion experiments. *Physics of Plasmas*, 25(8):082701, aug 2018.

[154] G. A. Kyrala, J. L. Kline, S. Dixit, et al. Symmetry tuning for ignition capsules via the symcap technique. *Physics of Plasmas*, 18(5), may 2011.

[155] William Riedel, Nathan Meezan, Drew Higginson, et al. Interpenetration and kinetic effects in converging, high-energy plasma jets. *High Energy Density Physics*, 37:100861, November 2020.

[156] William L. Kruer, Scott C. Wilks, Bedros B. Afeyan, and Robert K. Kirkwood. Energy transfer between crossing laser beams. *Physics of Plasmas*, 3(1):382–385, January 1996.

[157] Y. Ping, V. A. Smalyuk, P. Amendt, et al. Symmetry tuning and high energy coupling for an al capsule in a au rugby hohlraum on nif. *Physics of Plasmas*, 27(10):100702, 2020.

[158] D. S. Clark, S. W. Haan, A. W. Cook, et al. Short-wavelength and three-dimensional instability evolution in National Ignition Facility ignition capsule designs. *Physics of Plasmas*, 18(8), aug 2011.

[159] D. G. Hicks, N. B. Meezan, E. L. Dewald, et al. Implosion dynamics measurements at the National Ignition Facility. *Physics of Plasmas*, 19(12), dec 2012.

[160] Jian-Fa Gu, Zhen-Sheng Dai, Yong-Sheng Li, et al. Optimization of the Doped Ablator Layers for the Plastic Ignition Capsule. *Communications in Theoretical Physics*, 63:236–242, February 2015. ADS Bibcode: 2015CoTPh..63..236G.

[161] Karabi Ghosh and Gaurav Mishra. Effect of soft and hard x-rays on shock propagation, preheating and ablation characteristics in pure and doped Be ablators. *arXiv:2108.02933 [physics]*, August 2021. arXiv: 2108.02933.

[162] Yongsheng Li, Wen Yi Huo, and Ke Lan. A novel method for determining the M-band fraction in laser-driven gold hohlraums. *Physics of Plasmas*, 18(2):022701, February 2011.

[163] R. K. Kirkwood, J. D. Moody, J. Kline, et al. A review of laser–plasma interaction physics of indirect-drive fusion. *Plasma Physics and Controlled Fusion*, 55(10):103001, September 2013.

[164] R. E. Olson, L. J. Suter, J. L. Kline, et al. X-ray conversion efficiency in vacuum hohlraum experiments at the National Ignition Facility. *Physics of Plasmas*, 19(5):053301, May 2012.

[165] S. Le Pape, L. F. Berzak Hopkins, L. Divol, et al. The near vacuum hohlraum campaign at the NIF: A new approach. *Physics of Plasmas*, 23(5):056311, may 2016.

[166] George Kyrala, A. Seifter, Nelson Hoffman, et al. Using beam phasing and pointing to control indirect drive implosion symmetry. January 2007.

[167] Los Alamos National Laboratory, United States, and United States, editors. *Symmetry control using beam phasing in ˜0.2 NIF scale high temperature Hohlraum experiment on OMEGA*. United States. Dept. of Energy ; distributed by the Office of Scientific and Technical Information, U.S. Dept. of Energy, Washington, D.C. : Oak Ridge, Tenn, 2009.

[168] D. Callahan, O. Hurricane, Joseph Ralph, et al. Exploring the limits of case-to-capsule ratio, pulse length, and picket energy for symmetric hohlraum drive on the National Ignition Facility Laser. *Physics of Plasmas*, 25:056305, May 2018.

[169] L. Divol, A. Pak, L. F. Berzak Hopkins, et al. Symmetry control of an indirectly driven high-density-carbon implosion at high convergence and high velocity. *Physics of Plasmas*, 24(5):056309, may 2017.

[170] Zhenghong Li, Zhen Wang, Rongkun Xu, et al. Experimental investigation of Z-pinch radiation source for indirect drive inertial confinement fusion. *Matter and Radiation at Extremes*, 4(4):046201, July 2019.

[171] G. R. Bennett, R. A. Vesey, M. E. Cuneo, et al. Symmetric inertial confinement fusion capsule implosions in a high-yield-scale double-z-pinch-driven hohlraum on z. *Physics of Plasmas*, 10(9):3717–3727, sep 2003.

[172] Suhas Bhandarkar, Ted Baumann, Noel Alfonso, et al. Fabrication of Low-Density Foam Liners in Hohlraums for NIF Targets. *Fusion Science and Technology*, 73(2):194–209, 2018.

[173] Yunsong Dong, Jiamin Yang, Tianming Song, et al. Efficient soft x-ray sources from laser-irradiated gold foam targets with well-controlled impurities. *Nuclear Fusion*, 58(1), 2018.

[174] A. S. Moore, N. B. Meezan, C. A. Thomas, et al. Experimental demonstration of the reduced expansion of a laser-heated surface using a low density foam layer, pertaining to advanced hohlraum designs with less wall-motion. *Physics of Plasmas*, 27(8):082706, aug 2020.